Experimental investigation of AISI 4140 steel manufactured by Powder Bed Fusion-Laser Beam

Zur Erlangung des akademischen Grades eines
DOKTORS DER INGENIEURWISSENSCHAFTEN
(Dr.-Ing.)
von der KIT-Fakultät für Maschinenbau des
Karlsruher Instituts für Technologie (KIT)
angenommene

DISSERTATION

von

M.Sc. Chuan Shi

Tag der mündlichen Prüfung:	19. March 2025
Hauptreferent:	Prof. Dr.-Ing. habil. Volker Schulze
Korreferent:	Prof. Dr.-Ing. Eberhard Kerscher

Acknowledgement

Having spent four fulfilling and busy years in Germany, completing my doctoral research project, this experience has been incredibly important and valuable to me. The four years of living in Germany expanded my horizons, broadened my knowledge, and allowed me to firsthand experience the differences between cultures. I have also strived to understand and embrace different values with an objective and dialectical attitude.

First and foremost, I would like to express my gratitude to the China Scholarship Council for the financial support provided (CSC No. 201908320344). This support helped cover my living expenses in Germany and allowed me to focus on my research work without worries.

I would like to extend special thanks to Prof. Volker Schulze, who provided me with the opportunity to study and exchange in Germany and offered constructive feedback during the writing process of my papers and this thesis. Secondly, I would like to thank Dr. Stefan Dietrich, who provided guidance and assistance throughout my research journey, offering valuable advice that greatly contributed to the completion of my research tasks and the writing of my doctoral thesis. I am also grateful for his meticulous proofreading and language assistance.

Additionally, I would like to thank my colleagues at IAM-WK FUB research group for their kind and selfless help when I need help. I also want to express my appreciation to colleagues in the workshop for their assistance in specimen preparation, enabling the smooth conduction of various mechanical tests. Furthermore, I want to acknowledge Dr. Gibmeier Jens and his team for their support in residual stresses testing.

Lastly, I want to thank my parents for their understanding and support throughout my studies abroad.

Karlsruhe, 07.2023

Chuan Shi

Abstract

The Powder Bed Fusion-Laser Beam technology is a green additive manufacturing technique with enormous potential and is receiving increasing attention. This thesis systematically studies the correlations among the laser process parameters, defect formation, and mechanical performances of AISI 4140 steel produced by Powder Bed Fusion-Laser Beam. Moreover, the effects of various heat treatments, including substrate preheating, quenching and tempering, hot isostatic pressing, and laser remelting, on the microstructure, hardness, residual stress, and mechanical properties of AISI 4140 steel are investigated. Additionally, feasible methods for eliminating various types of defects are summarized.

This thesis consists of 7 chapters. Chapter 1 introduces the research motivation, and Chapter 2 discusses commonly used metal additive manufacturing technologies, summarizing their respective advantages and disadvantages. This chapter also focusses on the potential defect formation and elimination methods in Powder Bed Fusion-Laser Beam of steels and outlines current relevant research. Chapter 3 covers the experimental principles, plans, and equipments.

Chapter 4 focuses on processing parameters optimization, studying the effects of processing parameters on relative density, crack density, surface roughness, etc. The experimental results show that, through processing parameters optimization, the relative density of AISI 4140 manufactured by Powder Bed Fusion-Laser Beam can reach 99 %, and the crack density is around 0.28 mm/mm^2. Although substrate preheating cannot eliminate the existence of pores, it significantly reduces the density of micro-cracks to less than 0.01 mm/mm^2. Additionally, the effects of laser remelting on relative density, crack density, surface roughness are investigated. Laser remelting can effectively improve relative density to 99.6 % and reduce surface roughness, but the processing parameters of laser remelting must be optimized again to achieve ideal results.

Chapter 5 covers the microstructure and mechanical properties of AISI 4140, including impact toughness, tensile performance and fatigue behavior. The experimental results show that specimens manufactured horizontally with substrate preheating exhibit the highest tensile strength, which is close to that of traditionally manufactured parts. Results of Charpy impact tests show that the impact toughness of the Powder Bed Fusion-Laser Beam specimens is only 50 % of that of traditionally manufactured parts, and the impact toughness sharply decreases as the porosity increases. The fatigue performance of the specimens manufactured by Powder Bed Fusion-Laser Beam without substrate preheating (50 MPa) is only about 11 % of that observed in traditionally manufactured parts (450

MPa), whereas substrate preheating can significantly improve the fatigue limit, increasing it by 6 times (350 MPa). The specimens treated with hot isostatic pressing and quenching & tempering exhibit similar fatigue limits to those manufactured by traditional processes. Hot isostatic pressing significantly eliminates the size, number, and sphericity of internal defects in additive manufacturing specimens, and the residual tensile stress on the surface and subsurface of the specimens is released after hot isostatic pressing.

The experimental fatigue results in Chapter 5 show that the killer defect size does not affect the fatigue limit within a certain threshold, but the residual stress at the killer defect tips has a greater impact on the fatigue limit than the defect size itself. In Chapter 6, this concept is studied and validated, namely, the fatigue limit of Powder Bed Fusion-Laser Beam specimens can be improved even with substantial defects in the microstructure (200-500 µm), just by releasing the tensile residual stresses within these specimens. Results show that tempering can elevate the fatigue limit of as-built specimen from 50 MPa to 337 MPa; Deep rolling can enhance the fatigue limit by imparting compressive residual stresses up to -1200 MPa on the surface of specimens through plastic deformation. Moreover, the high compressive residual stresses resulting from deep rolling effectively enclose defects near the surface. Laser remelting, on the other hand, only marginally improves the fatigue limit of as-built specimens from 50 MPa to 72.5 MPa. This marginal improvement can be ascribed to the high remaining tensile residual stresses about 300-400 MPa following laser remelting. Finally, Chapter 7 provides a comprehensive summary of the experimental findings and offers an outlook.

Kurzfassung

Die Laserstrahlschmelzen (PBF-LB/M) ist ein pulverbettbasiertes additives Fertigungsverfahren mit enormem Potenzial hinsichtlich Geometriefreiheit und Werkstoffleistungsfähigkeit, welche zunehmende Aufmerksamkeit erfährt. Diese Dissertation untersucht systematisch die Zusammenhänge zwischen den Laserprozessparametern, der Defektbildung und den mechanischen Eigenschaften des Stahls 42CrMo4, der Mittels PBF-LB/M hergestellt wurde. Darüber hinaus werden die Auswirkungen verschiedener Wärmebehandlungen, einschließlich Substratvorwärmung, Abschrecken und Anlassen, heißisostatisches Pressen und Laser-Wiederaufschmelzen, auf die Mikrostruktur, Härte, Eigenspannungen und mechanischen Eigenschaften von 42CrMo4 untersucht. Zusätzlich werden praktikable Methoden zur Beseitigung verschiedener Arten von Defekten zusammengefasst.

Diese Dissertation besteht aus 7 Kapiteln. Kapitel 1 führt in die Forschungsmotivation ein, Kapitel 2 behandelt weiter gängige additive Fertigungstechnologien für metallische Werkstoffe und fasst ihre jeweiligen Vor- und Nachteile zusammen. Zusätzlich befasst sich Kapitel 2 mit der Defektbildung und Methoden zu ihrer Beseitigung im PBF-LB/M von Stählen und stellt den aktuellen Stand der Forschung umfassend dar. Kapitel 3 beschreibt sowohl das experimentelle Design als auch die experimentellen Methoden und Messverfahren sowie Anlagen zur additiven Fertigung.

Kapitel 4 konzentriert sich auf die Optimierung der Verarbeitungsparameter anhand der Einflüsse von Verarbeitungsparametern auf die relative Dichte, Rissdichte und Oberflächenrauheit. Die experimentellen Ergebnisse zeigen, dass durch die Optimierung der Verarbeitungsparameter die relative Dichte von 42CrMo4 aus dem PBF-LB/M einen Wert von über 99 % erreichen kann und die Rissdichte etwa 0,28 mm/mm^2 beträgt. Obwohl die Substratvorwärmung das Vorhandensein von Poren nicht beseitigen kann, reduziert sie signifikant die Dichte von Mikrorissen auf weniger als 0,01 mm/mm^2. Zusätzlich werden die Auswirkungen des Laser-Wiederaufschmelzens auf relative Dichte, Rissdichte und Oberflächenrauheit untersucht. Laser-Wiederaufschmelzen kann die relative Dichte effektiv auf 99,6 % verbessern und die Oberflächenrauheit reduzieren.

Kapitel 5 behandelt die Mikrostruktur und mechanischen Eigenschaften von 42CrMo4, einschließlich Schlagzähigkeit, Zugfestigkeit und Ermüdungsverhalten. Die experimentellen Ergebnisse zeigen, dass Proben je nach Baurorientierung und vorhandener Substratvorwärmung Zugfestigkeit aufweisen, die nahe an der des konventionell hergestellten Schmiedewerkstoff liegt. Die Ergebnisse der Charpy-Schlagzähigkeitsprüfungen zeigen, dass die Schlagzähigkeit der PBF-LB/M-Proben nur 50 % der von konventionell hergestelltem Material

beträgt und die Schlagzähigkeit sehr sensitiv auf die Restporosität reagiert. Die Ermüdungsfestigkeit der Proben, die durch PBF-LB/M ohne Substratvorwärmung hergestellt wurden (50 MPa), beträgt nur etwa 11 % derjenigen von konventionell hergestelltem Material (450 MPa), während die Substratvorwärmung die Wechselfestigkeit signifikant verbessern kann und sie um das 6-fache erhöht (350 MPa). Die mit heißisostatischem Pressen und Abschrecken & Anlassen behandelten Proben heben das Wechselfestigkeitsniveau weiter bis auf den Wert konventionell hergestellter Proben. Das heißisostatische Pressen beseitigt signifikant die Größe, Anzahl und Sphärizität interner Defekte in additiv gefertigten Proben während Eigenspannungen an der Oberfläche und in der Randschicht abgebaut werden.

Die experimentellen Ergebnisse in Kapitel 5 zeigen, dass die Größe des versagenskritischen Defekts die Ermüdungsfestigkeit bis unterhalb einer bestimmten Schwelle nicht maßgeblich beeinflusst, sondern Eigenspannungen im Bereich versagenskritischer Defekte einen größeren Einfluss aufweisen. In Kapitel 6 wird diese Wechselwirkung analytisch berechnet, validiert und im Gesamtkontext diskutiert. Dabei wird die Ermüdungsfestigkeit von PBF-LB/M-Proben mit erheblichen Defekten in der Mikrostruktur (200-500 µm) nach Relaxation der Zugeigenspannungen den as-build Proben gegenübergestellt. Die Ergebnisse zeigen, dass bereits ein einfaches Anlassen die Ermüdungsfestigkeit von as-built Proben von 50 MPa auf 337 MPa erhöhen kann; Festwalzen kann die Ermüdungsgrenze durch die Erzeugung von Druckeigenspannungen von bis zu -1200 MPa an der Probenoberfläche noch weiter verbessern. Laser-Wiederaufschmelzen hingegen verbessert die Ermüdungsfestigkeit von as-built Proben nur marginal von 50 MPa auf 72,5 MPa. Diese marginale Verbesserung kann auf die hohen verbleibenden Zugeigenspannungen von etwa 300-400 MPa nach dem Laser-Wiederaufschmelzen zurückgeführt werden. Schließlich bietet Kapitel 7 eine umfassende Zusammenfassung der experimentellen Ergebnisse und einen Ausblick.

Contents

List of Figures

List of Tables

Nomenclature

$\Delta\sigma_e$	fatigue strength of plain material
ΔK_{eff}	effective stress intensity factor range
$\Delta K_{th,lc}$	threshold stress intensity factor range for long cracks
$\Delta K_{th,sc}$	threshold stress intensity factor range for short cracks
ΔK_{tot}	total stress intensity range
ρ^*	notch tip radius
σ_a	stress amplitude
σ_{re}	residual stress
$\sqrt{area_0}$	the material parameter in El-Haddad model
$\sqrt{area_{th}}$	threshold defect size
$\sqrt{area}$	defect size
A_f	elongation after fracture
$K_{max,appl}$	maximum applied stress intensity factor
$K_{max,tot}$	total maximum stress intensity factor
$K_{min,appl}$	minimum applied stress intensity factor
K_{re}	residual stress intensity factor
M_1, M_2, M_3	geometry dependent factors
AB	as-built specimen
AM	Additive Manufacturing
AT	aging treatment
BJ	Binder Jetting
CAD	Computer Aided Design
CD	crack density
CM	conventionally manufactured
DED	Direct Energy Deposition
DR	deep rolling
FDM	Fused Deposition Modelling
h	hatching distance
HIP	Hot Isostatic Pressing
LED	linear energy density

LoF	lack of fusion
LR	Laser Remelting
m(x, $\sqrt{area}$)	the universal weight function
P	laser power
p	driving force constant
P+AB	specimen manufactured with base preheating
PBF-EB	Powder Bed Fusion-Electron Beam
PBF-LB	Powder Bed Fusion-Laser Beam
QT	quench and temper
R0	without remelting
R1	one remelting step
R2	two remelting steps
RD	relative density
SEM	Scanning Electron Microscope
SL	Stereolithography
SLM	Selective Laser Melting
SLS	Selective Laser Sintering
ST	solution treatment
t	powder layer thickness
UTS	ultimate tensile strength
v	laser scanning speed
VED	volumetric energy density
X-CT	X-ray computed tomography
XRD	X-ray diffraction
Y	shape factor
YS	yield strength

1. Introduction

AISI 4140 is a medium carbon steel with a carbon content of about 0.38 %-0.45 %, which exhibits excellent mechanical properties and is widely used in the automotive industry for critical components such as axles and gears. Traditional manufacturing methods and heat treatment processes for AISI 4140 steel have been extensively researched and industrially applied [1, 2, 3]. However, the limitations of traditional forging processes become apparent for small batch production and advanced structural design verification, such as high costs and the inability to produce complex and functional designs [4].

With the advancement and optimization of material forming processes, Powder Bed Fusion-Laser Beam additive manufacturing has emerged as a popular research topic. Compared with traditional manufacturing processes such as casting and forging, laser additive manufacturing offers advantages such as near net shape production of complex geometries, integral forming, gradient mechanical properties, design and manufacturing of new materials and the use of green energy, thus attracting significant attention from both the industry and academia [5, 6].

However, for Powder Bed Fusion-Laser Beam (PBF-LB) of metal powder materials, the current limitation lies in the limited types of available powders. Research and commercial use of powders are mainly focused on aluminum-based alloys like AlSi10Mg, titanium-based alloys like Ti6Al4V, and nickel-based alloys e.g. Inconel 718. For iron-based powders, 316L is the most extensively studied steel material, while for other low alloy iron-based materials, such as AISI 4130, 4140, only limited research is available [7]. In addition, there are still some general process and performance issues with PBF-LB manufactured parts. Different metal powders may require different laser manufacturing process parameters, which need to be optimized specifically for each alloy. Even if the optimized process parameters are used, there may still be variations in product performance when different brands of PBF-LB machines are adopted, leading to a lack of repeatability of the manufactured parts.

The critical defects in the PBF-LB process are large porosity caused by gas pores, keyholes, and unmelted powder. In the case of AISI 4140, due to its high carbon content and rapid cooling rate during the manufacturing process, the microstructure is mainly martensitic. Therefore, the expansion of martensite can cause large residual stresses, resulting in a high number of microcracks inside the additively manufactured components. The investigation into the effect of laser process parameters on crack density in AISI 4140 steel has not been extensively reported.

In terms of mechanical properties, generally speaking, the denser the parts and the lower the crack density of parts manufactured by PBF-LB, the higher the mechanical properties. It should be noted that there have been no reports of metal parts with 100 % density manufactured by additive manufacturing. Especially for materials such as AISI 4140 with poor welding wetting properties, defects are unavoidable. Nonetheless, there remains a scarcity of systematic studies on the influence of varying porosity, defect types, and crack density on the mechanical properties of AISI 4140.

For most components subjected to cyclic dynamic loads, the fatigue performance needs to be reliably tested. Unfortunately, the fatigue limit of PBF-LB metal components is currently only about 50 % of that of components manufactured by traditional forging or casting processes [8, 9], which greatly limits the scope of application of PBF-LB products. Researchers have conducted extensive studies on how to improve the fatigue performance of additively manufactured components, including optimizing process parameters, hot isostatic pressing heat treatment, and shot peening as a mechanical surface strengthening treatment to reduce porosity and applying compressive stress on the surface to improve the fatigue limit [10, 11]. For AISI 4140 steel manufactured by PBF-LB under the conditions of internal defects and microcracks, further investigation is needed to verify the closure efficiency of hot isostatic pressing on different types and positions of defects.

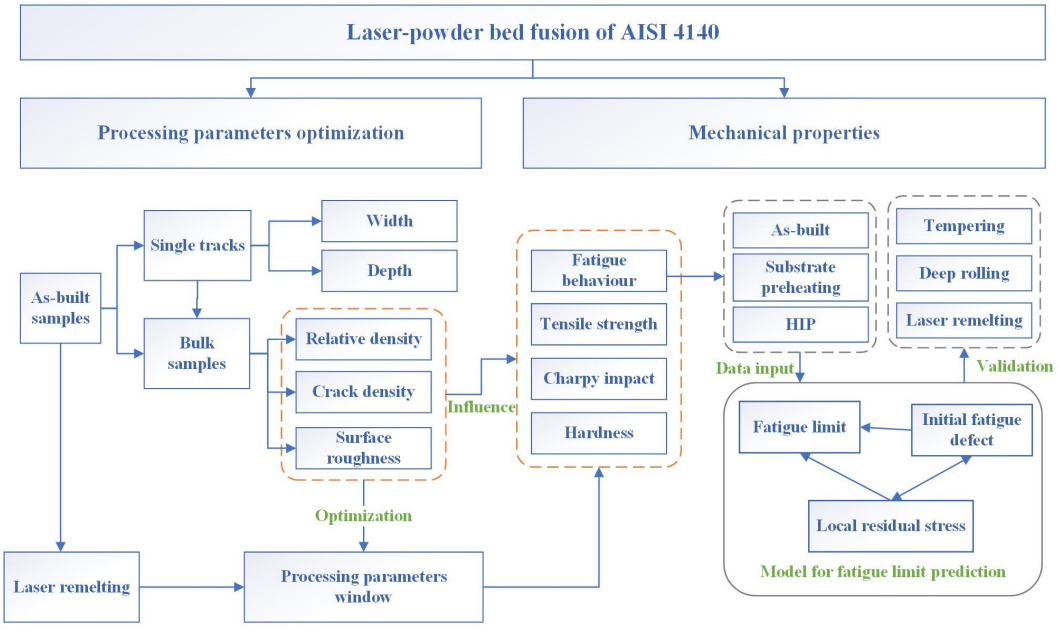

Figure 1.1: The main research routines for PBF-LB AISI 4140 steel.

Therefore, the motivation of this thesis is to systematically investigate the influence of Powder Bed Fusion-Laser Beam process parameters on various types of defects, and further study the impact of process parameters on surface roughness, microhardness, and mechanical properties including tensile and impact performance, and finally the understanding of correlations among processing parameters, defects and mechanical performance. In addition, this thesis will focus on the effects of pores, microcracks, and residual stresses on the fatigue performance of AISI 4140, and use existing fatigue life prediction theory models to predict the fatigue limit from the perspective of killer defect size in combination with residual stresses.

This research thesis will help to understand the role of pores, microcracks, hardness, and surface roughness in determining the mechanical properties when various processing parameters are used in the Powder Bed Fusion-Laser Beam process (Fig. 1.1). Meanwhile, this thesis will also help relevant practitioners or researchers to choose the optimized

PBF-LB processing parameter window for AISI 4140 steel and to promote the future development and improvement of the Powder Bed Fusion-Laser Beam manufacturing process for AISI 4140 steel.

2. State of the art

Additive Manufacturing (AM), also known as 3D printing, has been in development for several decades. This process typically uses Computer-Aided-Design (CAD) softwares to build and slice an object into a few thin layers, and these layers are then deposited layer-upon- layer using different heat sources (e.g., laser or electron beam) to form the final three-dimensional object with the desired precise geometric shapes, as shown in Fig. 2.1.

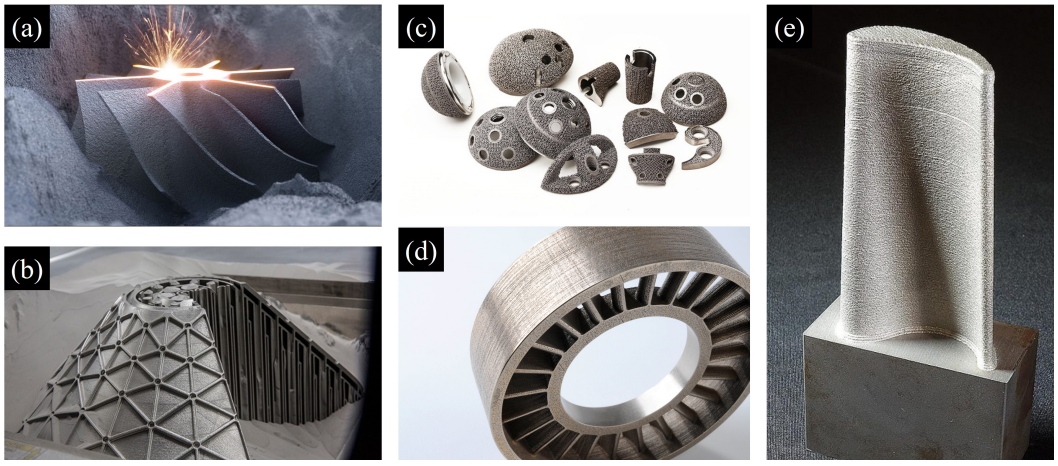

Figure 2.1: Products manufactured by varies additive manufacturing technologies. (a) Powder Bed Fusion-Laser Beam (cite from https://www.3dnatives.com); (b) an oxygen-hydrogen micromixer produced by Powder Bed Fusion-Laser Beam (cite from https://www.ge.com/additive/additive-parts); (c) implants produced by electron beam melting (cite from http://www.arcam.com); (d) oil gas stator produced by binder jetting (cite from https://www.exone.com/parts-and-services); (e) a blade fabricated by directed energy deposition (cite from https://synergyadditive.com/additive-manufacturing).

The exploration of machine concepts and experimental investigations in additive manufacturing dates back to the 1950s - 1970s. However, only the development of related technologies such as stereo lithography appearance in the 1980s made the first commercial system possible. Charles Hull [12] is credited with the invention of the first commercialized AM technology, Stereolithography (SL), and was granted the first patent in Additive Manufacturing in 1986. After two years, 3D Systems realized the commercial use of SLA by inventing the SLA-250, the first commercially available AM machine in the world. In the meantime, another kind of additive manufacturing technology named Fused Deposition Modelling (FDM) was created by Scott Crump [13], which has a lower fabricating cost than SL. C.R.Dechard [14] invented the Selective Laser Sintering (SLS) technology for plastic powder in 1986. Based on the technology of SLS, Fockele and Schwarze (F&S) invented the Selective Laser Melting (SLM) manufacturing method for stainless steel powder in 1999 in collaboration with Fraunhofer Institute for Laser Technology (ILT) [15].

2.1 Additive manufacturing

According to the manufacturing process, AM for metal materials can be divided into three main categories [16], (a) Powder Bed Fusion (PBF), (b) Direct Energy Deposition (DED) and (c) Binder Jetting (BJ).

2.1.1 Powder Bed Fusion (PBF)

Powder Bed Fusion (PBF) uses a laser or electron beam, or other heat sources to scan and melt the desired part cross section in the powder layer. After the scanning of each layer, the position of the build plate is lowered by a distance which equals the layer thickness, and the subsequent layer is filled with new powder by the recoater. Finally, the process is repeated until the part is finished. PBF includes Selective Laser Sintering (SLS), Selective Laser Melting (SLM) or termed Powder Bed Fusion-Laser Beam (PBF-LB), and Powder Bed Fusion-Electron Beam (PBF-EB), as shown in Fig. 2.2.

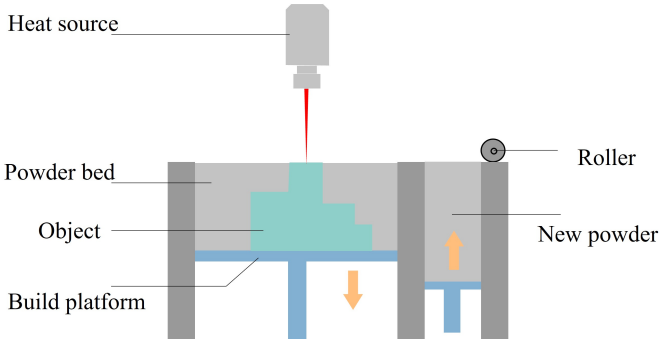

Figure 2.2: Schematics of a powder bed fusion set-up [17].

2.1.1.1 Selective Laser Sintering (SLS)

SLS is normally used to melt plastics or polymer powders in the early stage of powder bed fusion. SLS also can be used to manufacture metal and ceramic parts, but the process can only partially melt powder particles with high melting points or fully melt the powder with relatively low melting points (e.g. polymers) to bind metal particles or ceramic particles together. It is found that the bending strength of the Fe-Cu specimen manufactured by SLS is only 2.41 MPa, which is far below the practical application [18]. Because of the high porosity, low mechanical performances and high surface roughness of parts manufactured by SLS, SLS parts generally need further infiltration with low melting point material (such as bronze) to eliminate defects [19, 20].

2.1.1.2 Powder Bed Fusion-Laser Beam (PBF-LB)

Powder Bed Fusion-Laser Beam (PBF-LB) is widely applied in metal parts production. The laser power for PBF-LB generally ranges from 50 - 1000 W and the scanning velocity ranges from 100 - 2000 mm/s. Additionally, the powder layer thickness is about 20 - 100 µm [21]. One distinguishable difference between the SLS and PBF-LB is that PBF-LB can fully melt the powder to obtain a high relative density.

For PBF-LB, it has the advantage of (1) high complexity of shapes, (2) high relative density (over 99.5%), (3) high geometry precision (minimum about 0.04 mm) and good surface roughness (7-20 µm) [22], (4) relatively low material waste by recycling used powder, (5) high flexibility of parameters control during laser melting of the powder and (6) the build base can be preheated to 200 - 600 °C. However, the disadvantages of the PBF-LB are the low manufacturing efficiency and the low laser absorption rate depending on material types.

2.1.1.3 Powder Bed Fusion-Electron Beam (PBF-EB)

The process of PBF-EB is similar to PBF-LB, except that the PBF-EB process uses a changing magnetic field generated by a magnetic deflection coil to drive the electron beam to move and scan rapidly through the powder layer [23]. Moreover, the manufacturing process of PBF-EB is conducted in a vacuum chamber rather than in the protective inert gas of PBF-LB.

In comparison to PBF-LB, the advantages of PBF-EB are as follows: (1) The absorption rate of the electron beam for metal powder is better than the laser. (2) The ambient temperature of PBF-EB (over 700 °C). Consequently, high ambient temperature leads to low residual stresses in parts manufactured by PBF-EB. (3) It does not consume shielding gas. (4) PBF-EB is more suitable for metal material with high melt points (e.g., Ta alloy). Nevertheless, the disadvantages of PBF-EB are that (1) relatively low moulding accuracy due to the large electron beam and (2) expensive manufacturing cost, due to vacuum environment, e.g..

2.1.2 Directed Energy Deposition (DED)

Directed energy deposition (DED) is also referred to as Laser Engineered Net Shaping (LENS) or Directed Metal Deposition (DMD). The DED process works by depositing metal material (in the form of powder or wire) onto a substrate or the areas of the component that needs repairing through a nozzle mounted on a multi-axis robotic arm (four or five-axis). In the meantime, a heat source (laser, electron beam or plasma arc.) melts the material simultaneously to form dense metallurgical bonding layer by layer, as seen in Fig. 2.3.

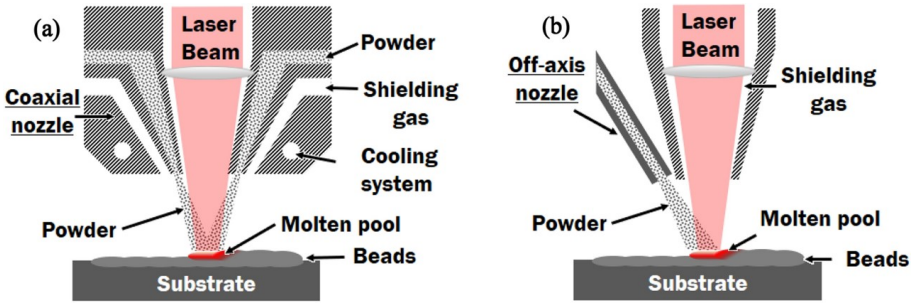

Figure 2.3: Schematics of a DED set-up, (a) coaxial nozzle and (b) off-axis [24].

DED has the advantages in the following aspects: (1) a high degree of space moving freedom, (2) can be used to manufacture functionally graded components, (3) a high build rate, (4) can be employed for repairing, especially for complicate surfaces, (5) manufacturing large scale parts. However, there are still some drawbacks to the DED. For example, (1) requiring a large volume of inert gas and (2) low build resolution.

2.1.3 Binder Jetting (BJ)

In the Binder Jetting (BJ) manufacturing process, the nozzle moves over the build platform to deposit the liquid binding adhesive agent onto the desired areas of the powder bed. When a layer is completed, the build plate moves downwards, and then a new layer of powder is spread evenly on former layers scratched by a roller, and the process is repeated layer by layer.

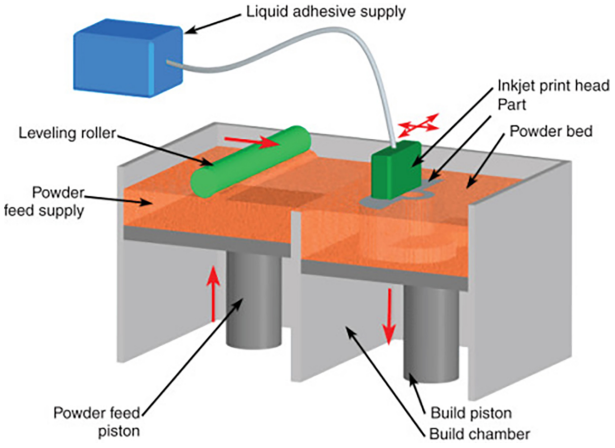

Figure 2.4: Schematics of an BJ set-up [25]. Reproduced with permission from Elsevier.

The binder droplets help the powder layers adhere to each other and finally form the desired parts, as shown in Fig. 2.4. The BJ process is similar to the PBF process, but there is no heat effect in the BJ manufacturing process, thus there is no residual stress in the parts manufactured by BJ. Additionally, the parts manufactured by BJ are generally in a green state, and they need further post-processing (e.g., infiltration process, sintering process) to improve the bonding strength and reduce the porosity.

Advantages: (1) no residual stress, (2) high dimensional accuracy, (3) parts can be made with different colours, (4) manufacturing large-sized parts with complex geometries.

Disadvantages: (1) additional post-processing, (2) higher porosity than the PBF, (3) as-built parts must be kept away from humidity to avoid discolouration, and (4) low mechanical performances because of high porosity.

2.2 PBF-LB of steels

Steels are one of the most popular materials employed in industries, and almost 80 % of metallic parts for engineering purposes are made of steels. Steels usually have good

mechanical properties, as shown in Table 2.1, such as a high yield-to-strength ratio, high impact toughness, and suitable wear resistance due to high hardness. Additionally, the cost of steels manufactured by conventional methods such as casting and forging are low.

Table 2.1: Different steels manufactured by traditional methods. ST-solution, AT-aging

Material	Method	E (GPa)	YS (MPa)	UTS (MPa)	A_f (%)	Hardness	Ref.
Iron	Wrought	-	70-140	240-280	40-60	-	[26]
304L	Annealed	-	168	556	61	136 HV	[27]
316L	Cast	200	365	596	69	-	[28]
17-4 PH	Wrought	199	992	1018	13.4	430 HV	[29]
18Ni-300	Wrought ST	180	760-895	830-1170	6-17	30-37 HRC	[30]
18Ni-300	Wrought AT	183-193	1790	1830-2100	5-11	54 HRC	[31]
H13	Wrought AT	210	1569-1650	1930-1990	9-12	40-53 HRC	[9]
M2	Wrought	-	-	1611	1.3	-	[32]

With the increasing challenges of further improving the mechanical properties of steels, more complicated geometries design requirements, steels fabricated by PBF-LB have raised great interest in academia and industry. In contrast to the conventional method such as casting and forging, the PBF-LB process has high design flexibility, imparting steel parts with low weight but high or similar strength due to finer grains in the microstructure.

Moreover, the PBF-LB process is more environmentally friendly than the conventional method. As reported by Additive Manufacturing Green Trade Association (AMGTA) [33], the optimized AM bracket for the low-pressure turbine module casing of the CF6-80C2B6F turbofan engine is 50 % lighter than the original version, weighing just 0.063 Kg. The report also estimates that carbon emission will decrease by 13376 Kg for every 1 Kg of weight reduction.

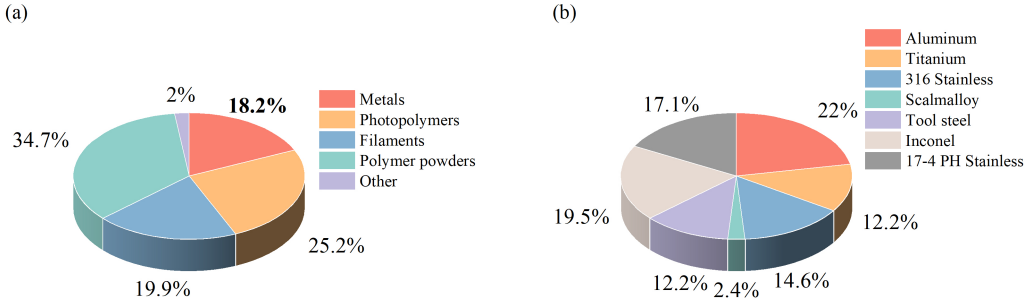

Figure 2.5: The market share of materials applied in the additive manufacturing [34]. (a) Main material groups and (b) metals.

Up to date, although steels occupied around 44 % market share in the metals additive manufacturing field, metals took up only a small proportion of the whole additive manufacturing market share (18.2 %), as shown in Fig. 2.5. Only a few types of steels for the PBF-LB have been investigated thoroughly, for instance, stainless steel (316L, 17-4 PH) and tool steel (H13). For other types of steel, the related investigating studies are scarse.

2.2.1 Feedstock

The powder used for the PBF-LB process is normally produced by water atomization, gas atomization and plasma atomization (Figs. 2.6 - 2.7). Different powder manufacturing methods could result in different powder characteristics. In comparison with the gas atomization process, water atomization is the simplest and therefore very cost-effective method for powder production. Therein, a water jet is used to atomize liquid metal in the chamber. However, the water atomization process may maintain high oxygen content in powder, which may form oxides and further influence the relative density and mechanical performance of the parts.

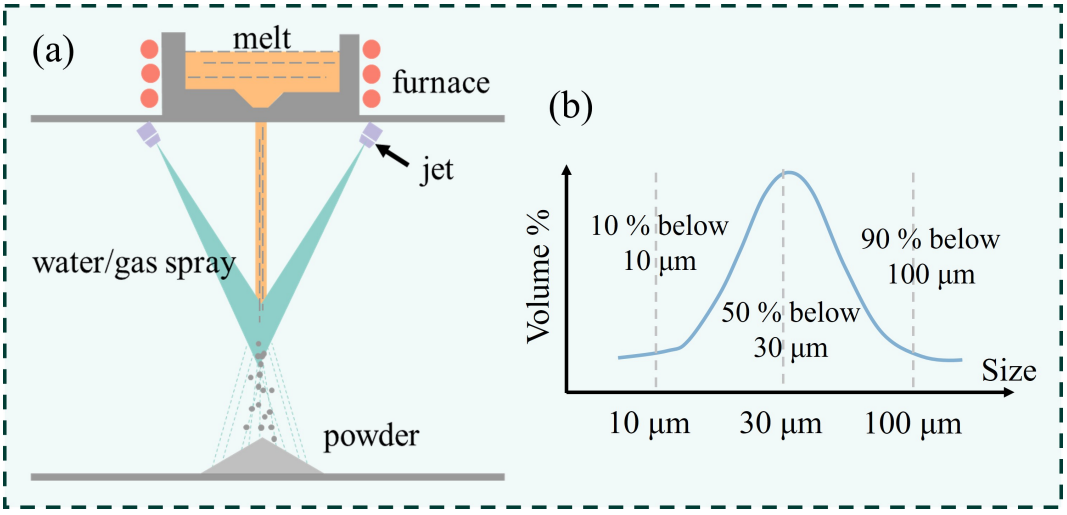

Figure 2.6: (a) Schematic illustration of the powder manufactured by gas/water atomization, and (b) the distribution of powder size [35].

Moreover, water-atomized powder particles often exhibit an irregular morphology, which could be attributed to the fast cooling and solidification rate during atomization. The powder used for PBF-LB should have geometries with good sphericity to achieve good powder distribution during the interaction with the laser. As a result, water atomization is suitable for steels. Gas atomization possesses advantages such as high production yield, high efficiency, small average powder particle size, and small impurity sizes. Therefore, gas atomization is suitable for reactive materials, such as Ti and Al alloys.

Plasma atomization involves introducing metal and its alloys in the form of wires or rods into the converging center of a plasma jet. The atomization process occurs as a result of impact within the ultrasonic plasma jet, followed by cooling and solidification to form spherical powder (Fig. 2.7). In comparison to gas atomization, plasma atomization consumes less gas, exhibits fewer powder hollow defects, and produces highly spherical powder, resulting in improved flowability [35]. However, when compared to water atomization and gas atomization, plasma atomization has a lower production efficiency.

Nitrogen and argon are two inert gases commonly used in gas atomization. On the one hand, the atomization process conducted by inert gas is helpful to reduce the oxygen content in the powder. On the other hand, the choice of different types of inert gas could

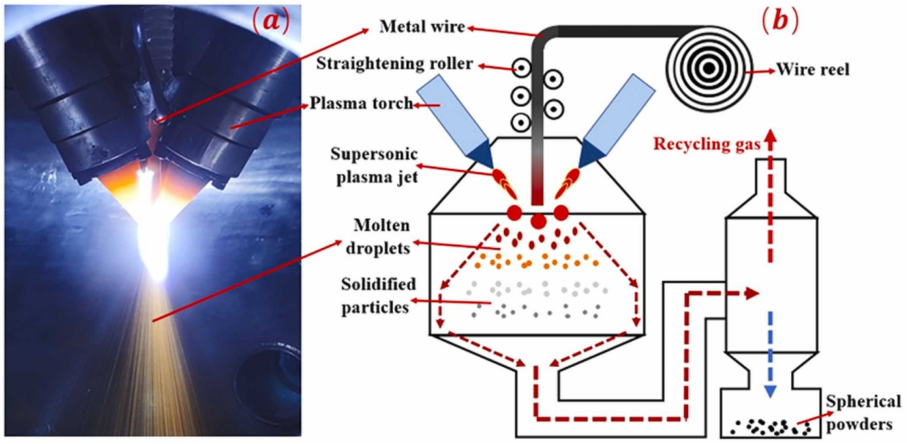

Figure 2.7: (a) Photo of the plasma atomization equipment, and (b) schematic illustration of the plasma atomization equipment [36]. Reproduced with permission from Elsevier.

even influence the microstructure of the final parts.

Gao et al. [37] studied the difference between nitrogen and argon in gas-atomized 316L steel powder. Their results indicate that powder atomized by argon is more spherical than nitrogen-atomized powder. The investigation of the influence of nitrogen and argon atomized 17-4 PH steel powder on microstructure from Starr et al. [38] revealed that parts manufactured by argon atomized powder contained a large proportion of martensite. In contrast, parts manufactured with nitrogen atomized powder showed a higher fraction of the austenitic phase. They explained the possible reason could be that the high content of residual nitrogen in the powder could stabilize the face-centred cubic phase and retain austenite in the microstructure.

Some other studies showed that powder granulometry is also an important factor affecting laser absorption, flowability, surface quality, etc. Olakanmi et al. [39] investigated the laser sintering of blended Al-Si powders. It is found that fine powder has a higher amount of laser absorption than coarse powder because of the large surface area of fine powder. Moreover, Dietrich et al. [40] found that fine powder granulometry can lead to high surface quality. Parts produced by the powder with a wider distribution have better side surface roughness than the narrow grade. However, it is easier to agglomerate when the powder particle size is smaller than a certain value (such as 10 µm), thereby inversely deteriorating the flowability. Additionally, Spierings et al. [41] proposed requirements for spreading powder in thin layers according to Eq. 2.1,

$$\frac{t_{layer}}{D_{90}} \approx 1.5, \frac{D_{90}}{D_{10}} \approx 5, D_{10} > 5 \tag{2.1}$$

To avoid powder agglomeration, the powder layer thickness should be 50 % higher than the size of the coarse fraction and the size ratio between the coarse and fine fraction is about 1:5.

In the aspect of mechanical performances, Tan et al. [42] overviewed the influence of

powder size distribution on parts performance, and they concluded that specimens manufactured by a wide distribution of powder size have lower strength but high elongation to fracture, and the narrowly distributed powder may produce high mechanical strength due to finer microstructure. Additionally, Vunnam et al. [43] reported that the as-built microstructure of 17-4 PH steel could be affected by powder chemical composition directly in PBF-LB. They found that the volume fraction of residual δ-ferrite varied from 95 % to less than 25 % depending on the Cr_{eq}/Ni_{eq} (a chromium to nickel equivalent value) in the powder. δ-ferrite grain refinement could occur with around 75 % volume fraction of transformed martensite when the $Cr_{eq}/Ni_{eq} \leq 2.36$.

2.2.2 Defects in PBF-LB

The interaction between the laser and the material forms a local melt pool, and some defects may occur during this process, as shown in Fig. 2.8. In the PBF-LB process, different materials require different processing windows to eliminate possible defects. Processing parameters, including laser power P, laser scanning speed v, hatching distance h and layer thickness t, play the most important roles in fabricating parts with a minimum of defects, and the typical process window for the PBF-LB is shown schematically in Fig. 2.9.

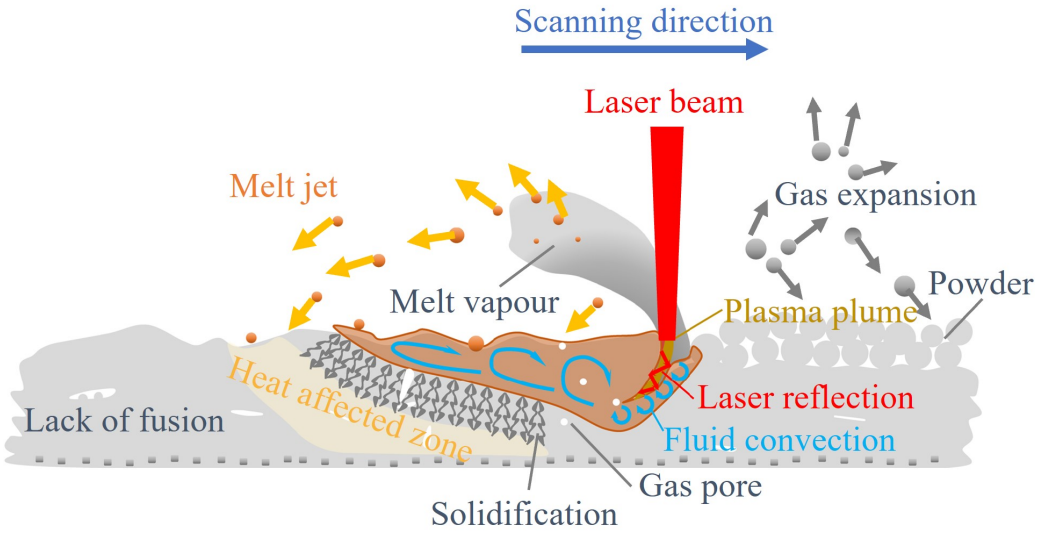

Figure 2.8: Schematic illustration of the interaction between the laser and the materials during the PBF-LB manufacturing process [44].

Pores (keyhole pores, lack of fusion pores and gas-entrapped pores), balling effect and cracking are the dominant flaws in the PBF-LB, which further deteriorate the mechanical performance of the final parts. In this section, different types of defects will be classified, followed by an explanation of how processing parameters influence these flaws and the methods that can be employed to mitigate defects in the PBF-LB manufacturing process.

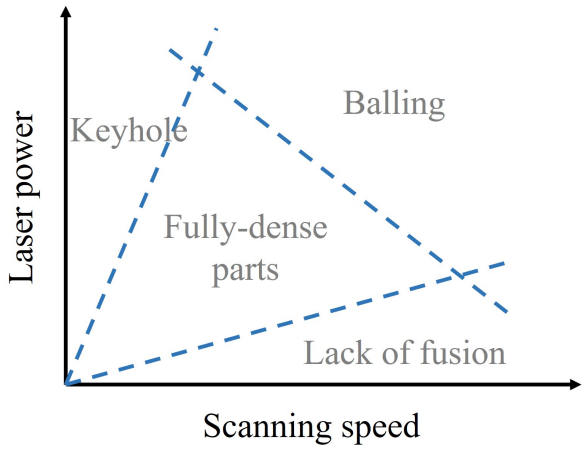

Figure 2.9: The typical processing window for defects distribution in PBF-LB [45].

2.2.2.1 Keyhole pores

The keyhole welding mode is generally caused by high energy input, which leads to a deep melt pool with highly complex meltpool fluid dynamics and internal gas flow. Therein, metal vapor, induced by the vaporization in the melt pool, can be trapped especially at turning points, hence forming keyhole-induced pores with spherical shapes, as seen in Fig. 2.10a.

Conditions with high laser power combined with low scanning speed easily generate keyholes, so low laser power or fast scanning speed should be chosen to reduce the input energy to eliminate keyhole pores. In order to investigate and reveal the formation mechanisms of keyhole pores, plenty of researchers used the in-situ X-ray computed tomography (X-CT) method to monitor the laser additive manufacturing process. Martin et al. [46] studied the dynamics of pore formation using X-CT in PBF-LB. It is found that keyhole-induced pores are easy to form at laser turn points because of the emergence and subsequent collapse of a deep keyhole depression caused by the deceleration and acceleration of the laser beam. Cunningham et al. [47] used ultrahigh-speed synchrotron X-ray imaging to quantify keyholes. They proposed that the keyhole does not precisely correlate with the shape of the melt pool, and keyhole pores could be generated before visible trenching in the melt pool. Bayat et al. [48] investigated the formation of the keyhole and keyhole-induced porosities of Ti6Al4V alloy. They proposed a new mechanism that keyhole pores are mostly formed due to the occurrence of local cold zones with higher surface tension and insignificant recoil pressure.

Li et al. [49] used the computational fluid dynamics (CFD) model to investigate the keyhole dynamics and built the correlation among forces and melt pool/keyhole motions. Unfortunately the insufficient aspect was the lack of related experimental data in their work. Additionally, Gordon et al. [50] studied the relationship between keyhole defects and the melt pool, and they found that keyhole pores are easy to occur when the angle of the front melt pool is larger than 77°.

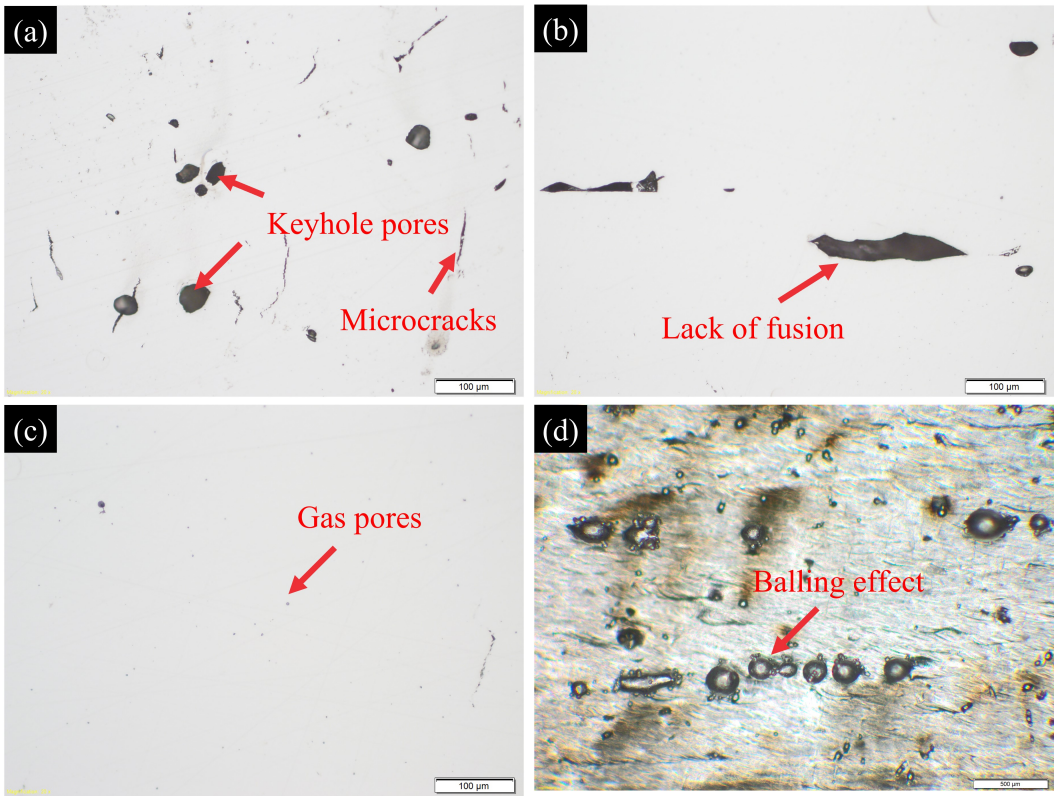

Figure 2.10: Possible defects occuring during the PBF-LB process due to inappropriate parameters. (a) Keyhole pores, (b) lack of fusion, (c) gas pores and (d) balling effect.

2.2.2.2 Lack of fusion pores

Lack of fusion (LoF) is the most detrimental defect observed in the metal PBF-LB, which is generally caused by insufficient fusion between adjacent layers or tracks, leaving voids with irregular shapes in the parts, as shown in Fig. 2.10b. Inappropriate processing parameters (laser power, laser scanning speed, hatching distance and layer thickness) all can result in LoF defects.

When the laser power is low, on the one hand, the melt pool could not overcome the surface tension and thus form discontinuous balls (balling effect). On the other hand, the shallow melt pool caused by the low input power may only melt part of the powder layer and leave unmelted powder particles underneath.The existing balling on the melted layer is prone to induce LoF defects in the following layers. Furthermore, a considerable hatching distance could cause the powder bed below the overlap region to be unmelted.

The LoF porosity also could be increased drastically with increasing the powder layer thickness, and it can be ascribed to the fact that the melt pool is not bonded to the former solid layer well when the powder thickness is too high (in general, the suitable value for layer thickness is 30-50 µm). Laleh et al. [51] studied LoF pore structures in PBF-LB of 316L steel. It is found that LoF pores could also be caused by oxides, which reduce the wetting of the molten material and prevent them from being consolidated. They also concluded that LoF defects caused by spattering may be the dominant type

of LoF structures of specimens with over 99 % density but could be eliminated with the appropriate processing parameters, especially a correct shielding gas flow.

2.2.2.3 Balling

As aforementioned, the influence of the balling effect is generally in the form of LoF defects inside the parts. It is also in the form of rough surface quality on the top layer. The fast scanning speed could cause the melt track to be unstable and thus tend to break it up into spherical balls during the scanning process due to the Plateau-Rayleigh capillary instability [52], as shown in Fig. 2.10d. Low laser power strongly affects balling effect because the melt pool could not overcome high surface tension and form balls [49]. Moreover, balling could also occur when the wettability between the current melt pool and the solid layer is poor (for example through surface impurities or oxide layers).

Besides LoF defects, balling is also responsible for the humping or ripple effects, which deteriorate the surface quality. Yadroitsev et al. [53] reported that the high energy density is beneficial in reducing the tendency of balling by forming the melt pool with wide and large geometry, which increases the liquid flowability and decreases the viscosity. Yasa et al. [54] investigated the remelting process on defects in 316L steel. Their work showed that remelting could refine the microstructure, eliminate LoF pores, and enhance surface roughness. However, remelting will cost more time. Li et al. [49] thought the balling phenomenon could be restrained by decreasing the oxygen content in the atmosphere due to the oxidation of the molten pool. It should not be a problem nowadays because most printers can well control oxygen content below 0.01 %.

2.2.2.4 Gas pores

The size of the gas pore is pretty tiny (around 5-20 µm) compared to that of LoF and keyhole pores, and is generally displayed as a spherical shape, as shown in Fig. 2.10c. Most of gas pores are caused by the entrapment of the shielding gas in the melt pool from the manufacturing chamber, or the gas entrapped inside powder particles. Gas-entrapped pores could only be reduced if they can float up to the top surface.

Although it is difficult to eliminate all gas pores inside the parts, slow cooling and solidification rates may help these gas pores coalesce and finally float to the surface of the melt pool. Moreover, Lv et al. [55]. reported that the thermocapillary force induced by the high-temperature gradient could help the remaining gas escape from the melt pool in studying Ti6Al4V manufactured by PBF-LB.

2.2.2.5 Cracking

The occurrence of cracking during PBF-LB manufacturing process is generally associated with high residual stresses. Residual stress shifts from compressive to tensile states during the heating and cooling stages of the laser interaction area, as shown in Fig. 2.11. Moreover, the steep temperature gradient of about 10^4 °C/mm [58] and phase transformation also result in high thermal residual stress, which further increase the likelihood of cracking in components.

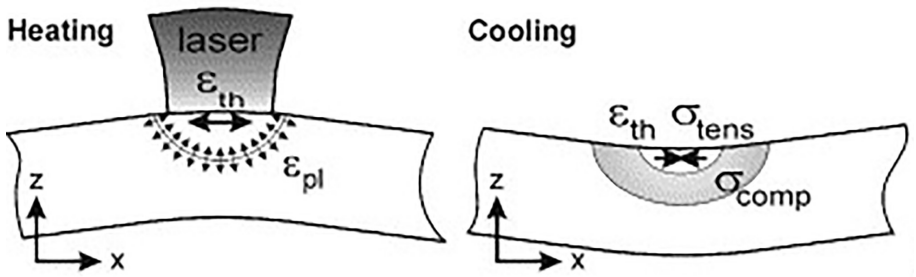

Figure 2.11: The schematic illustration of residual stress states during PBF-LB heating and cooling stages [56]. Reproduced with permission from Elsevier.

Solidification cracking

In the PBF-LB process, there are two main microcracking mechanisms in the part, namely, solidification cracking and liquation cracking. As shown in Fig. 2.12a, solidification cracking happens in the solidifying melt pool or the mushy zone near the end of solidification, and it results from insufficient feeding of remaining liquid films in the interdendritic region to accommodate the solidification shrinkage strain, thereby acting as crack initiation sites.

Consequently, metal with a wide range of solidification temperatures is more susceptible to solidification cracking than those with a narrow temperature range [59]. It is also found that this type of cracking has a typical feature, leaving a large gap between the two surfaces with an irregular shape. Moreover, the two surfaces do not necessarily appear in the same morphology that can close up together [57].

Liquation cracking

Liquation cracking occurs in the heat-affected zone of the former layer or track during the thermal cycles in the PBF-LB process (Fig. 2.12b). It mostly happens when chemical elements with low melting points are segregated around the grain boundary or the segregation of impurities which reduces the melting temperature in the local region and hence forms a liquid film again.

It is found that S and P elements in steels could broaden the solidification temperature range, which increases the cracking susceptibility [60, 61]. Due to the solidification shrinkage, these areas with liquid films could accelerate crack propagation.

Solid-state cracking

In contrast to the two kinds of cracking introduced above, solid-state cracking occurs totally in the solid state at a relatively low temperature. It happens because of the brittleness of the metals in interaction with large residual stresses, as shown in Fig. 2.12c. Strain-age cracking (SAC) and ductility-dip cracking (DDC) are two typical mechanisms for solid-state cracking [62]. SAC generally happens in Ni-base superalloys, so it will not be discussed further here.

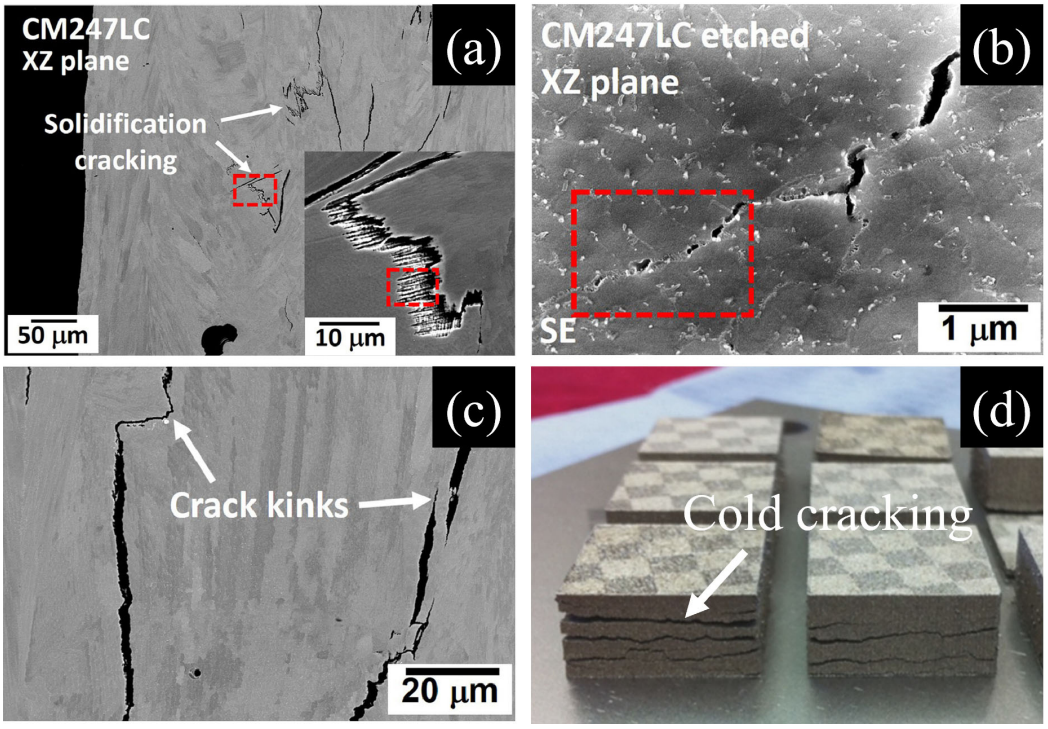

Figure 2.12: (a) Solidification cracking, (b)liquation cracking, (c) solid-state cracking and (d) cold cracking [57].

DDC occurs when the local material encounters a steep drop in ductility at a very narrow elevated temperature range during the repeated intrinsic heat-treatment cycle from layerwise PBF-LB. This phenomenon may induce stress concentration at grain boundary triple points due to grain boundary sliding, leading to the final cracking. It is reported that coarse grains and high-angle boundaries are more susceptible to DDC than finer grains [59]. There are some features of solid-state cracking that can be distinguished from other types of cracks. For example, the surface of the solid-state crack is generally identical in shape on both sides. Moreover, the crack is straight and clean when observed from microscopy. Additionally, cracks with sharp kinks are also a feature of solid-state cracking.

Steels with martensitic microstructures are prone to cracking in the microstructure due to the expansion during martensitic transformation combined with thermal residual stress due to fast liquation and solidification. Moreover, the microsegregation of elements could increase the susceptibility of solidification cracking by increasing the solidification temperature range, as previously discussed.

It is also found that grain refinement is a promising method to reduce hot cracks in PBF-LB aluminium alloys, which could accommodate more strain induced by the thermal stress [63]. However, it is tough to refine the martensitic microstructure in the PBF-LB process. Substrate preheating is hence the most widely used method to eliminate microcracks, especially high carbon martensitic steels, by reducing the temperature gradient in the PBF-LB process.

Altogether, processing parameters, microstructure, chemical composition and powder bed

temperature all could influence the formation of microcracks in the PBF-LB process. High laser power with slow scanning speed induces not only the keyhole mode but also severe hot cracking due to high thermal residual stress. However, the LoF pore could arise from insufficient input energy or balling effects. Herein, it is necessary to find a trade-off between low porosity and low crack density of workpieces manufactured by PBF-LB.

2.2.2.6 Other challenges

Besides defects stemming from process parameters and the materials themselves, there are currently issues associated with the performance of powder bed fusion equipment.

Shielding gas disturbances

In areas with low shielding gas flow, the spatter generated during manufacturing cannot be dispersed, leading to the formation of black residue and ejected melt landing back on top of the layer with a diameter of up to 200 µm. The accumulation of multiple layers of black residue can result in manufacturing defects.

Optical path contamination issues

During long-term continuous manufacturing, localized areas may exhibit scanning anomalies, with the power output of the laser beam seemingly diminished, preventing dense sintering. This issue might be caused by significant contamination of the protective lenses inside the chamber. Additionally, heating issues of the optical system slowly shifting the focal point out of the layer plane could be the other factor leading to diminished power output.

Multi-beam stitching issues

To increase the efficiency of powder bed fusion, multi-beam manufacturing is becoming increasingly prevalent. However, multi-beam manufacturing can result in potential multi-beam stitching issues, which are related to the temperature drift during long-term operation of the galvanometer and the stability of its mechanical system.

2.2.3 Microstructure

An overview of steel microstructures in AM can be seen in Fig. 2.13. The microstructure of stainless steel could be austenite (304, 316L) and martensite phases (15-5 PH, 17-4 PH). The main phases of tool steel consist of martensite, carbides and residual austenite depending on the PBF-LB manufacturing conditions. Although the martensitic steel includes carbon-free (15-5 PH, 17-4 PH) and carbon-bearing martensitic steels, this study mainly focuses on carbon-bearing martensitic steels manufactured by PBF-LB (AISI 4140), so only the microstructure of carbon-bearing steels will be further introduced.

The effect of alloying elements on the microstructure of steels and nickel alloys in welding can be derived from the Schaeffler diagram (Fig. 2.14), in which the microstructure is depent on the chromium equivalent and nickel equivalent. For AISI 4140, the chromium

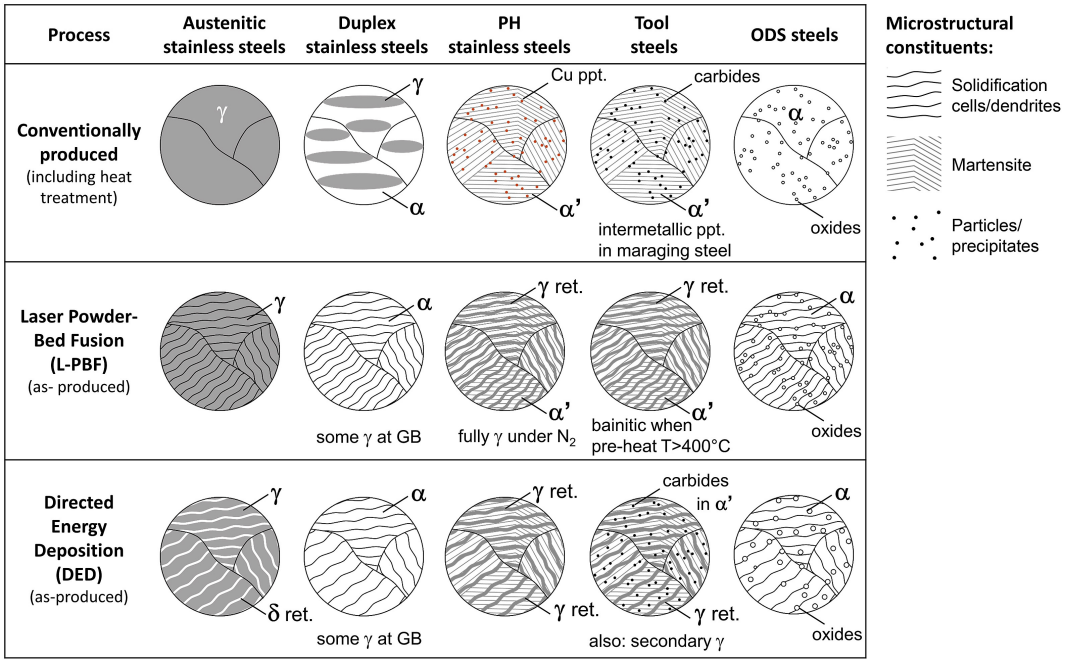

Figure 2.13: Overview of microstructure in different steels manufactured by two additive manufacturing methods including PBF-LB and DED, compared to conventional manufacturing methods [9]. Reproduced with permission from Elsevier.

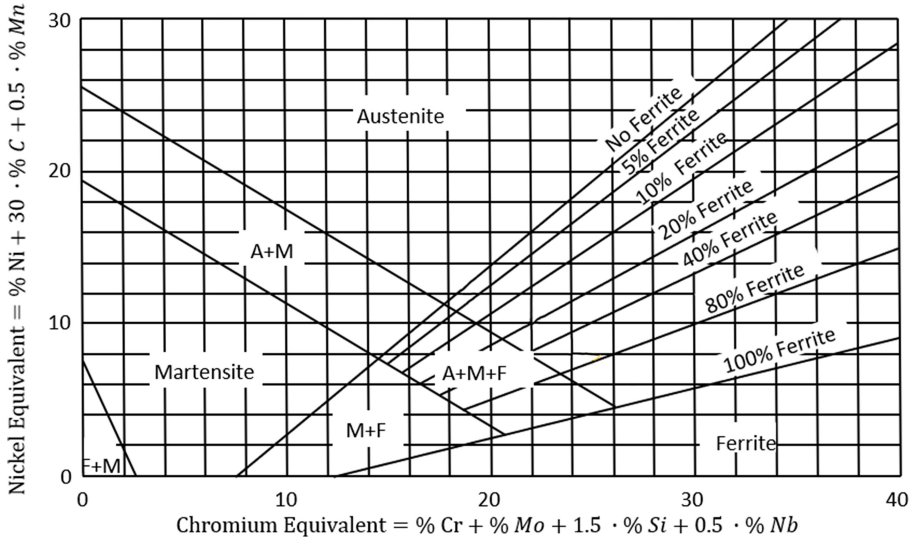

Figure 2.14: The Schaeffler diagram showing the relationship between element composition and phase [64]. Reproduced with permission from Elsevier.

equivalent and nickel equivalent is 1.6 and 12.15, respectively, suggesting the microstructure should be martensitic. Moreover, the size of the solidification microstructures of the PBF-LB is determined by the cooling rate of the melt pool. A higher cooling rate generally results in fine grains (1-100 µm), and a lower cooling rate results in coarse microstructures. In detail, the temperature gradient (G) and the growth rate of the solidification interface (R) affect the solidification mode. For example, the range from planar, cellular, columnar dendritic to equiaxed dendritic microstructures could be produced with different G/R, as shown in Fig. 2.15.

Due to the extreme cooling rates (up to 10^6 K/s), the microstructure of medium carbon steels manufactured by PBF-LB mainly consists of fine martensite laths (1-10 µm) supersaturated with carbon. During the PBF-LB process, regions in the vicinity of the melt pool could be tempered by repeated heating/cooling cycles, thereby forming tempered martensite with carbide precipitation and decreasing the hardness compared to that of fresh martensite, which is consistent with the results from Hearn et al. [65] in studying a series of low-alloy steels (AISI 4130, 4140, 4340 and 8620) manufactured by PBF-LB. Damon et al. [66] studied AISI 4140 low alloy steel processed by PBF-LB and concluded that the temperature of reheating a subsequent layer is approximately 715-805 °C by utilizing the Hollomon-Jaffe equation. Moreover, they did not report any retained austenite in the as-built specimens. Deirmina et al. [67] studied H13 steel manufactured by PBF-LB, and they reported the phases in the microstructure were mainly martensite and retained austenite (RA) at the cellular boundaries. They ascribed the RA to the chemical stabilization of austenite due to the intercellular segregation of alloying elements.

Last but not least, the base preheating temperature also influences the microstructure. When the preheating temperature is below 200 °C, the temperature is still below the martensite transformation starting point, and the microstructure is mainly martensite. However, when the preheating temperature exceeds 400 °C, the phases tend to form bainite instead of martensite in the microstructure. Mertens et al. [68] investigated different base preheating temperatures on the microstructure and mechanical performance of H13 steel manufactured by PBF-LB. Results show that specimens preheated at 400 °C have a more homogeneous microstructure and tensile properties than that with low preheating temperatures or without preheating.

2.2.4 Laser remelting

Optimizing processing parameters could be the most convenient and effective method to reduce microstructural defects. However, processing parameter optimization may not always work effectively for all materials to make surface roughness and porosity to meet the requirement. Post-treatment such as machining and hot isostatic pressing (HIP) is thus the commonly utilized method to ameliorate surface roughness and relative density, respectively. Besides, laser remelting (LR) is another promising in-suit method to improve the surface quality and eliminate defects simultaneously by scanning and melting solidified powder layers more than once before filling the new powder layers in the PBF-LB manufacturing process.

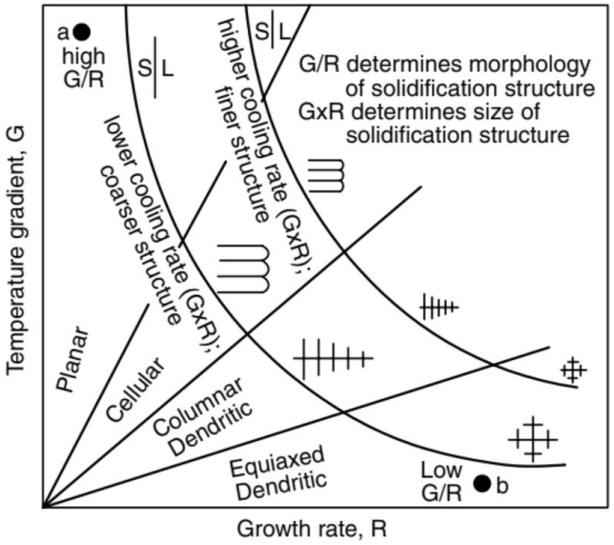

Figure 2.15: The relationship between G/R and the final microstructure [69]. Reproduced with permission from Springer Nature.

It has been demonstrated by Demir et al. [70] that LR can improve surface roughness and reduce residual defects by releasing possible entrapped gas in the microstructure. Qiu et al. [71] investigated the influences of LR on the reduction of defects during the PBF-LB of 316L steel, and they found that pores near the upper layer and vacuum pores in specimens can be eliminated by LR.

Some efforts have been put forward to investigate the dominating processing parameters affecting LR. Ghorbani et al. [72] studied parameters optimization of the LR in PBF-LB 316L inclined parts. It is found that the laser exposure time plays the most important role in affecting surface roughness, and hatching distance did not influence the LR results significantly. Moreover, they suggested that the processing parameters of LR should be optimized separately to get a satisfying remelting effect. Yasa et al. [73] also reported that scanning speed was the most effective parameter to obtain specimens with high relative density in investigating the influence of LR on density, surface quality and microstructure of 316L and Ti6Al4V manufactured by PBF-LB. Besides, they found that LR can enhance the surface quality by up to 90 %, and the microhardness was also improved due to refined cell sizes.

Zhou et al. [74] have drawn similar conclusions in studying the mechanical performances of remelted AlSi10Mg. They found that LR can decrease the average grain size up to 28.79 % and improve the microhardness by 10.2 %, but the ultimate tensile strength and yield strength were slightly reduced. Additionally, they reported that the residual stress after LR is still in the tensile regime. Song et al. [75] found that LR could slightly coarsen the average grain size in the heat-affected zone, and the formation of more nanoprecipitates induced by the intrinsic heat treatment effect due to LR is beneficial to improve the microhardness in manufacturing 18Ni-300 maraging steel by PBF-LB.

2.2.5 Mechanical properties of steels

2.2.5.1 Charpy impact toughness

The Charpy impact test is a commonly used method for evaluating toughness, with high impact energy indicating high impact toughness. Various factors such as crystallographic textures, grain size, chemical composition, and heat treatment methods have been found to significantly affect the impact toughness of conventionally manufactured metals, as reported in literature [76, 77, 78].

However, only limited studies on metal materials manufactured by PBF-LB have reported Charpy impact tests in detail. Saby et al. [79] found that there is an inverse relationship between microhardness and impact toughness in metal materials. Specifically, their study revealed that higher microhardness, such as those with 53 HRC, tend to exhibit lower impact toughness of around 15 J, while those with lower microhardness, such as 40 HRC, tend to have higher impact toughness of approximately 100 J. Wang et al. [80] compared the Charpy toughness of PBF-LB 30CrMnSiA steels with different heat treatment, and their results show that PBF-LB parts have the highest impact energy, 34.8 J, when annealed at 900 °C. Huang et al. [81] investigated the anisotropic toughness of a kind of low activation martensitic steel (CLAM) manufactured by PBF-LB. Their results show that the anisotropy in microstructure and the orientation of defects at the interface of layers were the primary reasons for the anisotropic toughness observed in the material. Seede et al. [82] found that as-built samples displayed a lower impact toughness of 27.8 J compared to as forged specimens (about 49 J) in studying the AF9628 steels manufactured by PBF-LB, and they ascribed the differences to about 12 % reduction in the carbon content during the PBF-LB. Moreover, they did not find any improvement in impact toughness after a stress relief heat treatment.

2.2.5.2 Tensile strength

Tensile testing is the most widely used method to quantitatively characterize and compare the strength and plastic deformation behaviour of materials by measuring the maximum amount of load that the material can withstand before it breaks or fails. Since microstructures of components produced by the PBF-LB process are much finer than conventional methods because of the quick melting and solidification, the ultimate tensile strength and yield strength of steels manufactured by PBF-LB is comparable to or even higher than the conventionally manufactured counterparts due to the fine grain strengthening effect.

Here some medium carbon steels manufactured by different additive manufacturing technologies are summarized in Table 2.2. It can be observed that tensile specimens built in the transverse orientation exhibit higher tensile properties than specimens built in the vertical orientation, reflecting the effect of the microstructural anisotropy inherited from the directional and layerwise build process. The tensile strength of AISI 4130, 4140, 4340 varies from 1000 to 1500 MPa, and the elongation ranges from 2.3 to 17 %.

The tensile strength of PBF-LB parts is influenced by defects in the microstructure, such as porosity and cracks. Significant LoF defects could result in brittle fracture, while micropores may grow and coalesce together, resulting in the final ductile fracture with dimple

Table 2.2: Summary of tensile properties of medium carbon steels manufactured by different additive manufacturing technologies.

Material	Direction	Method	YS (MPa)	UTS (MPa)	Elongation (%)	Ref.
AISI 4140	transverse	PBF-LB	1365.5±52	1526±49	13.8±0.9	[83]
	vertical	PBF-LB	1281±4.6	1438±3.6	12.4±1.8	
AISI 4130	transverse	PBF-LB	1249±15	1419±30	3.4±0.6	[84]
	vertical	PBF-LB	1166±5	1277±7	6.3±0.9	
AISI 4340	vertical	DED	1310	1372	16-17	[85]
AISI 4140	vertical	PBF-LB	1175±5	1280±10	7.2±2.8	[66]
	vertical	PBF-LB,QT+450	1290±10	1325±5	4.2±2.6	
AISI 4140	transverse	PBF-LB	1365	1526	13.8	[86]
	vertical	PBF-LB	1281	1438	12.4	
16MnCr5	vertical	PBF-LB	1050	1050	67.5	[87]
AISI 4340	vertical	PBF-LB	1151	1213	14.9	[88]
AISI 4140	vertical	PBF-EB	-	850	12.5	[89]
AISI 4130	vertical	PBF-LB	955±19	1040±16	2.8±1.2	[90]

features. It is reported that a high remaining porosity, about 2.4 %, leads to brittle failure modes with significantly reduced elongation [5]. Seede et al. [91] investigated the influences of processing parameters and strategies on the tensile performance of an ultra-high strength martensitic steel manufactured by PBF-LB. Their results show that higher ductility was observed along the building direction than in the horizontal direction due to different extent of tempering effect. Dilip et al. [92] also got a similar conclusion in studying HY100 steel manufactured by PBF-LB. Moreover, they found that compared to conventionally processed specimens, the PBF-LB specimens have higher ultimate tensile strength and yield strength but lower elongation. Kim et al. [93] pointed out that LoF pores and oxide inclusions are the main reasons for premature failure in additively manufactured AISI 4140 steels. An investigation reported by Mazur et al. [94] on H13 steel manufactured by PBF-LB showed that the tensile strength of as-built specimens dropped around 30 % because of high residual stress in as-built PBF-LB specimens, and the tensile strength recovered with a stress relief heat treatment.

2.2.5.3 Fatigue strength

Fatigue failure is one of the primary failure modes of engineering materials, which typically occurs under cyclic loading conditions with low stresses. The fracture of the workpiece due to fatigue failure usually happens suddenly after a long period of cyclic loading. It is still challenging to predict fatigue failure since killer defects for cracking initiation are typically very small, on the order of a few microns. In addition, fatigue fracture can lead to serious safety accidents, such as the derailment of a German ICE train in Eschede on June 3, 1998, caused by fatigue fracture of a wheel rim (Fig. 2.16), which resulted in 101 deaths and 88 injuries. Therefore, studying metal fatigue behavior has significant societal economic and safety implications.

For materials manufactured by PBF-LB and used in structural applications, the service life and durability of workpieces, especially when repeatedly undergoing cyclic loads, are of significant concern. However, it has been widely reported that PBF-LB parts generally exhibit a fatigue strength lower by about 30 %-50 % compared to CM parts. The fatigue

Figure 2.16: The severe transportation accident caused by metal fatigue fracture. The figure is cited from www.cdstm.cn.

performance of materials is closely linked to defects produced during the manufacturing process [95]. Flaws, such as LoF pores and microcracks, are common defects occurring in the PBF-LB process compared to the CM methods (casting, forging), which could explain the low fatigue strength in PBF-LB components.

The impact of the aforementioned defects on the fatigue strength of metals produced via AM has become an increasingly hot topic in the research of different materials, such as Ti-6Al-4V [96, 97], AlSi10Mg [98], stainless steel 316L [99, 100], martensitic steel H13 [101], etc. Current studies on the fatigue properties of PBF-LB metal specimens show that processing parameters, built orientation, surface roughness and heat treatment status can significantly affect fatigue performance [102, 103]. Yadollahi et al. [104] reported that horizontally built specimens show a superior fatigue performance compared to perpendicular ones, which can be ascribed to the advantageous direction of manufacturing-induced defects concerning the loading direction. Sanaei et al. [95] reviewed and studied Ti-6Al-4V manufactured by PBF-LB. Their results demonstrated that surface roughness is the primary factor affecting fatigue performance, even in specimens with large internal defects. They also found that the fatigue strength of as-built specimens is only around 50 % of that of the machined ones, and the high surface roughness could act as multiple stress concentrators, namely notch effects, to promote crack initiation, resulting in the low fatigue strength of as-built specimens [105].

With regard to defect mitigation, post-heat treatment methods such as hot isostatic pressing (HIP) and shot peening have also been explored as means of improving the fatigue limit of PBF-LB specimens. Molaei et al. [10] studied the influence of HIP on fatigue behaviours of PBF-LB Ti-6Al-4V. They found that fatigue life was improved due to the closure of manufacturing defects and the relaxation of detrimental tensile residual stress after the HIP heat treatment. Kunz et al. [106] compared different heat treatments on the fatigue strength of AISI H13 steel manufactured by PBF-LB. Their results suggested that the fatigue strength can reach up to 972 MPa after HIP+HT (hardening and tempering) treatment.

However, some researchers draw different conclusions. Chastand et al. [107] found no major differences between specimens in two different fabricating directions (vertical and transverse direction) in studying Ti-6Al-4V manufactured by PBF-LB. Stern et al. [108] reported that only pores with a flat morphology and connected to the surface could deteriorate fatigue strength. For other defects, such as gas-entrapped pores, an influence on performances can be negligible. Riemer et al. [109] concluded that high cycle fatigue performance was not affected by pores and internal stresses but by the high ductility of specimens in PBF-LB 316L stainless steel. In conclusion, the effects of defects (including size and location) on fatigue strength and their mechanisms in different PBF-LB material states remain to be fully elucidated.

Fatemi et al. [110] studied the influence of HIP on the fatigue strength of Ti-6Al-4V, and they concluded that there was no significant improvement in fatigue performance when tested with a rough as-built surface. Plessis et al. [111] further pointed out that defects open to or located near the surface were difficult to get closed. Consequently, the HIP process should be combined with suitable surface roughness to improve the fatigue strength of materials.

Although the fatigue strength of the conventionally manufactured AISI 4140 steel and its post heat treatments have been investigated a lot [112, 113, 114], there is no relevant study on the fatigue behaviour and mechanisms of the AISI 4140 steel manufactured by PBF-LB. Hence, it is meaningful to investigate the fatigue behaviour of the PBF-LB AISI 4140 samples and different potential methods including heat treatment and mechanical treatment to improve the fatigue strength in this thesis.

Additionally, one of the crucial tasks in understanding fatigue behaviours of components manufactured by PBF-LB is to develop reliable models for predicting the fatigue life of metal workpieces. In this section, several practical models are presented.

Linear cumulative damage model

Miner's rule [115] is a widely used empirical method for predicting the cumulative damage of a metal component subjected to multiple load cycles. The rule assumes that the damage caused by each cycle is additive and that the component will fail when the cumulative damage exceeds a certain threshold, which can be expressed as follows,

$$\sum_{i=1}^{n} \frac{N_i}{N_{fi}} = \frac{1}{N_f} \sum_{i=1}^{n} N_i \leq 1 \tag{2.2}$$

where N_i is the number of cycles at a given stress level, and N_{fi} is the corresponding fatigue life at that stress level.

While Miner's Rule is a simple and widely used model, it does have some limitations. For example, it assumes that the damage caused by each cycle is additive, which may not be true for all materials or loading conditions. It also assumes that the component fails when the cumulative damage ratio reaches one, which may not be an accurate representation of the actual failure behavior. As a result, Miner's Rule is often used as a conservative estimate of the fatigue life of a component, rather than an exact prediction.

Fatigue crack growth

The fatigue life of workpiece depends on the numbers of cycles for crack propogation. Based on the assumption that the crack growth rate is proportional to the range of the stress intensity factor and the number of cycles, As proposed by Paris et al. [116], the expression of cracking growth rate is displayed as follows,

$$\frac{da}{dN} = C(\Delta K)^m \tag{2.3}$$

where da/dN is the crack growth rate, ΔK is the stress intensity factor range, and C and m are material constants. Hence the number of cycles during the crack propogation can be expressed as follows,

$$N_f = \int_{a_0}^{a_f} \frac{da}{C(\Delta K)^m} \tag{2.4}$$

where a_0 is the inital crack length, and a_f is the final length before fracture. Moreover, the classic features of the fatigue strength of workpiece in presence of defects can be referred to the Kitagawa-Takahashi diagram [117], as shown in Fig. 2.17.

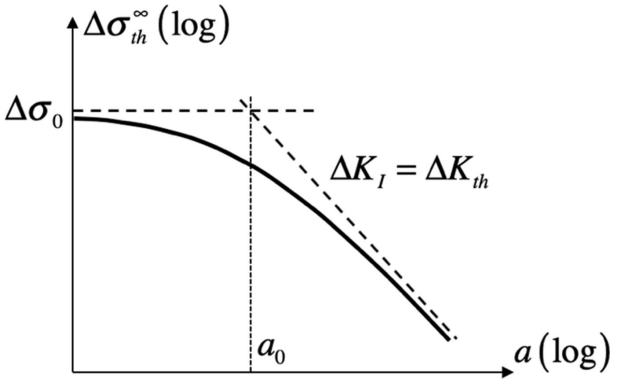

Figure 2.17: Schematic of the typical Kitagawa-Takahashi diagram [117].

However, the ΔK in Eq. 2.4 is only valid for long defect/crack length > 1000 µm. Regarding cracks propagating from short length (10 ≥ a ≥ 1000 µm) to long length, El-Haddad model [118] provides an accpetable solution to address it, which can be expressed as follows,

$$\Delta K_{th,sc} = \Delta K_{th,lc} \times \sqrt{\frac{\sqrt{area}}{\sqrt{area} + \sqrt{area_0}}} \tag{2.5}$$

$$\sqrt{area_0} = \frac{1}{\pi} \cdot \left(\frac{\Delta K_{th,lc}}{Y \cdot \Delta\sigma_e}\right)^2 \tag{2.6}$$

where $K_{th,sc}$ is the threshold SIF range for short cracks, $K_{th,lc}$ is the threshold SIF range for long cracks, $\sqrt{area}$ is the method of obtaining the size parameter of irregular defects as proposed by Murakami [119] and shown in Fig. 2.18, while $\sqrt{area_0}$ is a characteristic material parameter. However, the influences of residual stress on the fatigue strength are not mentioned. The extra high residual stress in workpieces produced by PBF-LB cannot

be ignored, and the influences of residual stress on fatigue behaviour will be investigated thoroughly in this thesis.

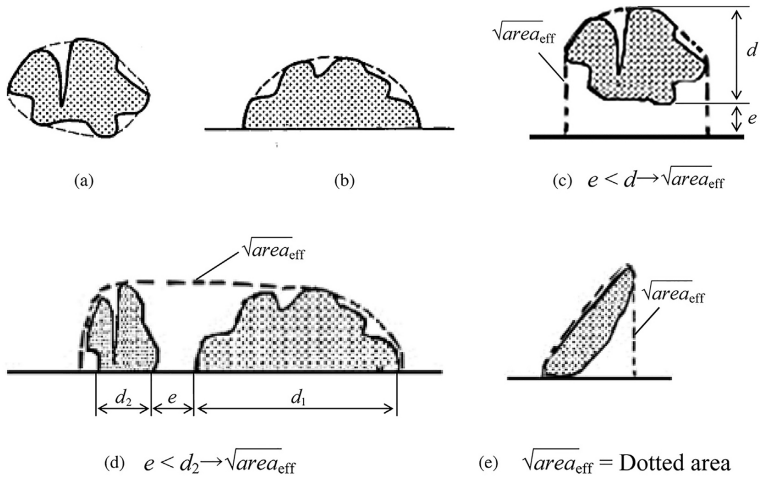

Figure 2.18: Estimation method for irregularly shaped defects in the vicinity of surface [119]. Reproduced with permission from Elsevier.

Overall, the fatigue behaviour of metallic materials manufactured by PBF-LB is affected by not only defects and surface roughness due to inappropriate processing parameters but also by the material properties. That means the fatigue behaviour and killer defects of different metallic materials fabricated by PBF-LB could be different. However, there are not sufficient investigations on the fatigue behaviour of carbon-bearing martensitic steels manufactured by PBF-LB, especially no investigations on the fatigue behaviour of AISI 4140 steel manufactured by PBF-LB.

3. Experimental design and characterization

3.1 Materials

The AISI 4140 powder used in the investigation was produced by gas atomization by Höganäs. The chemical composition of the powder is shown in Table 3.1. The particle size distribution has a d_{10} of 14 µm and a d_{90} of 28.4 µm. The powder morphology and powder size distribution also can be seen in Fig. 3.1. Powders were dried in a vacuum dryer at 100 °C for about 4 hours to avoid possible moisture.

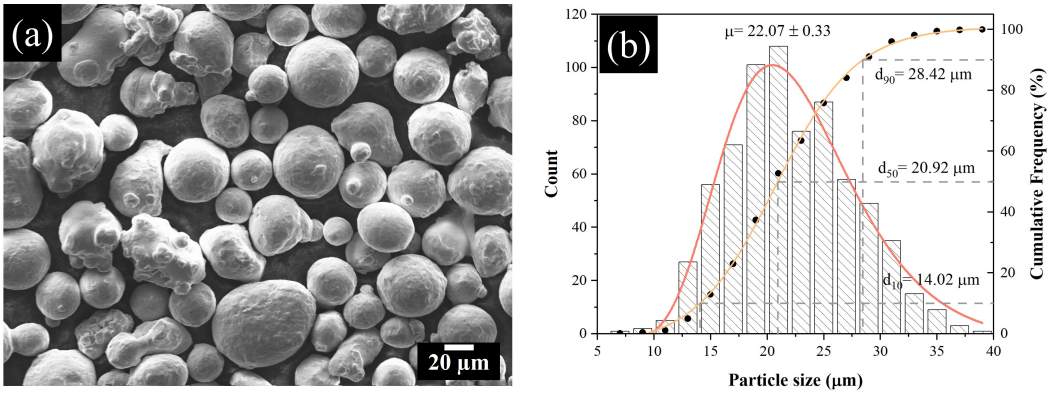

Figure 3.1: (a) The morphology of AISI 4140 powder used in PBF-LB, and (b) the particle size distribution.

Table 3.1: Chemical composition of the powder particles in wt %.

Element	C	Cr	Mo	Mn	Si	P	S	Fe
Tested	0.39	1.0	0.2	0.9	0.4	0.026	0.006	Bal.
Standard	0.38-0.45	0.9-1.2	0.15-0.3	0.6-0.9	0.1-0.4	∼0.025	∼0.035	Bal.

The standard is according to DIN EN ISO 683-2.

3.2 Experimental design

3.2.1 Powder Bed Fusion-Laser Beam procedures

As-built specimens were fabricated in an ORLAS CREATOR powder bed fusion machine (Fig. 3.2a), equipped with a 250 W Yb:YAG fibre laser source with a focus diameter of 40 µm and wavelength of 1070 nm.

Regarding substrate preheating, specimens were produced using a LiM-X260A machine (Fig. 3.2b) with the same parameters and a preheating temperature of 200 °C. The manufacturing process was carried out in an Argon gas environment (oxygen content in the chamber was maintained at approximately 0.01 % to avoid possible oxidation). The detailed parameters for PBF-LB are also listed in Table 3.2.

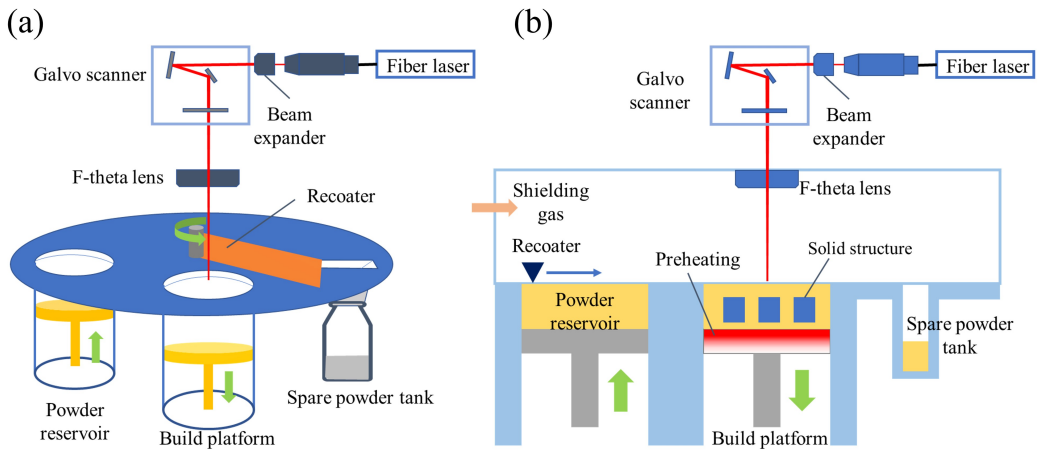

Figure 3.2: The schematic illustration of (a) ORLAS CREATOR and (b) LiM-X260A.

Table 3.2: Processing parameters for PBF-LB.

Parameters	Value
Beam diameter	40 µm
Wavelength	1070 nm
Substrate preheating	200 °C
Laser power	175-250 W
Laser velocity	300-1500 mm/s
Hatching distance	40-80 µm
Layer thickness	30 µm
Rotation angle	67°
Scanning strategy	uni-directional scan
Oxygen content	0.01 %
Shielding gas	Argon

3.2.2 Geometries and processing parameters

The geometry sizes of the specimen for parameters optimization is ϕ 10×10 mm. The Laser power ranges from 175 W to 250 W, laser velocity varies from 300 mm/s to 1500 mm/s, the layer thickness is 30 µm, and the hatching distance ranges from 40 to 80 µm. The rotation angle between successive layers is 67° and the scanning strategy is uni-directional scan. Three specimens for each processing parameter set were produced to obtain the average relative density and crack density values.

3.2.3 Heat treatment

One advantage of AISI 4140 steel is that the mechanical properties can be adjusted via heat treatment. The heat treatment for PBF-LB workpieces can be divided into in-operando/intrinsic and post-heat treatment. In-operando heat treatment is to heat the building plate up to 200 °C in order to reduce the temperature gradient during the manufacturing process. Methods used for post heat treatment are hot isostatic pressing (HIP), and quenching and tempering (Q&T).

Specimens for HIP treatment were kept at 1150 °C and 110 MPa for 2 hours, and the aim of implenting HIP is to reduce possible defects in specimens. The standard procedures for quenching is to heat specimens at 850 °C, then to quench them in oil to room temperature. Regarding tempering, the tempering temperature was calculated according to Hollomon-Jaffee method to obtain a comparable hardness with as-build PBF-LB specimens. For AISI 4140, there is a linear relationship between the hardness and Hollomon-Jaffee parameter (P_{HJ}) according to a experimental equation [120],

$$HV = 1034.12 - 0.03562 P_{HJ} \tag{3.1}$$

The relationship between P_{HJ} and temperature can be expressed as follows,

$$P_{HJ} = T(C + log_{10}(t)) \tag{3.2}$$

where T is the temperature in K, C is the material constant and C=18.864 for AISI 4140, and t is time in second. Therefore, the tempering temperature can be calculated when the goal hardness and heat treatment time are known.

3.2.4 Laser remelting

The processing parameters for the first melting were chosen based on the parameter optimization results and are listed as follows, the laser power is 250 W, the laser scanning speed is 1300 mm/s, the hatching distance is 60 µm, and the powder layer thickness is 30 µm. The laser power and scanning speed for remelting range from 50 % to 100 % of the first melting values (P= 125, 150, 175, 200, 225, 250 W and v= 650, 780, 910, 1040, 1170, 1300 mm/s). The scanning paths and rotation angle between layers of one and two remelting steps (R1 and R2) are the same as the first melting (67°), as shown in Fig. 3.3.

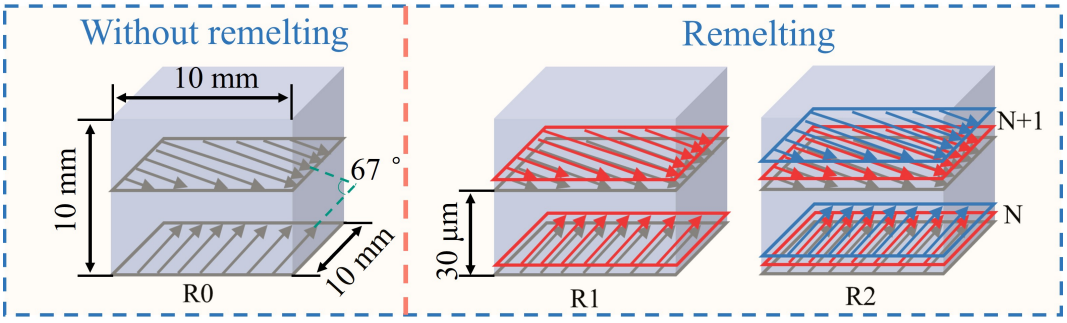

Figure 3.3: The schematic of laser remelting and remelting steps on specimens. R0 represents no remelting, and R1 represents remelting once, and R2 represents remelting twice [121].

3.2.5 Machining and deep rolling

In rough machining, the cutting depth a_p is 0.5 mm, the feed rate f is 0.2 mm/min, and the cutting speed v_c is 80 m/min. In precision machining, the cutting depth a_p is 0.2 mm, the feed rate f is 0.06 mm/min, and the cutting speed v_c is 100 m/min.

For some fatigue test specimens that require surface deep rolling after machining, the parameters for the deep rolling process are listed in Table 3.3.

Table 3.3: Processing parameters for the deep rolling process.

Parameters	Value
Hydraulic pressures	150 bar
Feed rate	0.04 mm
Spindle speed	250 r/min
Diameter of the tool	6 mm

3.2.6 Relative density and crack density measurement

The relative density of specimens was measured according to Archimedes' principle using a precision balance ME503TE, and distilled water was used as medium for the measurement. Relative density can be expressed as

$$RD = \frac{\rho_{measured}}{\rho_{ref.}} \tag{3.3}$$

and $\rho_{ref.} = 7.83$ g/cm^3. The crack density was measured by the image threshold technique via ImageJ software by measuring the length of each crack in metallographic sections (seen Fig. 3.4). Then, the total lengths of cracks ($L_{cracks,tot}$) were divided by the total areas measured in images (S) to get the crack density (mm/mm^2), and it can be expressed as follows,

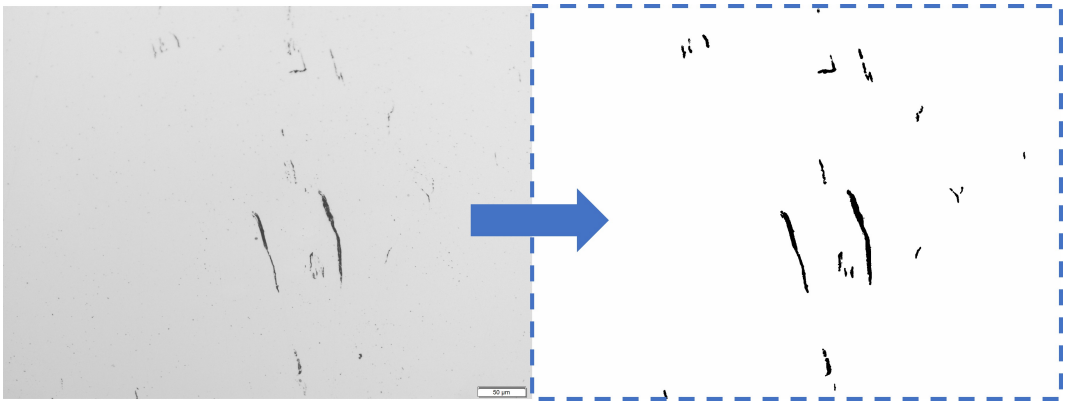

Figure 3.4: Microcracks extracted from the metallographic figure.

$$CD = \frac{L_{cracks,tot}}{S} \tag{3.4}$$

3.2.7 Tensile test

For uniaxial tensile tests, specimens were built in the size of ϕ 10 $\times$ 60 mm in vertical (V) and transverse (T) orientations. Then dog-bone shaped samples were machined with a gauge diameter of 5 mm and a gauge length of 25 mm according to DIN 50125, as shown in Fig. 3.5.

The tensile tests were conducted using a Zwick/Roell 1484 200 KN universal testing machine (equipped with an extensometer) with a strain rate of 0.001 /s at room temperature, and at least 5 specimens for each parameter group were tested.

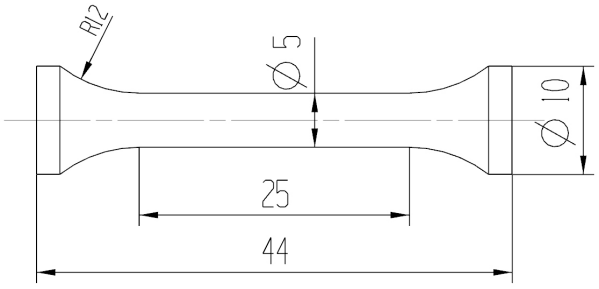

Figure 3.5: Geometry for tensile tests.

3.2.8 Charpy impact test

The impact roughness of the material under impact loading can be measured by the standardized Charpy impact test, which involves striking a notched specimen with a pendulum and measuring the amount of energy absorbed by the specimen, as shown in Fig. 3.6.

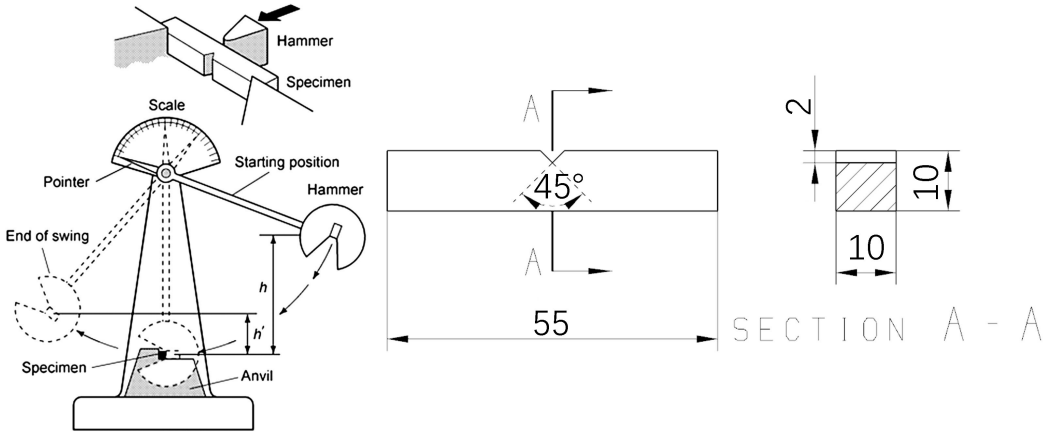

Figure 3.6: The schematic of Charpy impact test [122] and the standard dimensions of specimens after machining.

Samples for Charpy impact tests were manufactured via PBF-LB in dimensions of $15\times15\times60$ mm and machined to $10\times10\times55$ mm, following the standard described in ASTM E23-18. The building direction of specimens during the manufacturing process was parallel to the building platform. The Charpy impact testing was conducted using a Frank Pendulum at room temperature. Five specimens for each parameter group were tested to obtain the average impact energy value.

3.2.9 High cycle fatigue test

Specimens fabricated by PBF-LB initially featured a gauge section 6 mm in diameter and 15 mm in length, with an overall length of 78 mm; subsequent machining reduced the

gauge diameter to 5 mm and the overall length to 75 mm, while maintaining the 15 mm gauge length in accordance with DIN 50113, as shown in Fig. 3.7.

High cycle fatigue tests for PBF-LB specimens were conducted on a 100 Nm rotating bending machine under moment–control (Fig. 3.8), which was operated at a constant frequency of 50 Hz, and the nominal load ratio R = -1. The fatigue limit of specimens was determined firstly at an initial stress amplitude of σ_a= 300 MPa and then decreased or increased by 25 MPa each step according to the staircase method [123]. 10^7 cycles were set as the fatigue strength limit, and the specimen was declared as run out when the number of cycles exceeded 10^7, otherwise specimens were seen as failed when surviving less than 10^7 cycles. The final S-N curves were drawn according to the horizon method with 2-3 specimens per horizon. At least 15 specimens for each parameter group were tested to get credible experimental data.

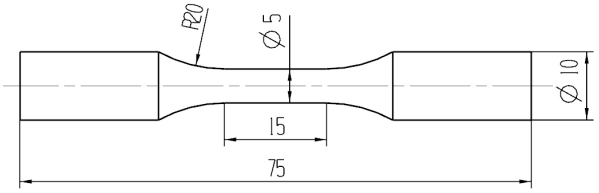

Figure 3.7: Geometry for rotation bending fatigue testing.

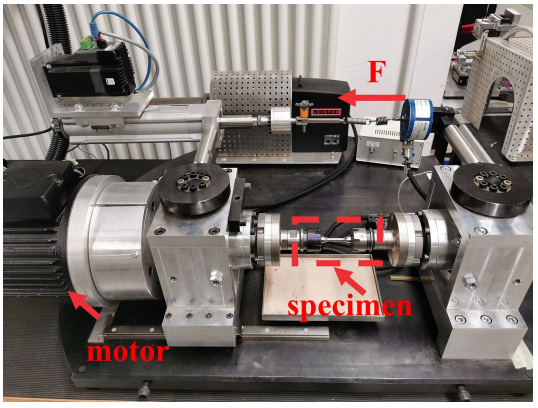

Figure 3.8: The equipment used for rotation bending fatigue testing.

3.2.10 Residual stress

X-ray diffraction (XRD) is a widely used technique for residual stress measurement in materials, which exploits the fact that stressed and unstressed materials have slightly different crystal lattice spacing. When X-rays are directed at a crystalline material, they are diffracted by the crystal lattice planes at specific angles, producing a unique diffraction pattern that reflects the crystal structure. Stress changes the crystal lattice spacing, which affects the diffraction angles and intensities. By analyzing the diffraction pattern, including the angles and intensities of the scattered X-rays, it is possible to determine the crystal lattice spacing and residual stress in the material.

Residual stress in PBF-LB specimens was determined using the $\sin^2\Psi$ method by CrKα radiation of the {211} lattice plane of α-Fe in a Ψ-diffractometer. The measurements along the built direction of specimens were carried out in a range of $-45° \leq \Psi \leq 45°$. The depth profiles for specimens were determined via electropolishing in steps of about 30 µm.

The $\sin^2\Psi$ method can be written as follows,

$$d_\Psi = \frac{1+\nu}{E} d_0 \sigma_\phi sin^2\Psi - \frac{\nu}{E}(\sigma_{11} + \sigma_{22}) d_0 + d_0 \tag{3.5}$$

where d_0 is the unstressed plane spacing, d_Ψ is the stressed inter-planar spacing, E and ν are Young's modulus and Poisson's ratio for the {211} reflection, respectively. As the variation of the plane spacing with $\sin^2\Psi$ is linear, the surface stress σ_ϕ can be determined from the slope of the d_Ψ and $\sin^2\Psi$ data.

3.2.11 Microhardness

To measure Vickers microhardness, the material surface is indented with a pyramidal diamond indenter which has an included angle of 136° between its opposite faces. The diagonal length of the resulting indentation is measured after a specified holding time, and the hardness value is calculated according to the formula as follows,

$$HV = \frac{1.854F}{d^2} \tag{3.6}$$

where F is the testing load (N), and d is the diagonal length of the indentation (mm).

Microhardness of PBF-LB specimens was measured by using a Qness Q10A Vickers digital microhardness tester with a load of 100 g and a dwell time of 10 s. The microhardness was measured at intervals of 0.2 mm, starting from the top layer down to a depth of 8 mm. Three points for each interval distance were tested to determine the average microhardness.

3.2.12 Surface roughness measurement

In the surface roughness measurement, Ra and Rz are parameters that commonly used to characterize the surface roughness of workpieces. Ra is the arithmetic mean of surface profile and represents the average deviation of surface height from the mean line. Specifically, Ra is the average of the absolute values of all deviations when the surface height is shifted up and down to touch the mean line within a certain length, and it can be expressed as follows,

$$Ra = \frac{1}{L} \int \mid y(x) - y_m \mid dx \tag{3.7}$$

where y(x) is the surface height curve, y_m is the mean value, and L is the length of the measurement.

Rz is the maximum peak-to-valley height of the surface profile within a given length, indicating the vertical distance between the highest peak and the lowest valley. It is calculated as the sum of the vertical distances between the five highest peaks and the five

lowest valleys within the given length,

$$Rz = \mid Ry_1 \mid + \mid Ry_2 \mid + \cdots + \mid Ry_n \mid \tag{3.8}$$

where Ry_n is the distance between the n highest peak and the lowest valley.

The surface roughness of PBF-LB specimens was measured on both, up-skin and lateral surfaces by using a Nanofocus µsurf confocal microscope. Three measurements for each surface and three specimens per parameter set were investigated.

3.2.13 Characterization of microstructure and defects

Specimens for microstructural characterizations were cut, embedded, mechanically ground, polished, and finally etched by a solution of 98 % alcohol (analytical reagent) and 2 % HNO_3 (analytical reagent). The microstructure characteristics of polished specimens and fracture surfaces of specimens after mechanical tests were analyzed by a Zeiss Leo50 scanning electron microscope (SEM) at an accelerating voltage of 20 kV and the Leitz Aristomet optical microscope.

In order to further analyze morphology of defects in specimens manufactured by PBF-LB, the three dimensional microstructure information of specimens was obtained by using a YXLON Precision X-ray microtomography scanner at an acceleration voltage of 185 kV and a target current of 110 µA. A total of 2070 projections were measured on a Perkin Elmer XRD1620 AN flat panel detector with a pixel pitch of 200 µm and a total field of view of 2048 × 2048 pixels. The voxel size for the measurement is 2.7×2.7×2.7 µm. Reconstruction of the 2D slices into 3D image stacks were carried out in VGStudio MAX 3.4 software using the FDK algorithm. The gauge length of 15 mm of fatigue specimens was scanned to investigate the overall distribution of pores in specimens.

4. Processing parameters optimization

In PBF-LB process, the vital processing parameters are laser power P (W), laser scanning velocity v (mm/s), hatching distance h (µm) and powder layer thickness t (µm). The defects generated during PBF-LB are directly relevant to these processing parameters, which further affects the mechanical properties, hence it is essential to optimize the processing parameters based on the currently used manufacturing machine.

In this chapter, the investigation of laser power and scanning velocity begins with the examination of single tracks to analyze melt pool dimensions, including both width and depth. Subsequently, the impacts of processing parameters on the relative density and crack density were investigated in the bulk samples, and the optimized parameters for AISI 4140 were finally obtained. Additionally, the influences of various building orientations and layer thicknesses on surface roughness were also studied to obtain a relatively good surface quality. Finally, the processing parameters for laser remelting were investigated and optimized, and the influences of laser remelting on relative density and crack density were also discussed in this chapter.

4.1 Single tracks

4.1.1 Width

The morphology of single tracks manufactured with different scanning speeds from 300 to 1500 mm/s, while maintaining a constant laser power of 250 W, is shown in Fig. 4.1. It can be found that all tracks (Fig. 4.1 (a-f)) are decorated with partially melted powder on both lateral and even the up-facing surfaces, suggesting it is difficult to avoid the partially melted powder on tracks just by optimizing the laser processing parameters.

The track remains continuous with a width of about 234 µm at a scanning speed of 300 mm/s (Fig. 4.1a). However, a necking effect becomes evident in the track as the scanning speed surpasses 700 mm/s (Fig. 4.1c). This necking effect could result in LoF defects during the melting of multiple tracks and layers, demonstrating that low scanning speed, lower than 500 mm/s (Fig. 4.1b) in this investigation, can be beneficial to reduce the necking effect in single tracks.

The width also shows a decreasing trend with increasing scanning speed, and it drops by about 64 % when v= 1500 mm/s (Fig. 4.1f) compared to that of v= 300 mm/s. As shown in Fig. 4.2, the shapes of the tracks cannot be formed well, with serious necking effect and even discontinuous sections, while scanning with a lower laser power of less than 250 W (Fig. 4.2 (a-b)). However, the width of the track is not changed much with different laser power (v= 1300 mm/s, P= 200, 225 and 250 W). The dominant defects are the discontinuous tracks due to balling and necking effects when decreasing the laser power from 250 W to 200 W, indicating improving the laser power is vital to reduce the balling and necking effects in producing single tracks of AISI 4140 steel.

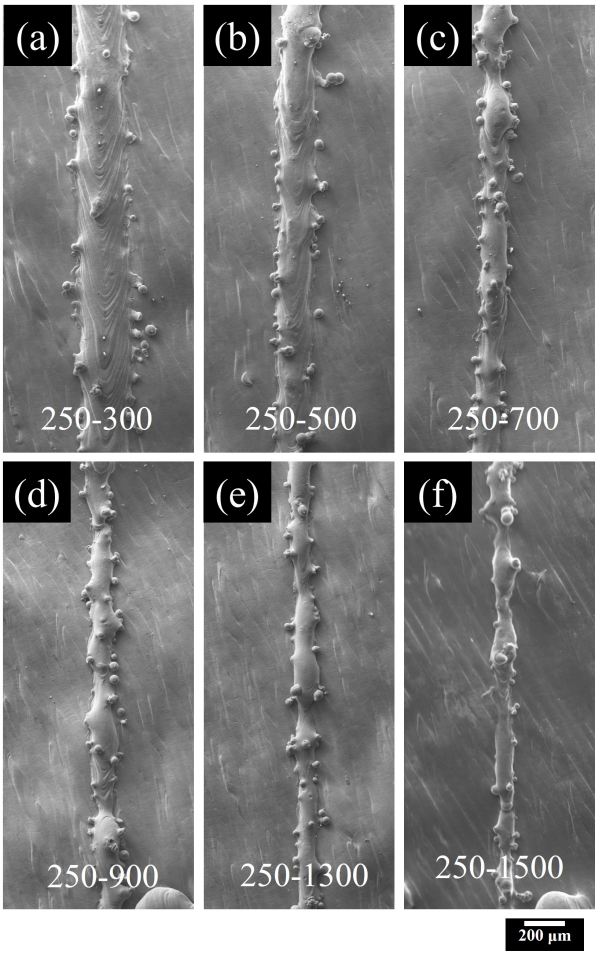

Figure 4.1: Single tracks scanned with various laser velocity from 300 mm/s to 1500 mm/s, P= 250 W and t= 30 µm.

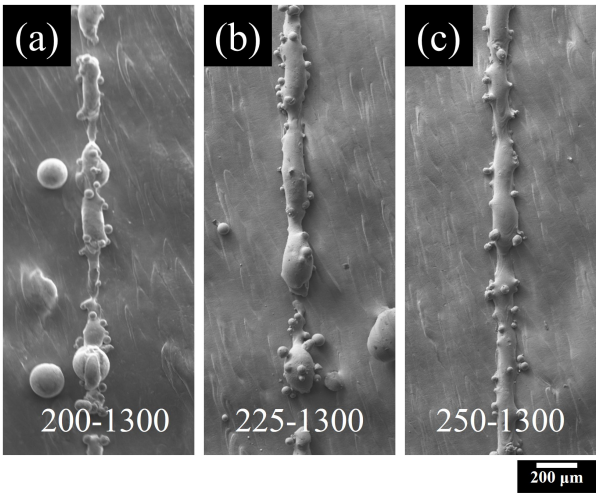

Figure 4.2: Single tracks scanned with various laser power from 200 W to 250 W, showing balling and necking defects along tracks at a scanning speed of v= 1300 mm/s and a layer thickness of t= 30 µm.

4.1.2 Depth

The cross-section of single tracks is prepared, as shown in Fig. 4.3, to study the influence of processing parameters on the penetration depth. It can be found that the penetration depth is obviously reduced with increasing the scanning speed from 300 mm/s to 1500 mm/s. Moreover, the height of the tracks which is the part above the substrate, also tends to increase while increasing the scanning speed.

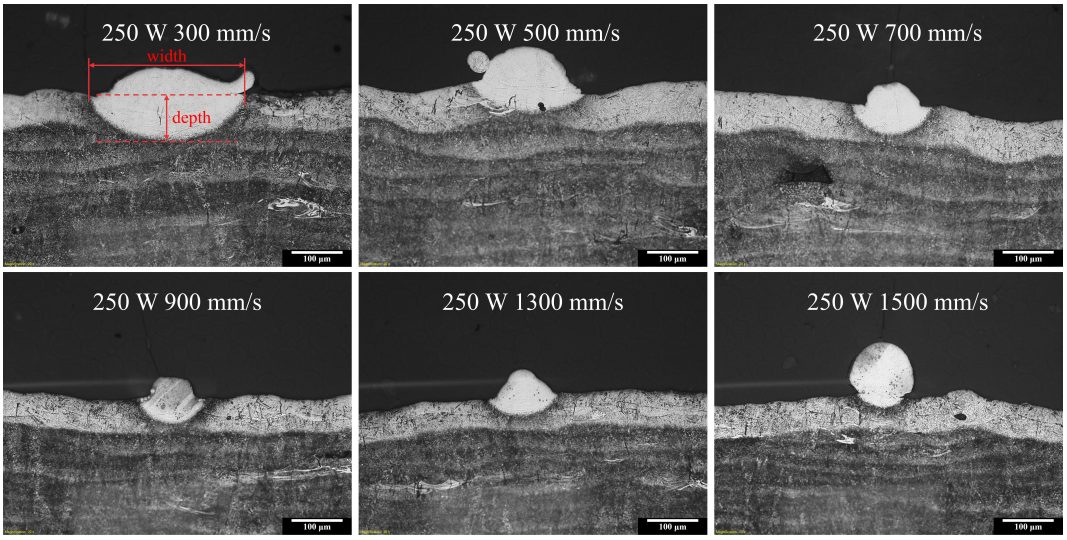

Figure 4.3: The cross-section of single tracks scanned with various laser velocity v from 300 mm/s to 1500 mm/s at a laser power of P= 250 W and a layer thickness of t= 30 µm.

The reduction of the penetration depth and an increase in height when increasing the scanning speed indicate the balling effect is deteriorated with increasing the scanning speed. However, it should be noted that some cross-section probably located in the vicinity of defects or necking sections; hence, three tracks of each parameter group are measured to get relatively stable geometry sizes.

4.1.3 Discussion

4.1.3.1 Influences of processing parameters on the width

For single tracks, the linear energy density (LED) is generally used to consider the influence of processing parameters on the melting quality of single tracks. The LED can be expressed as follows,

$$LED = \frac{P}{v} \tag{4.1}$$

The LED is mainly affected by two parameters, including laser power and scanning speed. As the variation of P just ranges from 200 W to 250 W, but the scanning velocity v varies from 300 to 1500 mm/s, which means the effect of the scanning speed on the LED weighs heavier than the power in this investigation (Fig. 4.4a and b).

It can be found in Fig. 4.4c that the width of the track increases from about 83.5 to 234 µm with increasing the LED from 0.17 to 0.83 J/mm, which again proves that the width

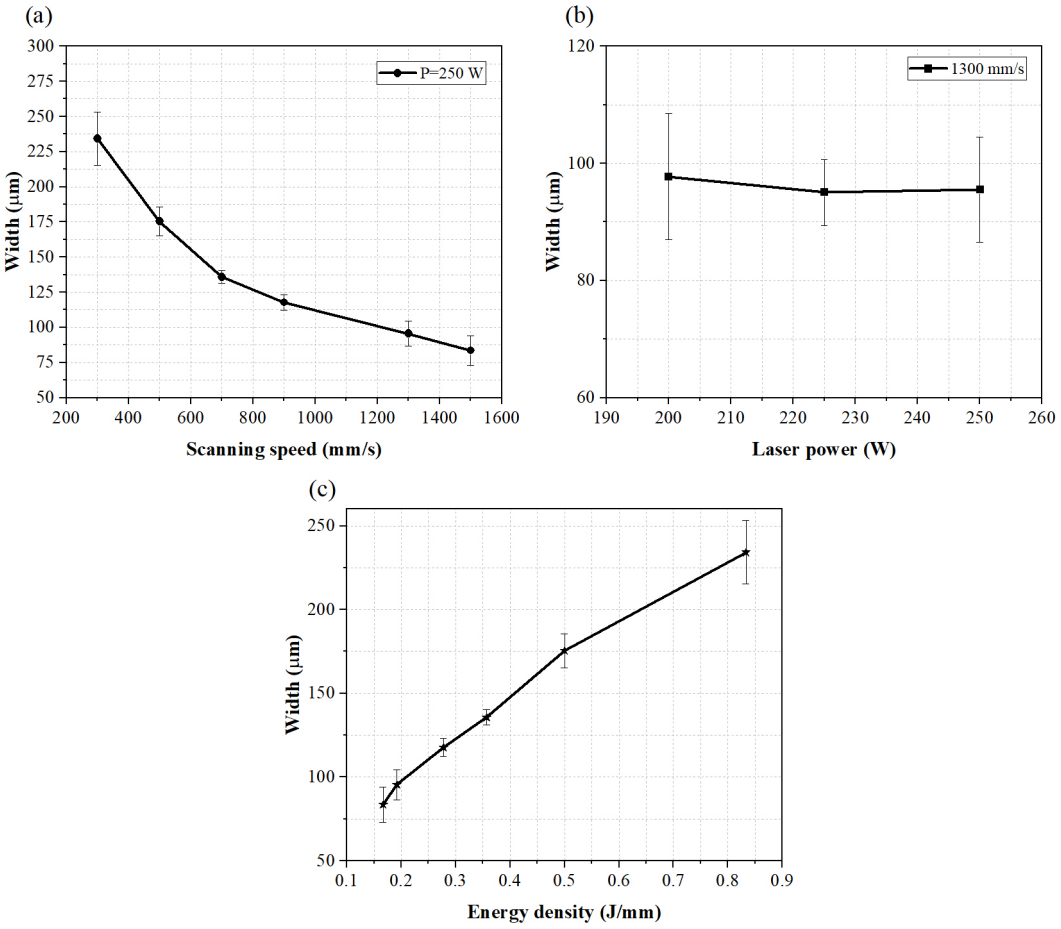

Figure 4.4: Influences of processing parameters (a) scanning speed, (b) laser power and (c) linear energy density on the width of single-tracks.

of single tracks is dominated by the laser scanning speed, namely, the width reduces with increasing the scanning speed.

4.1.3.2 Influences of processing parameters on the depth

The influences of laser scanning speed and LED on the penetration depth is similar to the width. As depicted in Fig. 4.5, the depth of the melt pool is reduced from about 81 µm to 28 µm, about a 65 % reduction, while increasing the scanning speed from 300 to 1500 mm/s (Fig. 4.5a), and the depth is inversely increased with increasing the LED (Fig. 4.5c). Moreover, the penetration depth is also obviously influenced by the laser power, and the depth is increased from about 19 µm to 38 µm, and the improvement is 100 % with an increase in the laser power from 200 W to 250 W (Fig. 4.5b), which shows a positive linear relationship between the penetration depth and laser power.

Additionally, it should be noted that some microcracks vertical to the scanning direction are observed on the single tracks manufactured with low velocity (300-500 mm/s), as shown in Fig. 4.6. It means microcracks exist and are prone to occur at low scanning speeds during the melting of single tracks. This kind of microcracks could be ascribed to high thermal residual stress in single tracks scanned with low velocity [56]. However, microcracks in single tracks can be healed in the following melting of mutiple tracks and layers.

In a short summary, the width of the tracks is mainly dominated by the laser scanning speed, and the penetration depth of the track is affected by both laser power and laser scanning speed. Therefore, the laser power should be kept at a high value, for example, 250 W, to ensure a high LED when a fast-scanning speed is implemented, to get an acceptable penetration depth between layers.

4.2 Multiple tracks and layers

4.2.1 Relative density

The morphology of defects in bulk specimens produced within the prospective processing window are shown in Fig. 4.7, and the respective relative density distribution of bulk specimens measured by Archimedes' method is shown in Fig. 4.8. It can be obviously found that most of the low relative density (RD) (92 % - 93 %) are obtained when laser power is 175 W, or the laser scanning speed is 1500 mm/s.

It was also found that the RD increases prominently while increasing laser power from 175 W to 250 W. For example, the RD increases from about 93 % to over 98 % when laser power increases from 175 W to 250 W manufactured with the same laser scanning speed (1300 mm/s) and the hatching distance (60 µm). However, the influence of laser scanning speed on RD does not vary much especially when laser power is 250 W (Fig. 4.8 (a-c)). Fig. 4.8d demonstrates that the changes in the hatching distance (40-80 µm) do not influence much the RD in comparison to the laser power.

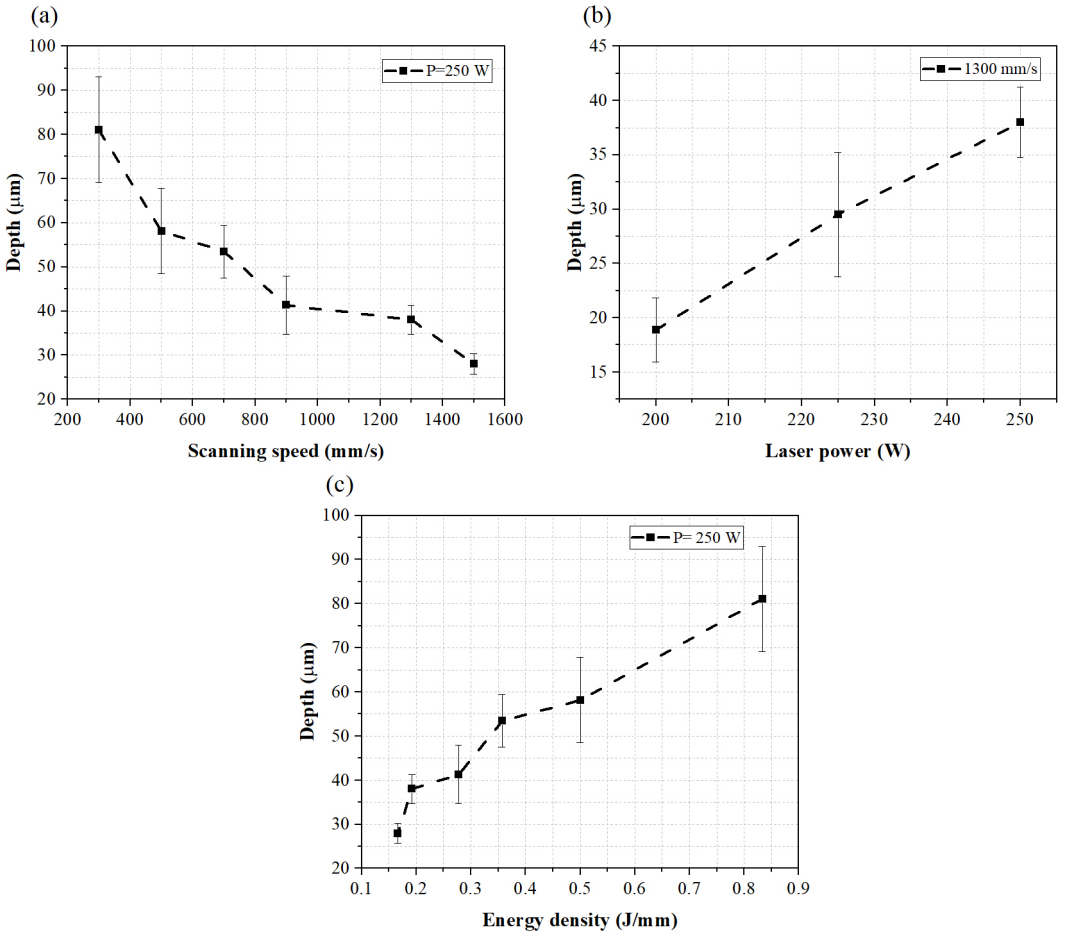

Figure 4.5: Influences of processing parameters (a) scanning speed, (b) laser power and (c) linear energy density on the depth of single-track.

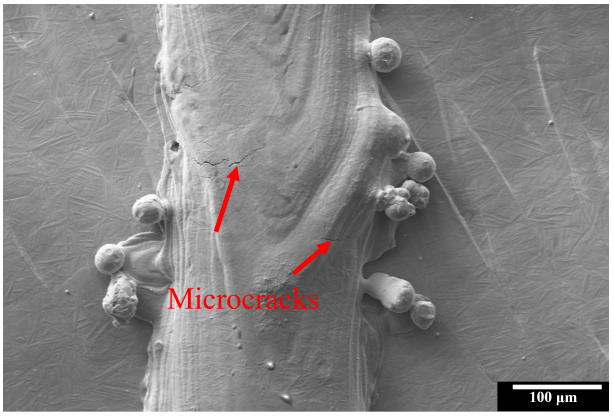

Figure 4.6: The SEM image shows microcracks perpendicular to the laser scanning direction. P= 250 W, v= 300 mm/s, h= 60 µm and layer thickness t= 30 µm.

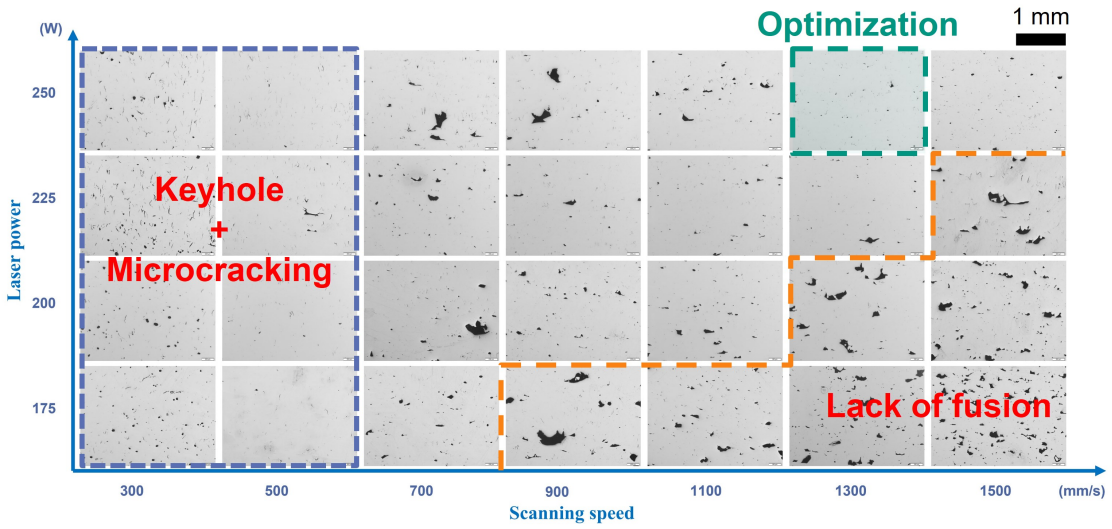

Figure 4.7: The processing window for AISI 4140 steel manufactured by PBF-LB without preheating [124]. Laser power ranges from 175 W to 250 W, and laser scanning speed varies from 300 mm/s to 1500 mm/s, h= 60 µm and t= 30 µm.

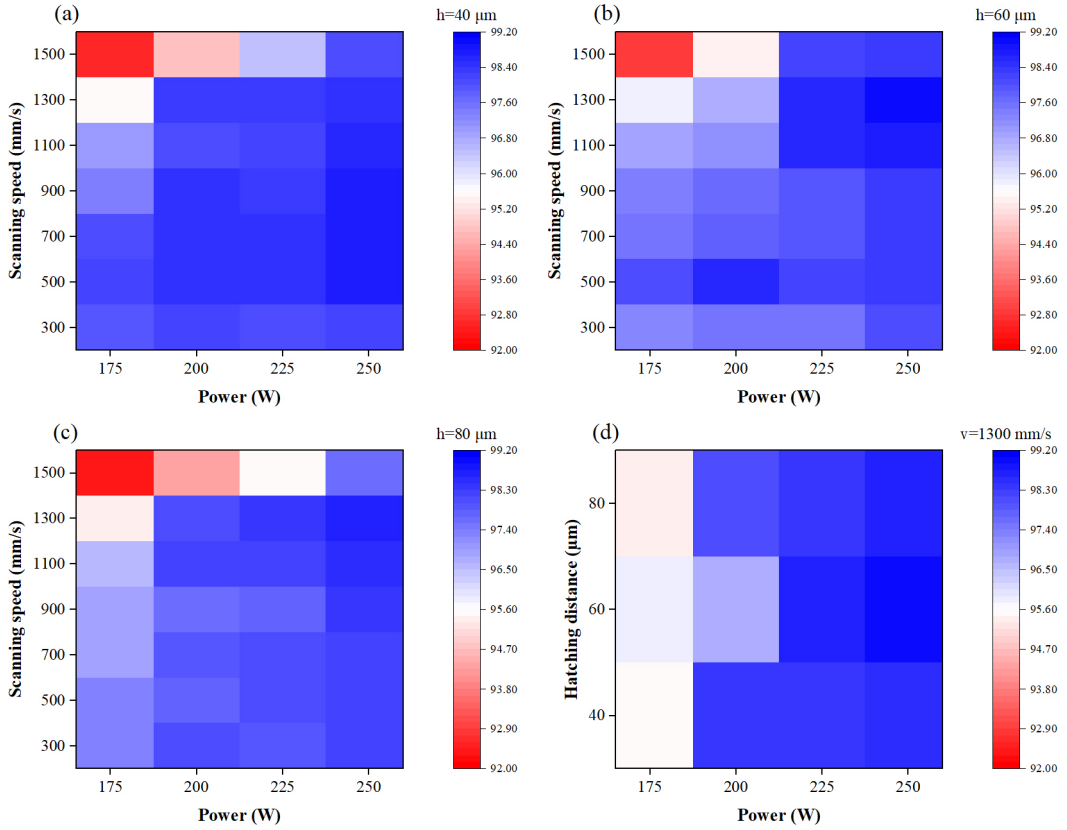

Figure 4.8: Relative density of specimens produced with different processing parameters (without preheating, t= 30 µm, the reference density is 7.83 g/cm^3): (a) h= 40 µm, (b) h= 60 µm, (c) h= 80 µm, and (d) influence of hatching distance on relative density, v= 1300 mm/s [124].

4.2.2 Crack density

Apart from the RD, cracking is another category of defects critical in the additive manufacturing of AISI 4140 steel, which normally originates from a steep temperature gradient plus phase transformation. It can be found in Fig. 4.9 that the crack density sharply drops from 3 to 0.23 mm/mm^2 while increasing the laser scanning speed from 300 mm/s to 1500 mm/s (with the same laser power, P=250 W), and the cracking distribution in specimens can also be seen in Fig. 4.7.

Moreover, the crack density is as low as (0.01-0.76 mm/mm^2) within all ranges of the laser power when the laser scanning speed is beyond 900 mm/s, suggesting a fast laser scanning speed combined with either low or high laser power is beneficial to reduce the crack density in as-built specimens without base preheating.

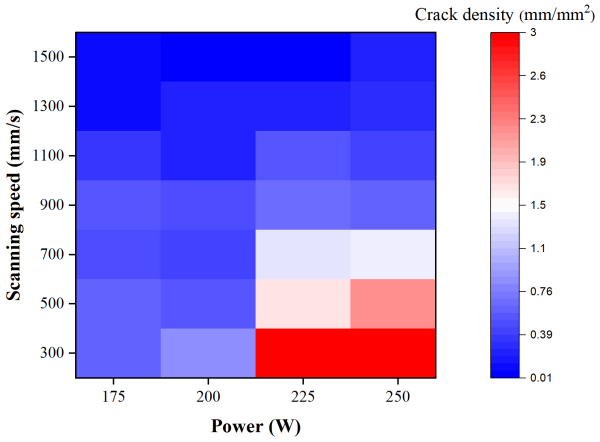

Figure 4.9: The heat map shows the influences of laser power and scanning speed on the microcrack density in AISI 4140 steel (without prehating), h=60 µm and t=30 µm [124].

It is also interesting to note that the crack density of specimens manufactured at a laser power of 200 W and the scanning speed ranges from 500 to 1100 mm/s is higher than that of specimens produced with 175 W, as shown in Fig. 4.9. The possible reason could be that the dominant defects in 175 W specimens are LoF pores, and the amount of LoF defects is more than that in 200 W specimens, in which cracking is prone to initiate in the tips of irregular LoF defects due to stress concentration.

Although the RD of the 200 W/500 mm/s specimen is 98.57 %, and the RD value is close to the RD of the 250 W/1300 mm/s specimen (99 %), the crack density of the 200 W/500 mm/s specimen is about 2 times of the latter. Therefore, it is better to choose a processing window with fast scanning speed to reduce crack density compared to processing window with low scanning speed.

When specimens are manufactured with the 200 °C base preheating with the same processing parameters (250 W/1300 mm/s, h=60 µm), the RD is further improved from 99 % to 99.3 %, and the crack density is less than 0.01 mm/mm^2, which reduces by about 95 % compared to that without base preheating, as shown in Fig. 4.10. Although the RD

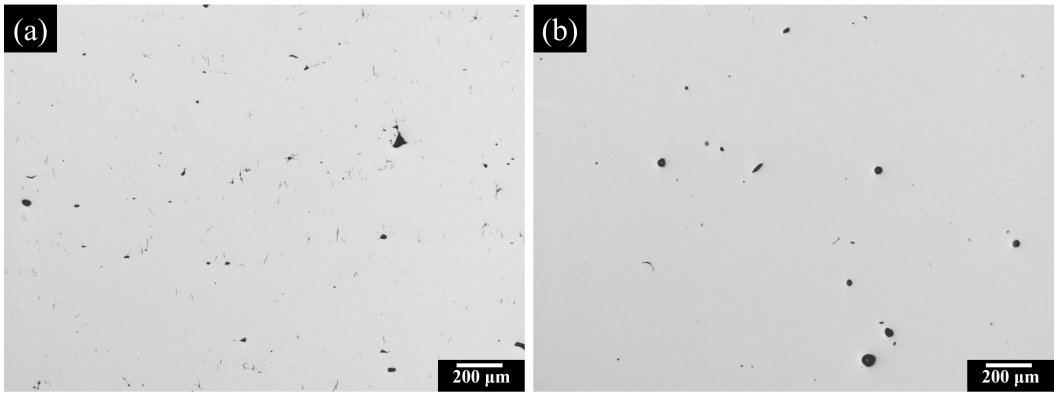

Figure 4.10: (a) As-built specimen and (b) specimen manufactured with 200 °C base preheating. P=250 W, v=1300 mm/s, h=60 µm and t=30 µm.

is not improved much with preheating, the prominent reduction in the crack density of specimens with base preheating can be ascribed to the reduction of a temperature gradient to reduce thermal residual stress.

4.2.3 Surface roughness

It can be seen from Fig. 4.11a that the up-facing surface roughness show an increase trend, from 1-2 µm to 4-7 µm, as the scanning speed increases from 300 mm/s to 1500 mm/s, and the increase is greater than 50 %. It also can be found that high laser power is beneficial for the surface roughness reduction especially scanned with high scanning speed (> 1200 mm/s).

However, the roughness of the lateral surface reduces by 10 %-30 % with increasing the scanning speed from 300 mm/s to 1500 mm/s (Fig. 4.11b), indicating a faster laser scanning speed is beneficial for improving the quality of the lateral surface. On the other hand, the roughness decreases with an increase in the laser power from 175 W to 250 W. For example, the mean lateral surface roughness of the specimen produced with 175 W and 1300 mm/s is only about 67 % of that manufactured with 250 W and 1300 mm/s.

The influences of powder layer thickness and manufacturing orientation on both up-facing and lateral surface roughness are also investigated in this section, as shown in Fig. 4.12. It is clearly shown that the upper surface roughness is affected by the building orientation (Fig. 4.13). Specimens manufactured at a 45° orientation have the worst up-facing surface roughness (14.5 µm), compared to those produced in the transverse (0°) and vertical (90°) orientations, and do not significantly show an influence of layer thickness. This result aligns with the investigation conducted by Yan et al. [125] in comparing the effect of different building orientations on the surface roughness of Inconel 625, where they reported that the value of the surface roughness of the PBF-LB 45° sample (R_a= 31.397 µm) was the roughest owing to the balling phenomenon and the stair stepping effect.

Additionally, the lowest up-facing surface roughness, approximately 3 µm, is observed in specimens produced at the 0° and 90° orientations with a layer thickness of 30 µm, which

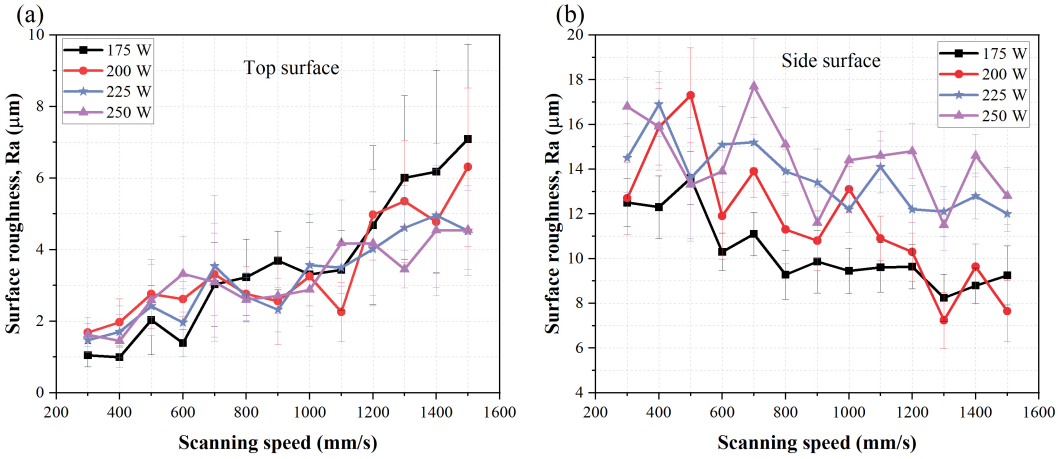

Figure 4.11: Influences of laser scanning speed and laser power on (a) up-facing surface and (b) lateral surface roughness. h= 60 µm and t= 30 µm, and specimens were manufactured without substrate preheating.

is roughly 20.7 % of the roughness found in the specimens manufactured at 45° orientation with the same layer thickness.

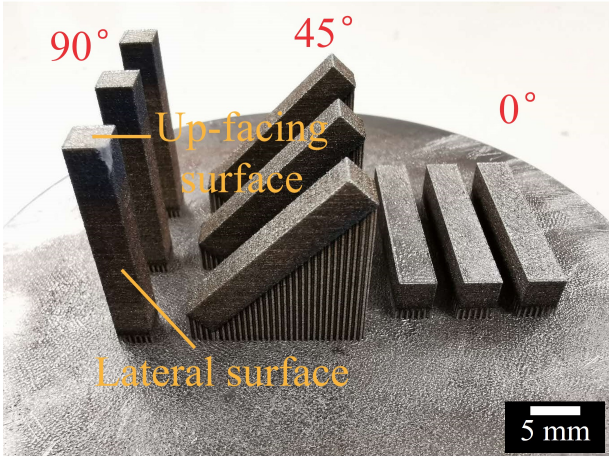

Figure 4.12: The image shows specimens manufactured in different build orientations (without preheating). P= 250 W, v= 1300 mm/s, h= 60 µm and t= 30 µm.

It is worth noting that the roughness of the lateral surface decreases as the layer thickness increases from 30 µm to 50 µm, exhibiting reductions of 21.6 %, 51.8 % and 53.3 % at built orientations of 0°, 45°, and 90°, respectively. By contrast, the up-facing surface roughness of specimens built in 0° and 90° orientations shows an increasing trend as the layer thickness exceeds 30 µm, with a maximum increase of about 105 % and 42 % respectively. Additionally, it is found that the 0° orientation specimen has the highest value of lateral surface roughness (16.2 µm) compared to specimens built in 45° and 90° orientations.

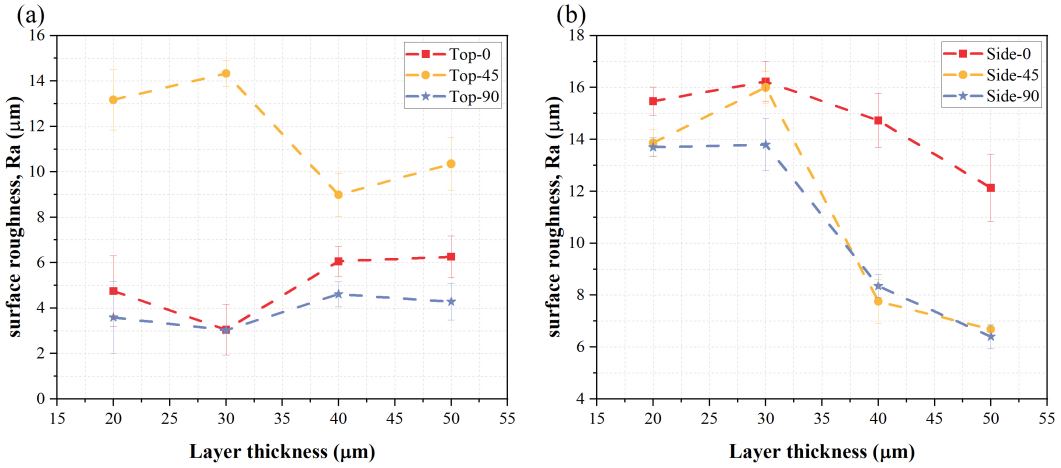

Figure 4.13: Influences of powder layer thickness and building orientation on (a) up-facing surface roughness and (b) lateral surface roughness. P= 250 W, v= 1300 mm/s, h= 60 µm and specimens were manufactured without preheating.

4.2.4 Computed tomography analysis

As shown in Fig. 4.14, although the processing parameters are optimized, there are still many defects remaining in specimens. Moreover, the volume of pores in as-built specimen (AB) (over 5×10^{-3} mm^3) is significantly larger than specimen produced with base preheating (P+AB) (about 5×10^{-4} mm^3). The projected defect size $\sqrt{area}$ in XY plane in AB specimen of 90 % cumulative frequency is about 103.6 µm (Fig. 4.15a), which is about 36 % higher than the P+AB specimen (75.7 µm, Fig. 4.15c).

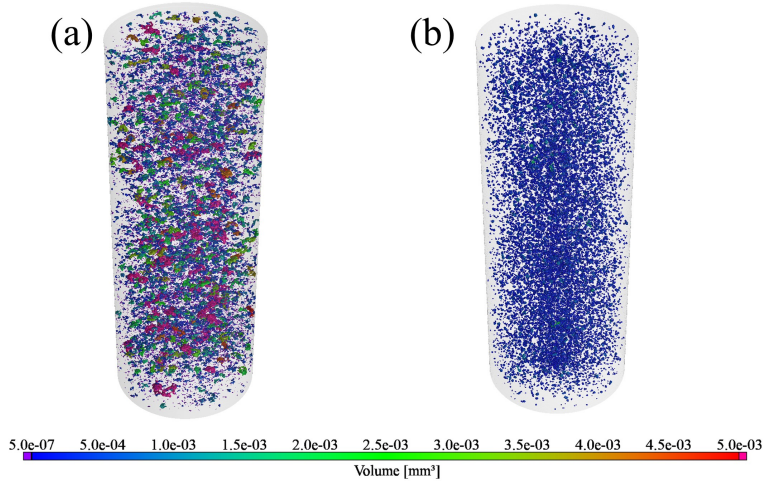

Figure 4.14: CT analysis of defect size in (a) as-built (AB), and (b) with base preheating (P+AB) specimens.

The sphericity distribution of pores (as shown in Fig. 4.16) in the AB specimen is approximately 20.7 % lower than that of the P+AB specimen (Fig. 4.15b and d), which suggests that the AB specimen has a higher incidence of lack of fusion defects compared to the P+AB specimen. A lower sphericity distribution of pores in the AB specimen indicates that the pores are more elongated or non-spherical in shape, which is often associated

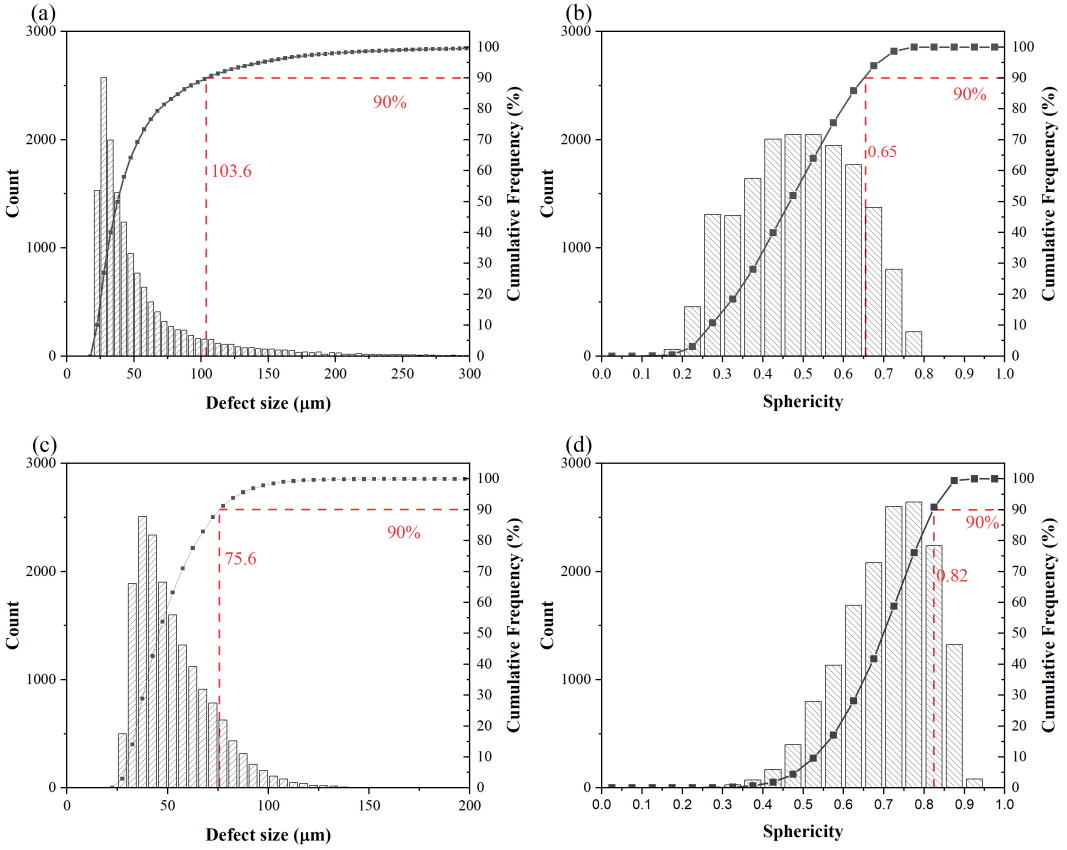

Figure 4.15: Statistical distribution of projected defect size, and sphericity of (a) (b) AB and (c) (d) P+AB specimens. 90 % represents the cumulative frequency.

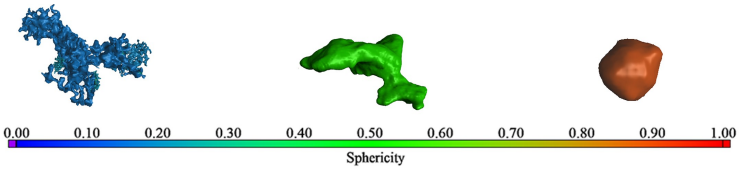

Figure 4.16: Illustration of sphericity of defects from 0 to 1.

with lack of fusion defects. Therefore, the lower sphericity distribution of pores in the AB specimen suggests that the specimen has a higher proportion of lack of fusion defects compared to the P+AB specimen.

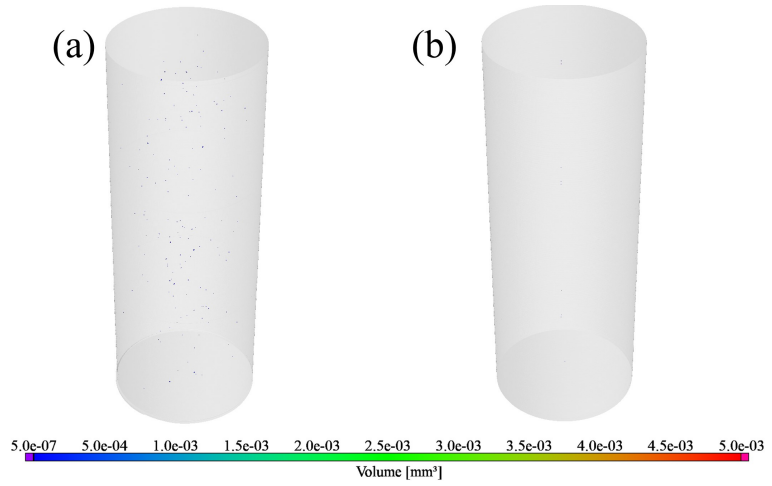

Figure 4.17: CT analysis of defects in (a) AB and (b) P+AB specimens after HIP heat treatment.

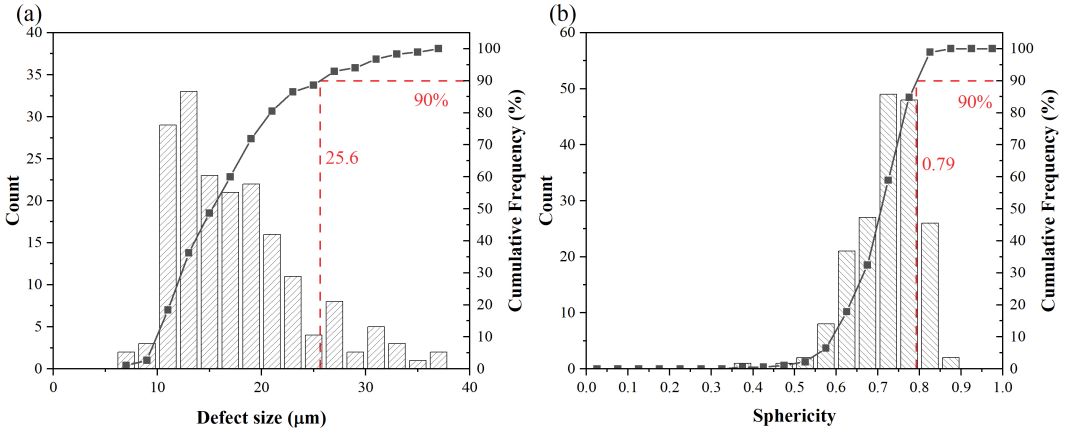

Figure 4.18: Statistical distribution of (a) projected defect size along the axis direction, and (b) sphericity of AB specimen after the HIP.

The number and volume of defects in specimens are promiently reduced after the HIP treatment, as shown in Fig. 4.17, indicating HIP is efficient in closing defects in specimens. However, it can be found that some pores still remain in the specimen after HIP treatment, especially in AB specimen (Fig. 4.17a). The statistical results (Fig. 4.18) show that the projected defect size in AB specimen reduces by 75 %, and the sphericity of defects increases from 0.65 to 0.79, compared to AB specimen without HIP heat treatment.

4.2.5 Discussion

4.2.5.1 Influences of single processing parameters on defects

As shown in Fig. 4.19, the influences of single processing parameters on the relative density (RD) are presented here. The time that the laser and powder are in contact is

dependent on the laser scanning speed. Fast scanning speed could produce a smaller size of the melt pool in both width and depth because of shorter interaction time and energy density, which could also cause a severe balling effect due to Plateau-Rayleigh instability [52], as shown in the single-track section. A low scanning speed is beneficial for increasing the interaction time between laser and powder, hence leaving sufficient time for pores to escape and improve the density of the melted zones. However, a low scanning speed could inversely increase the possibility of intense spattering and increase keyhole pores.

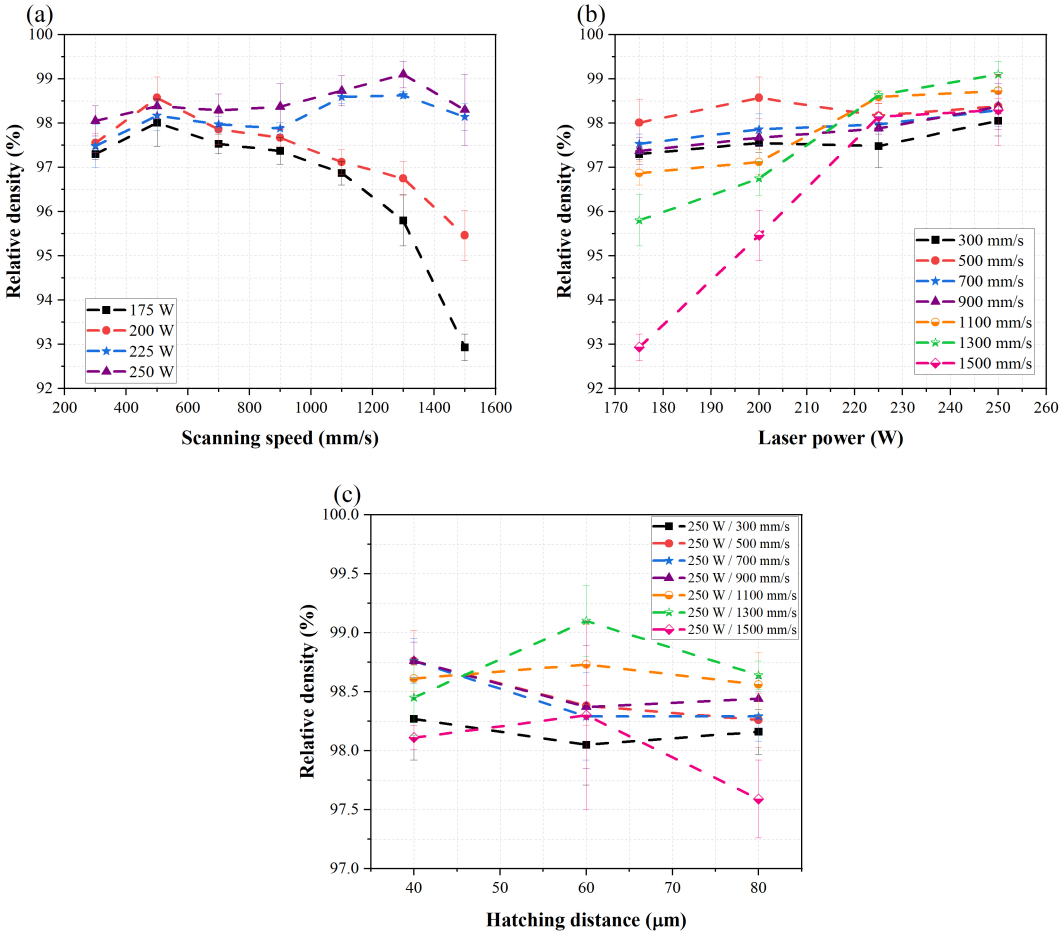

Figure 4.19: Influences of single processing parameters (a) scanning speed, (b) laser power and (c) hatching distance on the relative density of bulk specimens manufactured by PBF-LB; Layer thickness t= 30 µm.

When the laser power P $\leq$ 200 W, the RD reduces with increasing the scanning speed, which can be ascribed to the LoF defects. However, the RD is firstly improved and then dropped with increasing the scanning speed when P > 200 W. This can be explained by the domination of keyhole defects with increasing the scanning speed when the laser power is kept constant, and LoF becoming the dominant defect when scanning speeds exceed 1300 mm/s.

As aforementioned, defects are influenced by the laser power prominently, such as LoF pores. In general, high laser power easily induces a deep penetration depth and has a strong evaporation effect in the melt pool and hence high recoil pressure to entrap gas in

the melt pool after the quick solidification, for example, the keyhole pores. In contrast, the powder layer cannot be melted completely with lower laser powers (P $\leq$ 200 W), thereby leaving many LoF defects in specimens and resulting in low RD.

The overall relationship between the laser power and the RD demonstrates that the RD increases with an increase in the laser power. Furthermore, the RD of specimens is drastically improved with increasing the laser power especially when the scanning speed is higher than 900 mm/s. However, it does not show much improvement in the RD when increasing the laser power with a scanning speed less than 900 mm/s. The reason could be that the increase of laser power deteriorates the keyhole effect while scanning with a relatively low velocity, so the RD is not improved prominently.

Nevertheless, the increase of laser power is beneficial to reduce the LoF and keyhole defects when combined with a high scanning speed ($\geq$ 1100 mm/s), and that is why the improvement in the RD of specimens produced with high scanning speed is prominent when increasing the laser power, as shown in Fig. 4.19b. Additionally, it can also be concluded that LoF defects influence the RD more significantly than keyhole pores.

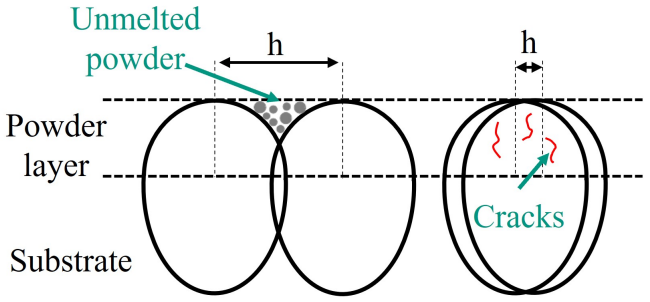

Figure 4.20: Influences of different hatching distance on neighbouring tracks.

Large hatching distances make the neighbouring tracks not densely melted and leaving unmelted powder. Meanwhile, too small a hatching value could lead to the overheating of a large proportion of former scanned areas, thereby inducing severe hot cracks in martensitic steels, as shown in Fig. 4.20. Although it seems that the changes in the hatching distance do not significantly affect the RD according to Fig. 4.19c, it still can be found that the increase in the hatching distance is detrimental to the improvement of the RD especially when the laser scanning speed is high ($\geq$ 1100 mm/s).

Fig. 4.21 shows the influences of laser power and scanning speed on the crack density (CD). It demonstrates that the crack density is increased with an increase in the laser power (Fig. 4.21a). Meanwhile, the crack density is reduced while increasing the scanning speed (Fig. 4.21b), indicating the low laser power combined with a high scanning speed is an optimization choice for reducing the crack density in PBF-LB AISI 4140 steel, but this strategy is opposite to reducing LoF defects as discussed above.

It is noteworthy that the impact of varying the laser power on crack density is limited when the scanning speed is not less than 900 mm/s, suggesting an acceptable crack density still

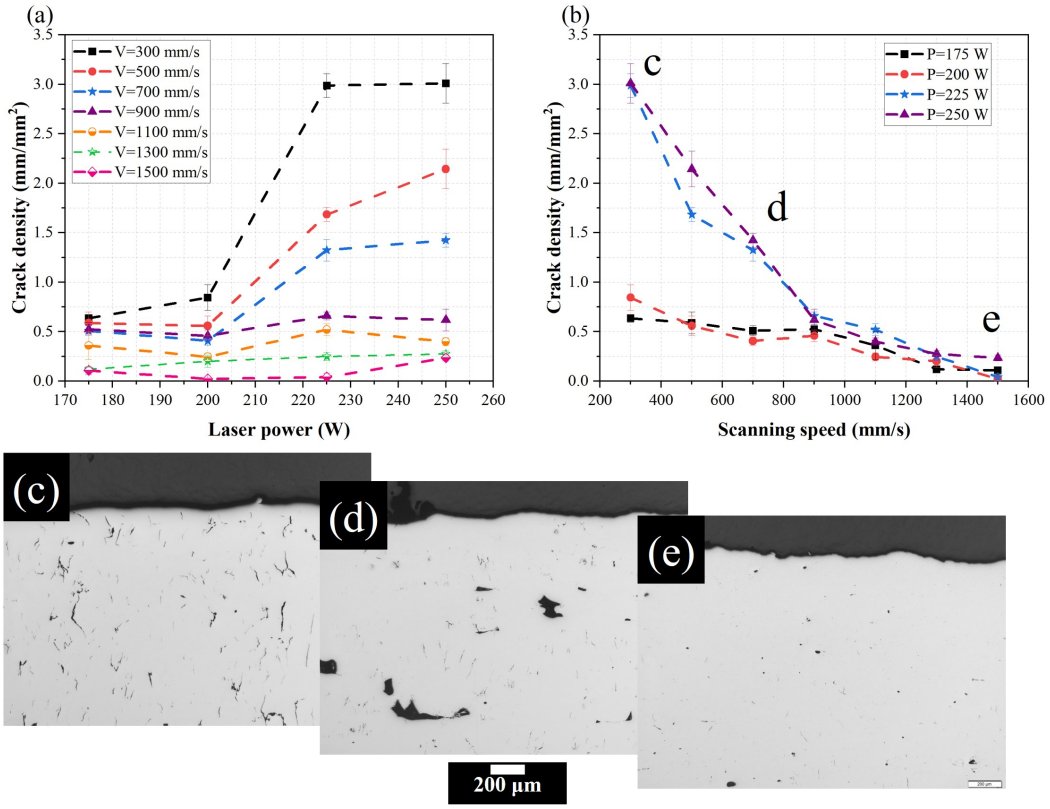

Figure 4.21: Influences of processing parameters (a) laser power and (b) scanning speed on the crack density of bulk specimens manufactured by PBF-LB (without preheating). Microcracks in micrographs of (c) 250 W-300 mm/s, (d) 250 W-700 mm/s and (e) 250 W-1500 mm/s. h= 60 µm and t= 30 µm.

can be obtained by simply increasing the scanning speed beyond 900 mm/s, even combined with a high laser power.

4.2.5.2 Influence of Volumetric energy density on defects

The manufacturing quality of the workpiece is influenced by the comprehensive effects of processing parameters, including laser power, laser scanning speed, hatching distance and even layer thickness. Volumetric energy density (VED), which incorporates these key parameters, is commonly used to comprehensively evaluate the effect of processing parameters on defects, and it can be expressed as follows,

$$VED = \frac{P}{vth} \tag{4.2}$$

where P is laser power, v is laser scanning speed, t is powder layer thickness and h is hatching distance. The VED of the optimized parameters with the highest RD and the least crack density for AISI 4140 is about 106.8 J/mm^3 (P= 250 W, v= 1300 mm/s, t= 30 µm, h= 60 µm) in this investigation, and this value is close to the value of about 80-100 J/mm^3 as reported in the literature [66].

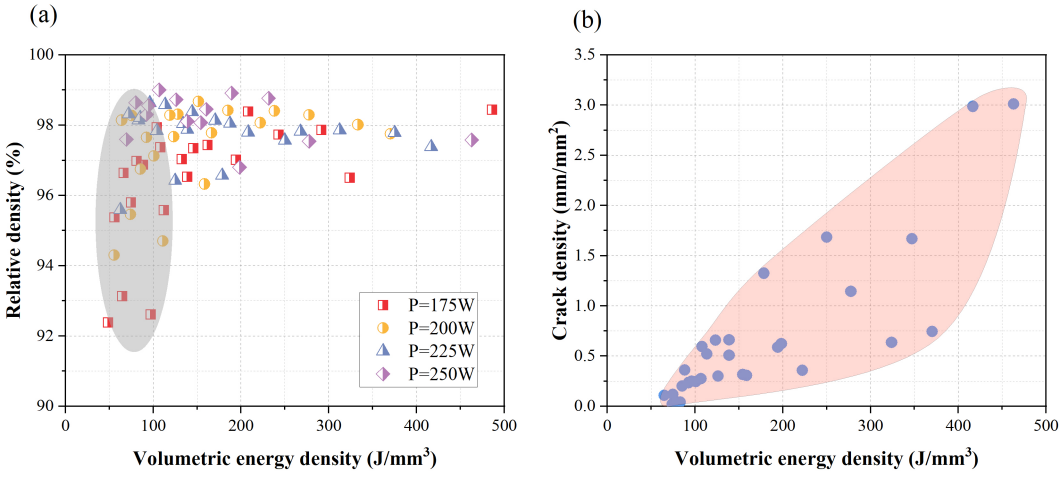

Figure 4.22: The relationships between the volumetric energy density and (a) relative density, (b) crack density [124].

However, it should be noted in Fig. 4.22 that the RD of some samples tested in the experiment is still very low (ranges from 92 % to 94 %) even with a similar VED value (around 100 J/mm^3) to the specimen which has the highest density, and it could be ascribed to the low laser power combined with a lower scanning speed resulting in a similar VED, such as 175 W-1000 mm/s. The unexpected results demonstrate that laser power is the most suitable reference to obtain specimens with a higher relative density rather than the VED.

The almost linear relationship between the energy density and the maximum crack density in Fig. 4.22b suggests that AISI 4140 is susceptible to microcracks when manufactured with high VED value. The crack density can reach up to 3 mm/mm^2 when the VED is over 400 J/mm^3. The related reasons can be explained as follows: 1. High energy

density induces a steep temperature gradient and hence high residual stress during the layer-wise process due to rapid melting and solidification; 2. The expansion during the martensite transformation of AISI 4140 also increases the risk of cracking; 3. The lack of substrate preheating could also deteriorate the cracking susceptibility because of the steep temperature gradient within the top layers; 4. overheat due to small hatch.

The VED value is also determined by the layer thickness according to Eq. 4.2. However, it should be kept in mind that the layer thickness also depends on the particle size distribution of powder. The layer thickness could be potentially increased when the diameter of the powder particle is larger than the layer thickness (30 µm), resulting in a decrease of the VED. Meanwhile, large particle size could also leave voids between particles, and thus induces LoF defects especially when there are no sufficient fine particles to complement these voids. However, the d_{50} and d_{90} of particle size distribution are 20.9 µm and 28.4 µm in experiments, respectively, thus it is possible to form continuous and homogeneous layer thickness at 30 µm.

To sum up, the most efficient and reliable method to reduce LoF defects in the bulk PBF-LB AISI 4140 parts is to control the laser power, namely, improving the laser power to reduce LoF defects. The VED is not closely related to the relative density, but the crack density is highly susceptible to high VED values. Consequently, a high laser power (250 W) combined with a relative fast scanning speed (1300 mm/s), and a layer thickness t of 30 µm and a hatching distance h of 60 µm is the optimized choice to obtain a VED of 106.8 J/mm^3. This configuration ensures a high relative density (> 99 %) and a low crack density (0.39 mm/mm^2) in the PBF-LB of AISI 4140 steel.

4.2.5.3 The formation of protrusions

It is found that there are many protrusions with a diameter around several hundred microns on the up-facing surface of specimens, which could be responsible for the coarse surface roughness of as-built specimens. When the laser interacts with the powder, the geometry of the melt pool is prone to stretch to the two edges along the scanning direction due to the recoil pressure and Marangoni convection [126]. Then the geometry of the melted powder recovers to a semioval shape on the substrate because of the surface tension during the cooling stage. However, some liquid zones which are extended far away from the melt pool could form small protrusions, and areas in the vicinity of these protrusions are easy to trigger LoF defects.

Moreover, large spattering particles induced by the ejection of metal vapour remain unmelted or are partially incorporated into the melt pool, thereby forming protrusions on the surface of tracks. This phenomenon also has been observed by Nassar et al. [127]. It is also reported that splashing prevails when manufactured with high laser power and low scanning speed because of the long-time life of over-heated liquid [128], so protrusions could be caused by high laser power in this investigation.

The balling effect induced in single tracks is an important potential reason to induce protrusions from the powder bed. The existence of balling defects makes the recoated powder

layer not homogeneously distributed, which could trigger more defects and protrusions on the surface of top layers due to the alternating of local layer thickness, and the related scheme is shown in Fig. 4.23. In fact, protrusions are not found on the surface of specimens produced with substrate preheating in this investigation. Song et al. [129] reported that the substrate preheating is beneficial to improve the wettability between layers near the substrate, thereby hindering the influence of the balling effect on subsequent layers. As a result, reducing ejection from the melt pool and the balling effect by optimizing the processing parameters, and adopting substrate preheating are potential solutions to reduce protrusions on the surface, and eventually also to reduce surface roughness.

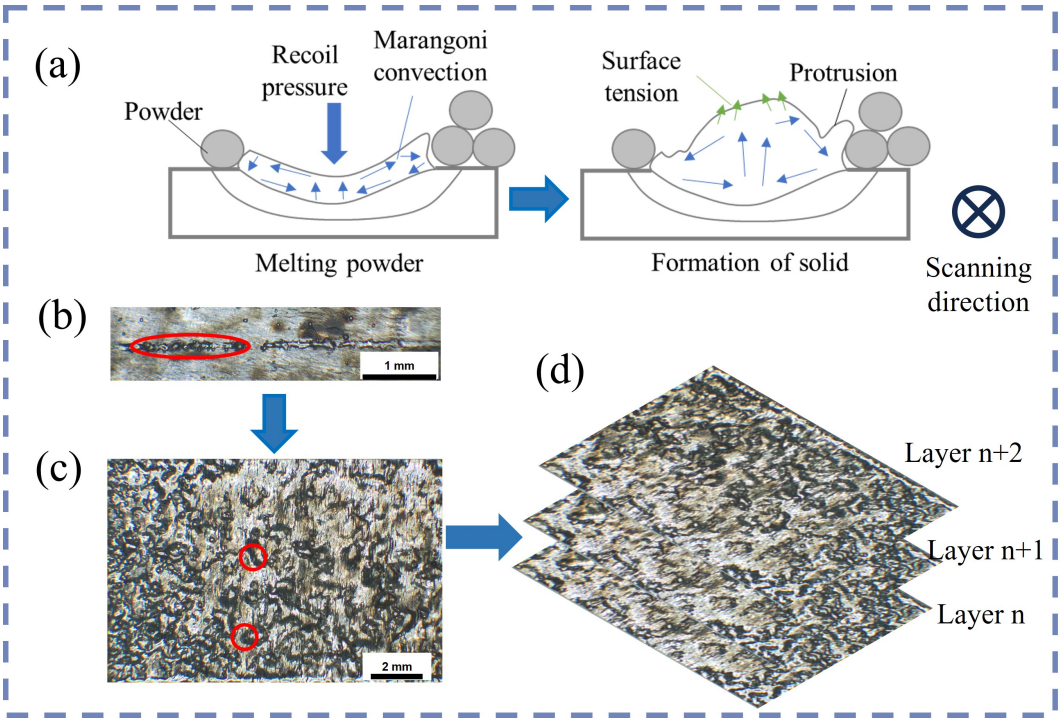

Figure 4.23: (a) Schematic of protrusions induced in the melt pool and (b) (c) (d) the formation of large protrusions on the final layer.

4.2.5.4 Influence of processing parameters on surface roughness

The decrease of laser velocity is beneficial to keep a stable melt pool geometry during the scan, thereby reducing spattering effect and possible protrusions on the up-facing surface, which could be the reason for lower roughness compared to that scanned with high velocity. Moreover, a high scanning speed combined with low laser power is prone to inducing terrible surface roughness due to the balling effect and unmelted powders, particularly seen in the surface roughness of specimens produced with 175 W/1500 mm/s. However, using a low scanning velocity or high laser power results in a larger width of the melt pool, thus adhering more partially melted powder particles on the lateral surface and increase the lateral surface roughness.

In regards to the comparatively worse lateral surface roughness of transversely built specimens compared to others build orientations, it can be explained that the transversely built

specimen has longer scanning boundaries than the vertical and 45° built specimens, which could cause defects, such as balling and necking due to the instability of the melt pool during the long-distance scanning. This highlights that the lateral surface roughness of specimens is more affected by the length of the boundaries in the scanning plane of each layer, rather than the height of specimens.

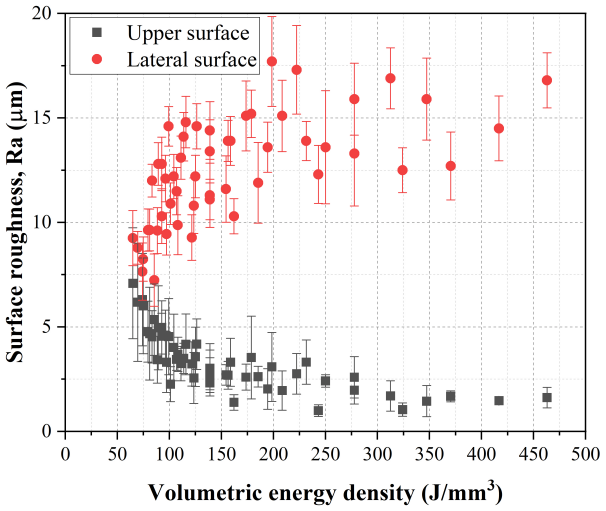

Figure 4.24: The relationship between the volumetric energy density and surface roughness.

The relationship between the volumetric energy density and surface roughness (Fig. 4.24) further shows that the upper surface roughness decreases with increasing the energy density, but the lateral surface roughness shows an inverse increase trend with increasing the energy density. This indicates that it is difficult to simultaneously reduce surface roughness in the transverse and vertical planes during the PBF-LB.

In a short summary, an increase in scanning speed or a decrease in the volumetric energy density is helpful to reduce the surface roughness on the lateral surface, while increasing the laser velocity or decreasing the volumetric energy density can increase the upper surface roughness due to increased balling and unmelted powders. The up-facing and lateral surfaces of specimens built vertically have a lower surface roughness compared to those produced transversely. The layer thickness of 30 µm can be regarded as a threshold value, as the up-facing surface roughness increases when the layer thickness exceeds 30 µm, but the roughness on the lateral surface decreases with an increase in layer thickness.

4.2.5.5 Influences of manufacturing orientation on geometry

In the PBF-LB experiments, it is found that building orientation affects the geometry promiently. Due to the contraction of the part during the cooling state, maximum tensile residual stresses occur at ends connecting the substrate, thus horizontally produced specimens are prone to upward warping deformation, as shown in Fig. 4.25. During the manufacturing process, the upward movement of the already solidified layers leads to a decrease in the thickness of the subsequent recoated powder layer, resulting in size deviations of the complete component, and the reduction in diameter can reach up to 27 %.

However, vertically produced samples do not experience severe warping deformation due to the small contact area with the substrate. Consequently, manufacturing workpieces in vertical direction is a better strategy to avoid severe warping deformation compared to the horizontal orientation.

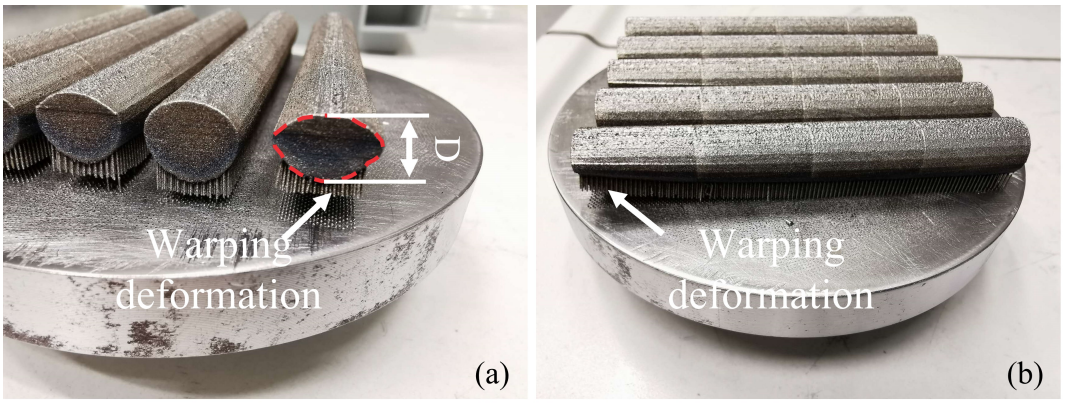

Figure 4.25: Warping deformation of horizontally produced specimens (without preheating). P= 250 W, v= 1300 mm/s, h= 60 µm and t= 30 µm.

4.2.5.6 Influences of HIP on defects

During the HIP process, the material undergoes plastic deformation and flow under high temperature and pressure, resulting in closure of pores in the material. However, the material may be subjected to high temperature again, which leads to reopening of the previously closed pores due to stress relaxation in the subsequent heat treatment process, as shown in Fig. 4.26b and c. Behrens et al. [130] also reached similar conclusions while simulating porosity regrowth during heat treatment after HIP in Titanium components.

Meanwhile, it can be found that (Fig. 4.26d) the small LoF defect in the vicinity of unmelted particle is hard to be closed, which could be hindered by these particles during the HIP process, or the HIP pressure of 110 MPa is not sufficient to close defects totally. Additionally, as reported by Kunz et al. [131], the remaining argon in a pore due to the low solubility, will increase the opposing force during the volume reduction, thereby leaving some pores open in the HIP process.

4.3 Laser remelting

Laser remelting is a promissing in-operando treatment during PBF-LB to reduce potential defects in parts. However, questions including the choice of remelting processing parameters, remelting steps and its influence on the mechanical properties are unclear. In this section, laser remelting process is investigated, covering optimization of laser processing parameters, such as laser power and scanning velocity, as well as the impacts of laser remelting and remelting steps on the melt pool size.

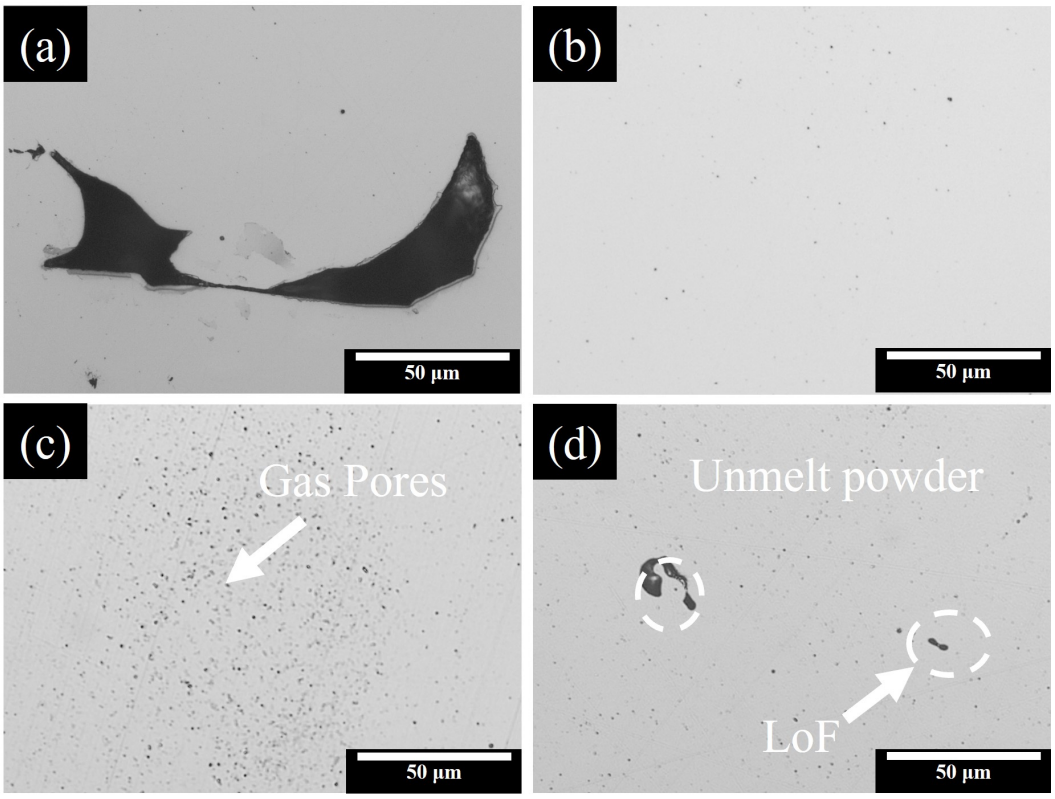

Figure 4.26: In the middle regions of specimens: (a) the as-built specimen without HIP, and (b) the specimen treated only with HIP, and (c) (d) shows remaining defects of gas pores and LoF defects after the HIP+QT treatment.

4.3.1 Optimization of remelting processing parameters

The heat map depicted in Fig. 4.27 (also see Table A5) shows the distribution of RD after laser remelting, with the highest RD reaching 99.63 % when the remelting power is 200 W, and the remelting scanning speed is 780 mm/s. The RD of R1 (remelting once) specimens using these optimized remelting parameters is improved by 0.94 % compared to as-built specimens without laser remelting (R0, 98.7 %, with the processing parameters of P= 250 W, v= 1300 mm/s, h= 60 µm and layer thickness t= 30 µm). However, when the R1 remelting laser power exceeds 225 W and the remelting scanning speed varies from 650 to 1170 mm/s, the RD values (98.29-98.75 %) are not prominently improved and even drop.

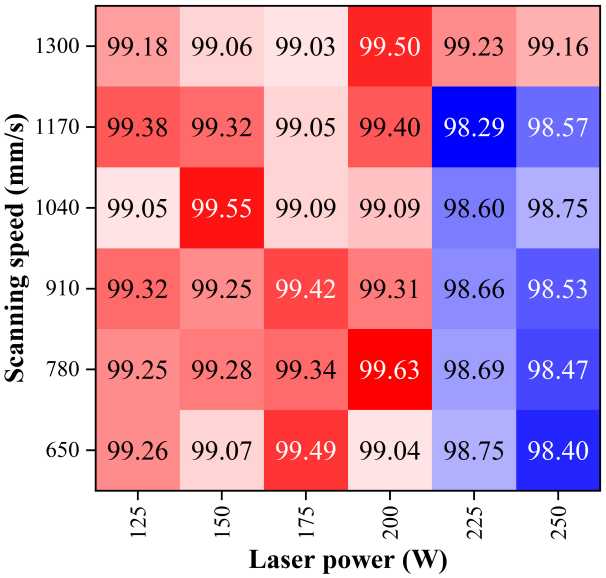

Figure 4.27: The relationship between remelting processing parameters and relative density. The parameters for the first melting: P= 250 W, v= 1300 mm/s, h= 60 µm and t= 30 µm [121].

As demonstrated in Fig. 4.28, the defects in the R0 specimen, consisting of large, spherical pores with a mean size of 41 µm, are transformed into tiny spherical pores with mean diameters of 14 µm and 9.4 µm in the R1 and R2 specimens, respectively, after laser remelting. While the reduction in pore size is significant, the crack density increases from 0.3 mm/mm^2 in the R0 to a mean value of 0.41 mm/mm^2 in the R1 specimen. Additionally, although the RD in the R2 specimen, 99.2 %, is not further enhanced after the second remelting, the crack density in the R2 (0.61 mm/mm^2) is about 47.8 % higher than in the R1 specimens, indicating the increased number of remelting steps is detrimental to cracking prevention.

4.3.2 The single-track dimension

The width and depth analysis of single-tracks, scanned with various remelting steps (R0-R2), shows that the width and depth of the melt pool both increase as the number of remelting steps increases (Fig. 4.29). The width and depth of the R1 melt pool increase by 15.41 % and 80.2 %, respectively, compared to R0, indicating LR is significant in

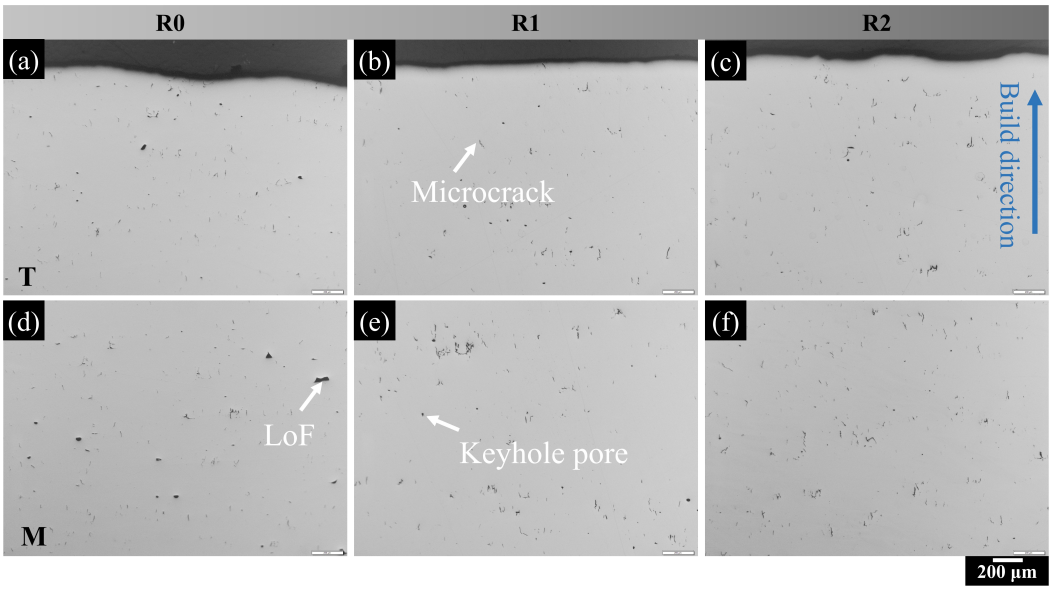

Figure 4.28: Optical images of specimens manufactured with remelting steps from 0 to 2 (R0-R2), showing the dominating defects in specimens. T-top, M-middle zones [121]. The parameters for the first melting (R0): P= 250 W, v= 1300 mm/s, h= 60 µm and t= 30 µm; The parameters for the remelting (R1 and R2): P= 200 W, v= 780 mm/s and h= 60 µm.

enhancing the melt pool depth. Moreover, the width and depth increase by 25.3 % and 24.6 %, respectively, compared to R1 when further increasing the remelting steps to two.

Additionally, it can be found from the morphology of the experimental single tracks (Fig. 4.29a, R0) that LR can effectively minimise necking defects resulting from the instability of the melt pool in the single track that has not previously been remelted, which is helpful in reducing LoF defects. However, the particles adhering to the boundaries of the tracks increase with increasing the number of remelting steps from R0 to R2.

4.3.3 Surface roughness

As depicted in Fig. 4.30, the surface roughness value of the upper surface is reduced from Ra 5.41 (R0) to 1.93 µm (R1), representing a 64 % reduction. After undergoing two remelting steps, the surface roughness is further reduced from Ra 1.93 to 1.46 µm, approximately a 24 % reduction from R1, demonstrating that the upper surface quality can be improved by increasing the number of remelting steps [121]. This trend is also reflected in the variation of Rz.

However, the roughness on the lateral surfaces is not significantly affected by LR steps, with the roughness even increasing. Specifically, the R2 specimen has higher values of Ra and Rz on the lateral surface (increased by 4.5 % and 2.9 %, respectively) than R0 specimens, indicating an increase in the number of LR steps can be detrimental to reducing the roughness of lateral surfaces.

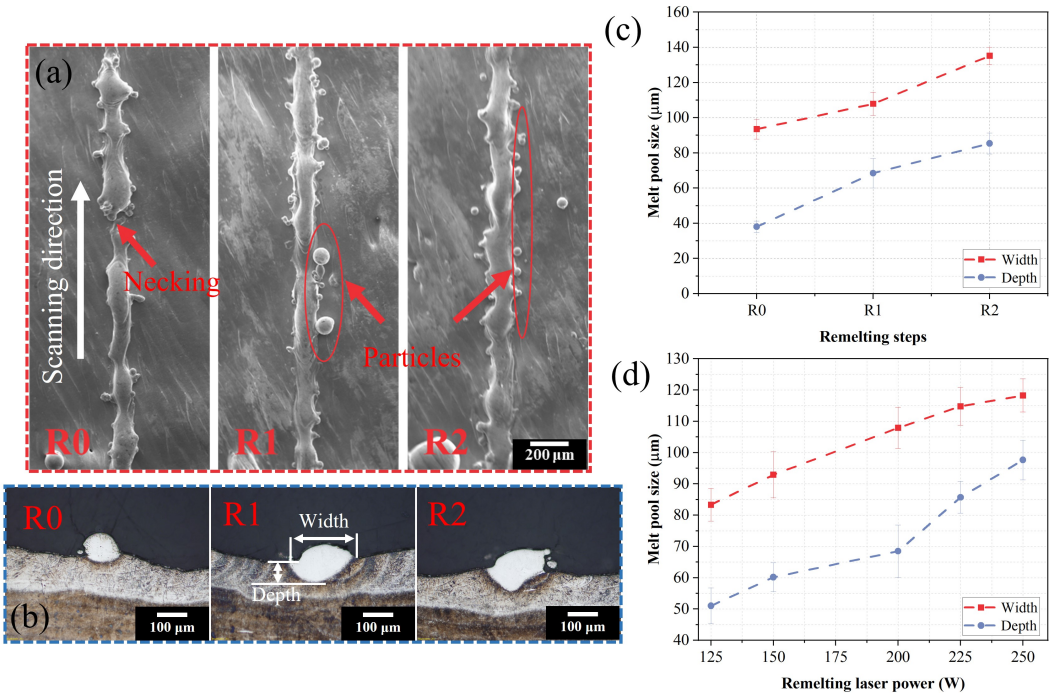

Figure 4.29: The morphology and geometry sizes of single-tracks produced with various remelting steps from 0 to 2. (a) the morphology of single tracks along the scanning direction, (b) the cross-section of the tracks perpendicular to the scanning direction, (c) the relationship between remelting steps and melt pool size, and (d) influence of remelting laser power on the melt pool dimensions (R1) [121].

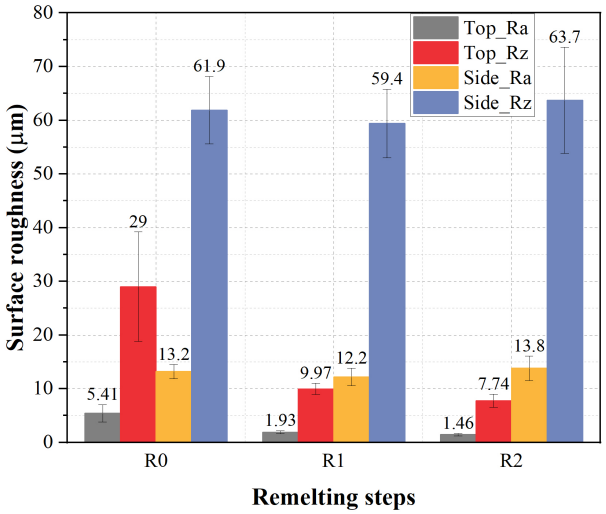

Figure 4.30: The surface roughness of both upper and lateral surfaces for specimens produced with different remelting steps [121]. The parameters for the first melting (R0): P= 250 W, v= 1300 mm/s, h= 60 µm and t= 30 µm; The parameters for the remelting (R1 and R2): P= 200 W, v= 780 mm/s and h= 60 µm.

4.3.4 Discussion

4.3.4.1 Influence of laser remelting on relative density

The relationship between the melt pool sizes and the remelting laser power shown in Fig. 4.29(c-d) shows that as the remelting laser power increases, the width and depth of the melt pool also increase. The larger melt pool size in R1 compared to R0 could be explained by the preheating effect of the previous laser scanning and the higher thermal conductivity of the solid state compared to the powder state, which is also consistent with the findings reported by Zhou et al.[74]. When the remelting power increases, the preheating effect is also enhanced due to the high input energy density, thereby increasing the melt pool sizes including width and depth. Additionally, the absence of powder in the path of the laser, which would normally absorb and scatter the laser, could also be a reason for the enlarged melt pool size during laser remelting.

Regarding the specimen fabricated with high remelting power, for example, 225 and 250 W in this study, especially when combined with a relatively low scanning speed, such as 780 mm/s, the increase of the depth of the melt pool can result in the formation of keyhole pores caused by entrapped gas or vapor[22]. Therefore, the reason for the low RD of specimens produced with high remelting power, as shown in the heat map Fig. 4.27, can be ascribed to the keyhole pores induced by the deep melt pool.

Additionally, the relative density of R2 (99.2 %) is not further improved by simply increasing the number of remelting steps. This could also be attributed to the increased depth of the melt pool when more remelting steps are taken. Consequently, the depth of the melt pool is the most influential factor in determining the formation of pores during the LR, which further influences the RD in the remelting process.

4.3.4.2 Influence of laser remelting on surface roughness

The surface topography of the top and lateral surfaces after different remelting steps is shown in Fig. 4.31. The sharp protrusions (over 200 µm in height) in the R0 specimen, which could be caused by unmelted particles and spatters, were melted by subsequent laser remelting, as seen in R1 (< 90 µm) and the schematic is also shown in Fig. 4.32, thus the smoothing effect on the upper surface is improved by increasing the number of remelting steps.

As previously mentioned, the width of the melt pool increases with an increase in remelting steps. This makes it possible to melt or partially melt additional particles on the boundaries, which can also be confirmed from the single tracks in Fig. 4.29a. The enlarged melt pool size due to LR is beneficial in reducing defects on the inner upper surface. Consequently, only the roughness value of the lateral surface is increased as the number of remelting steps increase, while the value of upper surface roughness is reduced.

4.3.4.3 Influence of laser remelting on microcracks

The increase of microcrack density in LR processes (Fig. 4.33) can be attributed to the thermal history experienced during the manufacturing process. As the number of remelting

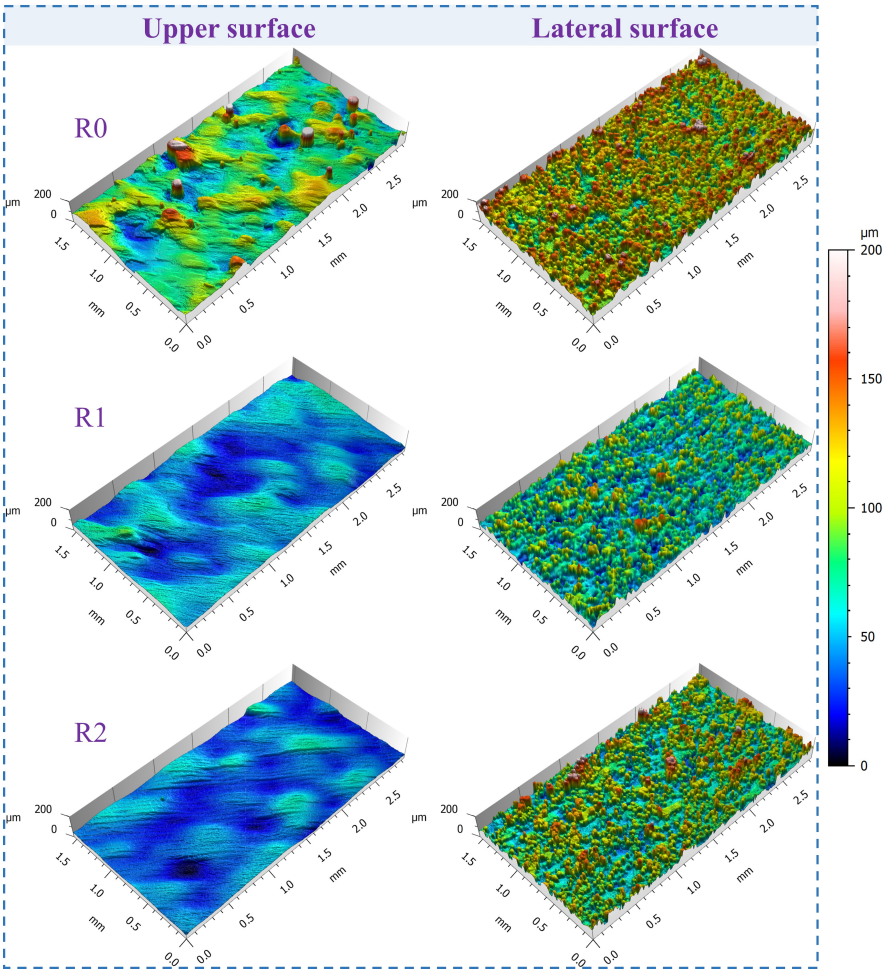

Figure 4.31: Surface morphology of specimens produced with different remelting steps from R0 to R2 [121]. The parameters for the first melting (R0): P= 250 W, v= 1300 mm/s, h= 60 µm and t= 30 µm; The parameters for the remelting (R1 and R2): P= 200 W, v= 780 mm/s and h= 60 µm.

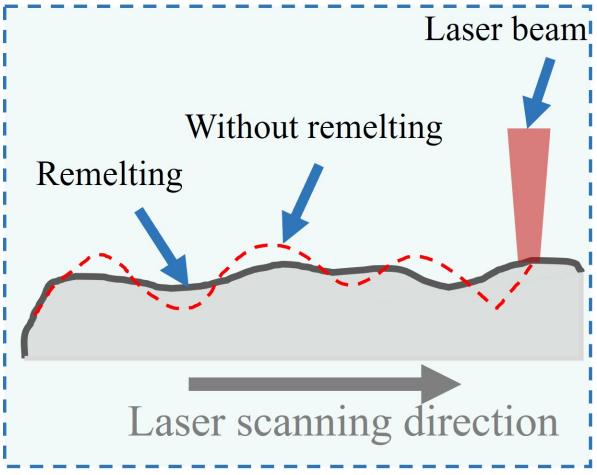

Figure 4.32: The schematic illustrates the smoothing effect of laser remelting on the upper surface of the PBF-LB specimen.

steps increases, the thermal residual stress in the specimens also increases, which could lead to the increase of microcracks. This is because during each remelting cycle, the solid material experiences fast melting and solidification with a steep temperature gradient and thermal expansion, which could cause a nonuniform distributed residual thermal stress to build up in the specimen, leading to more microcracks compared to the processes without remelting.

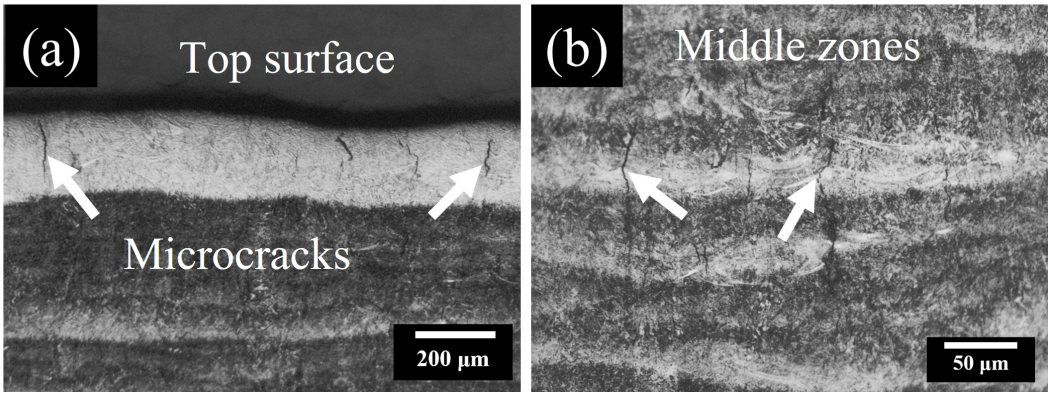

Figure 4.33: Microcracks in the R1 specimen. (a) upper surface and (b) middle zones of the specimen [121].

Although the residual stress measured from XRD decreases with increasing remelting steps, the increased crack density, from 0.3 to 0.61 mm/mm^2, in the microstructure shown in Fig. 4.28 could be a reason for the stress release with two remelting steps, which could explain why the R2 has lower residual stress compared to the R0 and R1 specimens.

During the laser remelting process, the repeatedly thermal expansion induces an increase in residual thermal stress. This elevated thermal stress level contributes to the formation of additional microcracks. However, the presence of these microcracks simultaneously alleviates the residual stress, resulting in a higher crack density 0.61 mm/mm^2 and lower residual stress values in R2 specimens.

5. Microstructure and mechanical performances

Based on the optimized laser processing parameters, microstructure and mechanical properties of AISI 4140 steels manufactured by PBF-LB are investigated in this chapter. The focus is mainly put on investigating the influences of defects arisen from inappropriate laser processing parameters on the tensile properties, Charpy impact toughness and fatigue strength, and understanding the correlations among laser processing parameters, defects, and responding mechanical properties. Moreover, the focus of this chapter is also on the mechanical properties of AISI 4140 steels fabricated by layer-wise remelting.

5.1 Microstructure

5.1.1 As-built

As shown in Fig. 5.1a and c, the main phase present in the microstructure of specimens prepared with and without substrate preheating is martensite, with an average martensite lath thickness of 2-5 µm. Moreover, it is difficult to identify carbides precipitated among martensite laths in the AB and P+AB specimens when further magnifying the images (Fig. 5.1b and d), indicating the intrinsic tempering effect is limited with regards to carbide precipitation in the PBF-LB process, even with substrate preheating. It also shows that the 200 °C substrate preheating does not change the microstructure compared to that without preheating.

5.1.2 Heat treatment

After the HIP heat treatment, the microstructure consists of ferrite and cementite, as shown in Fig. 5.2. The microstructure of specimens after the HIP + QT heat treatment are shown in Fig. 5.3, and it is easy to find some white shining Fe_3C carbides less than 1 µm in size precipitated among the martensite (Fig. 5.3b and d)), which can be ascribed to the tempering effect during the heat treatment. It is also found that the average thickness of martensite laths increases around 17 - 29 % after the HIP + QT heat treatment because of the slower cooling rate (10^2 - 10^3 K/s) in the conventional heat treatment process compared with PBF-LB manufacturing process (10^6 K/s).

5.2 Microhardness

5.2.1 Results

The microhardness of specimens fabricated with and without substrate preheating are shown in Fig. 5.4a. The microhardness of the as-built (AB) specimen is about 520 $HV_{0.1}$, which is around 14 % higher than that manufactured with substrate preheating (P+AB, 456 $HV_{0.1}$). Moreover, it is evident that the microhardness on the top surface is significantly higher (about 100-150 $HV_{0.1}$ higher) in comparison to other locations in the

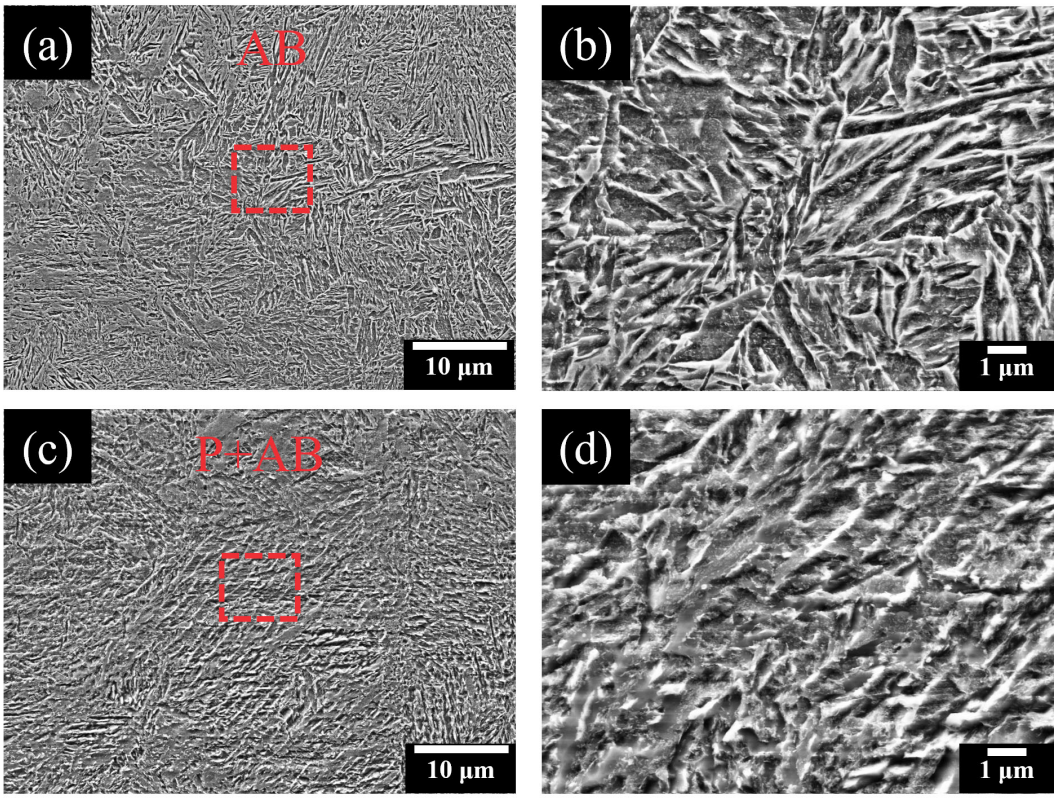

Figure 5.1: Microstructure of (a) (b) as-built specimen, and (c) (d) specimen manufactured with substrate preheating [132].

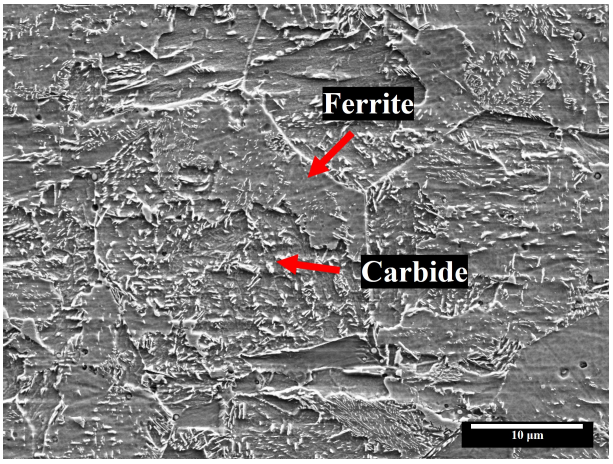

Figure 5.2: Microstructure of AISI 4140 after the HIP heat treatment.

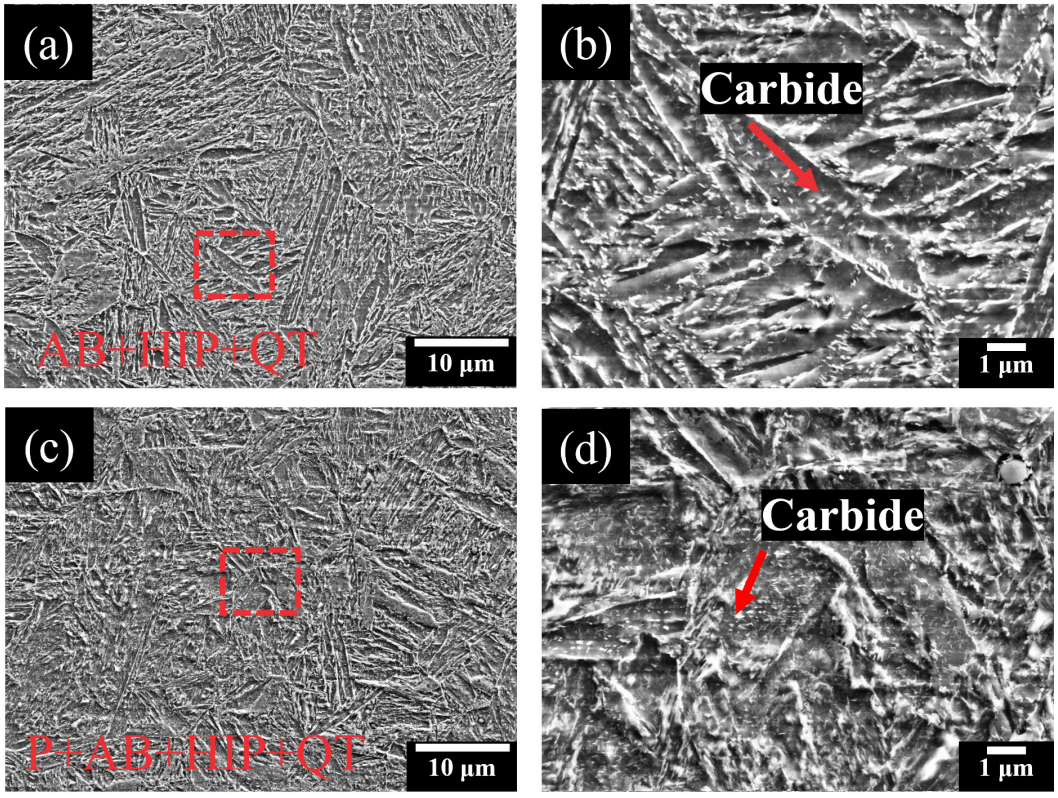

Figure 5.3: Microstructure of (a) (b) AB+HIP+QT, and (c) (d) P+AB+HIP+QT [132].

specimen. After the HIP heat treatment, the microhardness of specimens is only about 335 $HV_{0.1}$, which is reduced by around 26.58 % compared to the as-built specimen with preheating (Fig. 5.4b).

In order to have a similar microhardness to that produced by PBF-LB, the HIPed specimens are further processed with the quenching and tempering (QT) heat treatment. The microhardness distribution of HIP+QT specimen, with an average hardness value of about 465 $HV_{0.1}$, indicating the data (as shown in section 3.2.4 heat treatment) for tempering is acceptable.

5.2.2 Discussion

5.2.2.1 Influences of processing parameters on microhardness

The influence of processing parameters on the microhardness is shown in Fig. 5.5. The microhardness increases from 417 $HV_{0.1}$ to 535 $HV_{0.1}$ as the scanning speed increases from 300 mm/s to 1500 mm/s while keeping the laser power constant (250 W). However, it shows an inversely decreasing trend of microhardness (from 550 $HV_{0.1}$ to 520 $HV_{0.1}$) while increasing the laser power, demonstrating that specimens produced with low laser power and high scanning speed have higher microhardness than those manufactured with high laser power and low scanning speed.

The variation in microhardness due to different processing parameters can be ascribed to the fact that the increase in laser scanning speed and decrease in laser power all lead

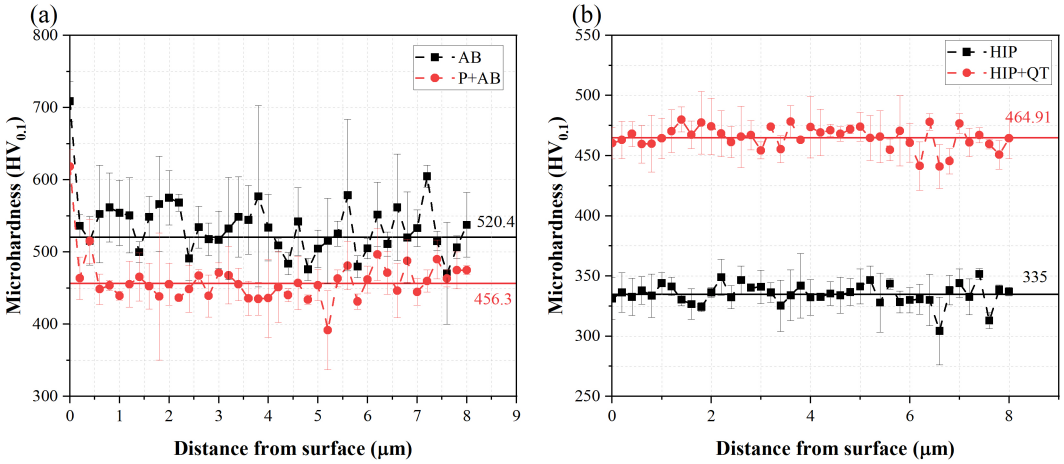

Figure 5.4: Microhardness depth profiles of (a) AB and P+AB specimens, and (b) HIP and HIP+QT specimens.

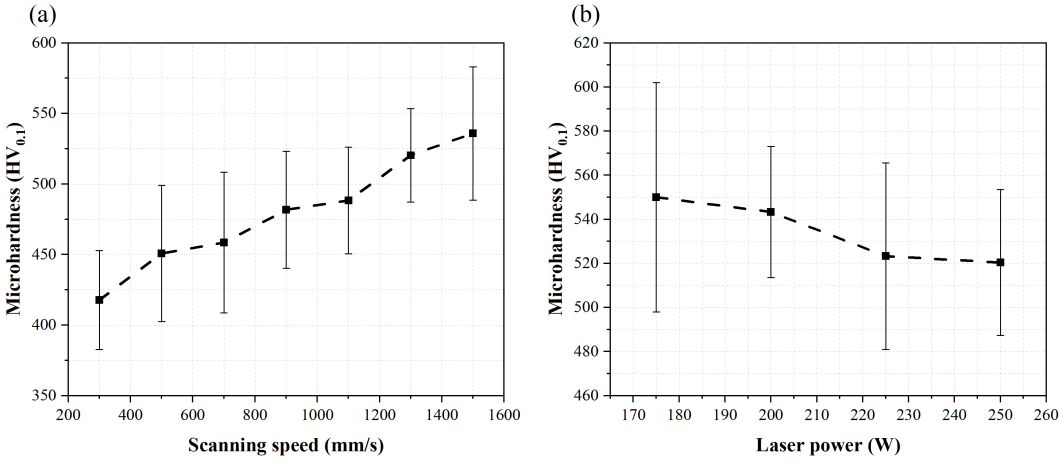

Figure 5.5: Influences of (a) laser scanning speed and (b) laser power on the microhardness. All specimens were manufactured without base preheating.

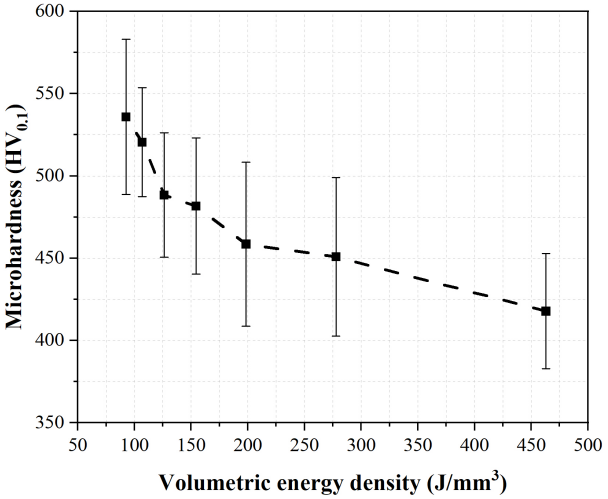

Figure 5.6: The relationship between volumetric energy density and microhardness showing the microhardness decreases with increasing the energy density (without preheating).

to the reduction of input energy density, which further reduces the intrinsic tempering effect, thereby leading to higher microhardness than specimens manufactured with high laser power and low scanning speed (Fig. 5.6).

Additionally, the AB specimen can be seen as tempered with 357 °C for 2 hours to get a mean hardness of 520 $HV_{0.1}$, and the mean tempering temperature for the P+AB specimen is 435 °C (2 hours), which highlights the significant tempering effect of substrate preheating to soften the microhardness compared to specimens without preheating.

5.3 Tensile performance

5.3.1 Results

Fig. 5.7 shows the results of tensile properties of specimens manufactured with varying processing parameters. It can be found that with increasing laser power from 175 W to 250 W, the ultimate tensile strength (UTS) and elongation to fracture increases by about 24.2 % and 285 %, respectively. However, the UTS firstly shows an increase to over 1100 MPa at the scanning speed of 700 mm/s, and then drops to 760 MPa while further increasing the scanning speed to 1500 mm/s. The elongation of all specimens tested in Fig. 5.5 is below 1 %.

The tensile properties of specimens manufactured with different building orientations and substrate preheating condition are shown in Fig. 5.8. The UTS of transversely built specimen (1214.9 MPa) is about 17.8 % higher than that of vertically built specimen (1031.7 MPa), and the yield strength of the transversely built specimen (1089.7 MPa) is about 9.2 % higher than the vertical specimen (997.5 MPa).

Additionally, the tensile properties of specimens manufactured with substrate preheating are higher than those without substrate preheating, with the UTS, yield strength and

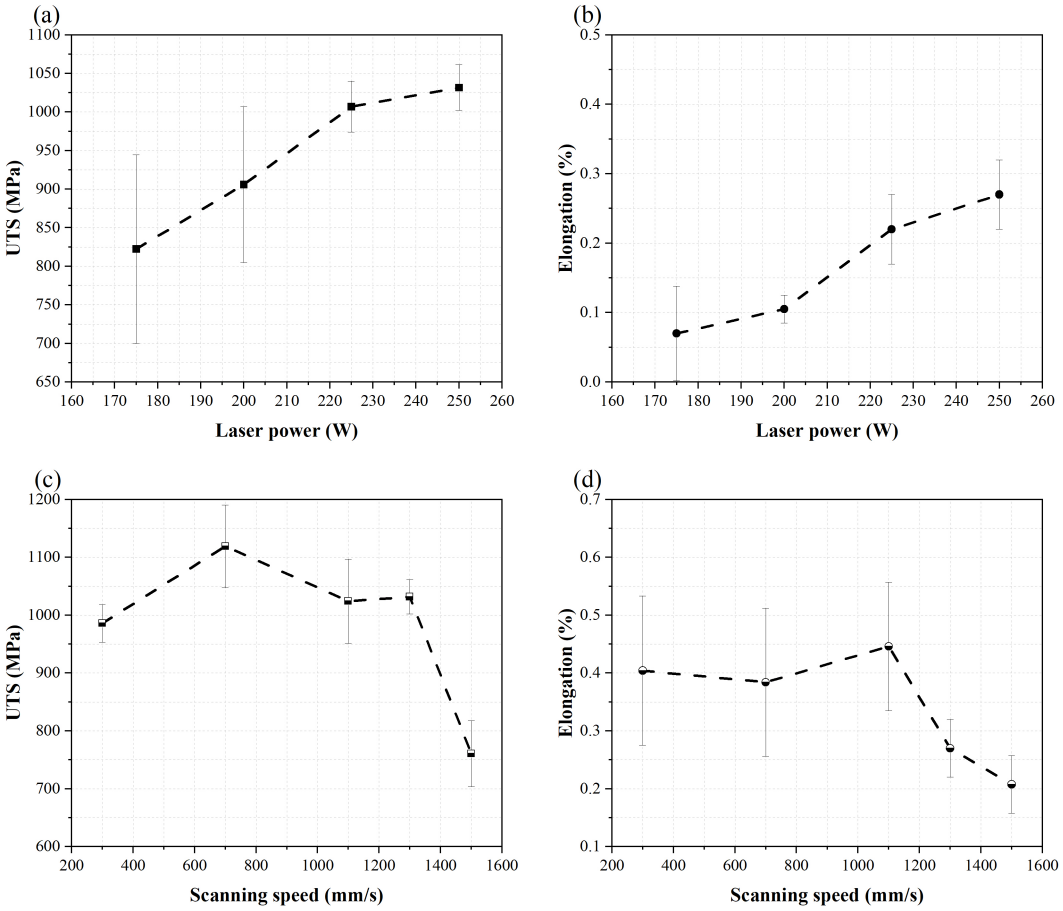

Figure 5.7: Influences of (a) (b) laser power and (b) (d) laser scanning speed on tensile properties.

elongation to fracture increase about 11 %, 13.8 % and 171 %, respectively, suggesting the transverse building orientation and substrate preheating are effective methods for improving the tensile properties.

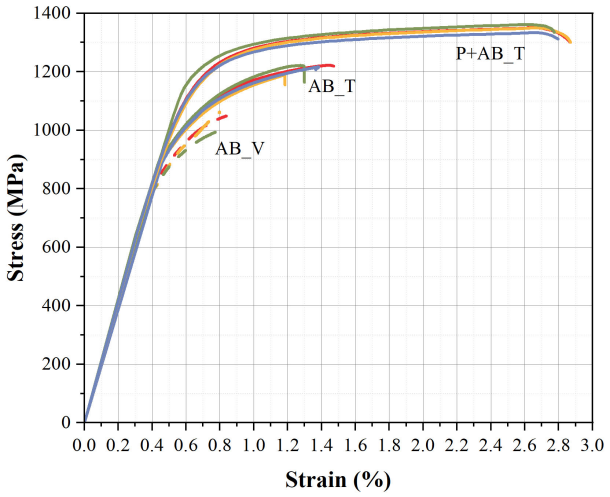

Figure 5.8: The comparison of strain-stress curves for PBF-LB specimens produced with and without substrate preheating, T- transverse, V- vertical.

5.3.2 Discussion

5.3.2.1 Influences of relative density on tensile properties

As has been discussed the increase in laser power is beneficial to reduce the LoF defects which could have high stress concentration in LoF tips. Therefore, the improvement in tensile strength is due to the decrease in LoF defects with the increase in laser power. Regarding the laser scanning speed, the reason for the reduction in tensile strength can still be ascribed to the LoF defects when the scanning speed is 1500 mm/s. However, the dominant factor affecting the tensile strength of specimens scanned with the low velocity of 300 mm/s is the transition to keyhole pores and microcracks.

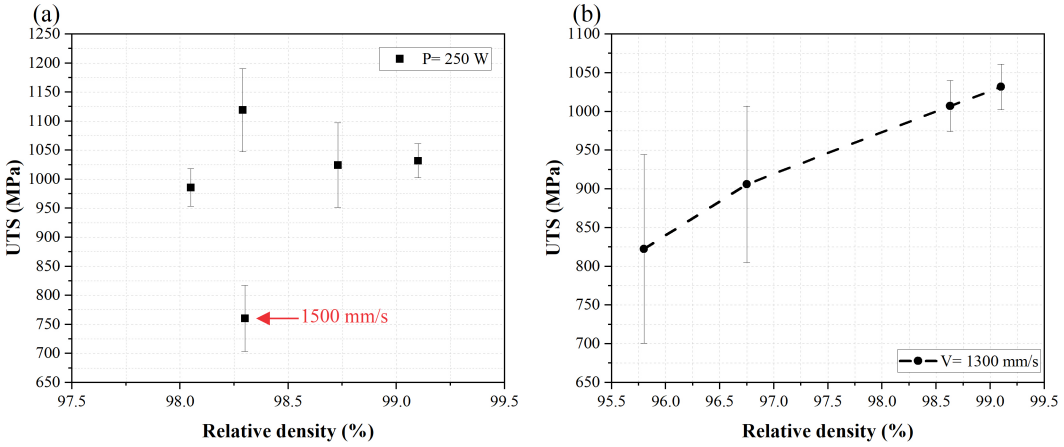

Figure 5.9: Influences of various relative density of specimens cuased by (a) scanning speed, and (b) laser power on the tensile strength of PBF-LB specimens.

On the other hand, as shown in Fig. 5.9, the interplay between the relative density and the UTS shows that variations in RD resulting from different laser scanning speeds have little effect on the UTS, except for the specimen manufactured at 1500 mm/s. However, it is noteworthy that the RD influenced by laser power exhibits a linear correlation with the UTS. When the scanning speed is set to a high value of 1300 mm/s, the variation in laser power dominantly affects LoF defects, which impact the RD, demonstrating that the tensile strength of AISI 4140 steel produced by PBF-LB is more influenced by the laser power rather than the laser scanning speed.

5.3.2.2 Influences of building orientation on tensile properties

When the specimen is built in the transverse orientation, the direction of LoF defects in the microstructure tend to be aligned parallel to the axial direction of the sample and therefore parallel to the direction of tensile loading. As a result, cracks are more likely to propagate along the direction perpendicular to the loading direction as compared to specimens built in the vertical direction, which agrees with Alfieri et al. [133] in studying the influences of build orientation on 17-4 PH stainless steel.

In general, high microhardness results in a higher yield strength. Despite the fact that the specimen produced with substrate preheating show a 14 % decrease in microhardness compared to the as-built specimen, it has higher values of the UTS, yield strength and elongation to fracture. This could be explained by the absence of microcracks and fewer LoF defects in the specimen produced with substrate preheating. Additionally, the lower microhardness of P+AB is advantageous in increasing plasticity due to stronger intrinsic tempering, which attributes to higher elongation to fracture compared to AB.

5.4 Charpy impact performance

5.4.1 Results

The results of the impact energy of PBF-LB specimens manufactured with the optimized parameters (P= 250 W, v= 1300 mm/s, h= 60 µm and t= 30 µm) and manufactured with different conditions (with 200 °C base preheating) are shown in Fig. 5.10. Regarding PBF-LB specimens, the specimens manufactured with preheating (P+AB) have the highest impact energy (20.75 J), which is 3-4 times higher than the as-built PBF-LB samples (AB) (4.79 - 5.69 J).

The microhardness of the conventionally manufactured specimen (CM) is similar to that of P+AB, but the impact energy of the CM specimen (45 J) is about 2 times of the P+AB specimen (20.75 J). However, the only differences between the P + AB and CM + QT 450 specimens are the slight difference in porosity and QT microstructure compared to P+AB. It is also worth noting that although all PBF-LB specimens were fabricated with the optimized parameters as described in the chapter 4, the RD of Charpy testing samples with large geometry sizes decreases from over 99 % to only 97.7 %. Nonetheless, the RD of the P+AB specimen seems not to be affected much (99.4 %), and the high RD value could be one of the essential reasons why P + AB samples have higher impact energy in the Charpy impact tests compared to AB specimens.

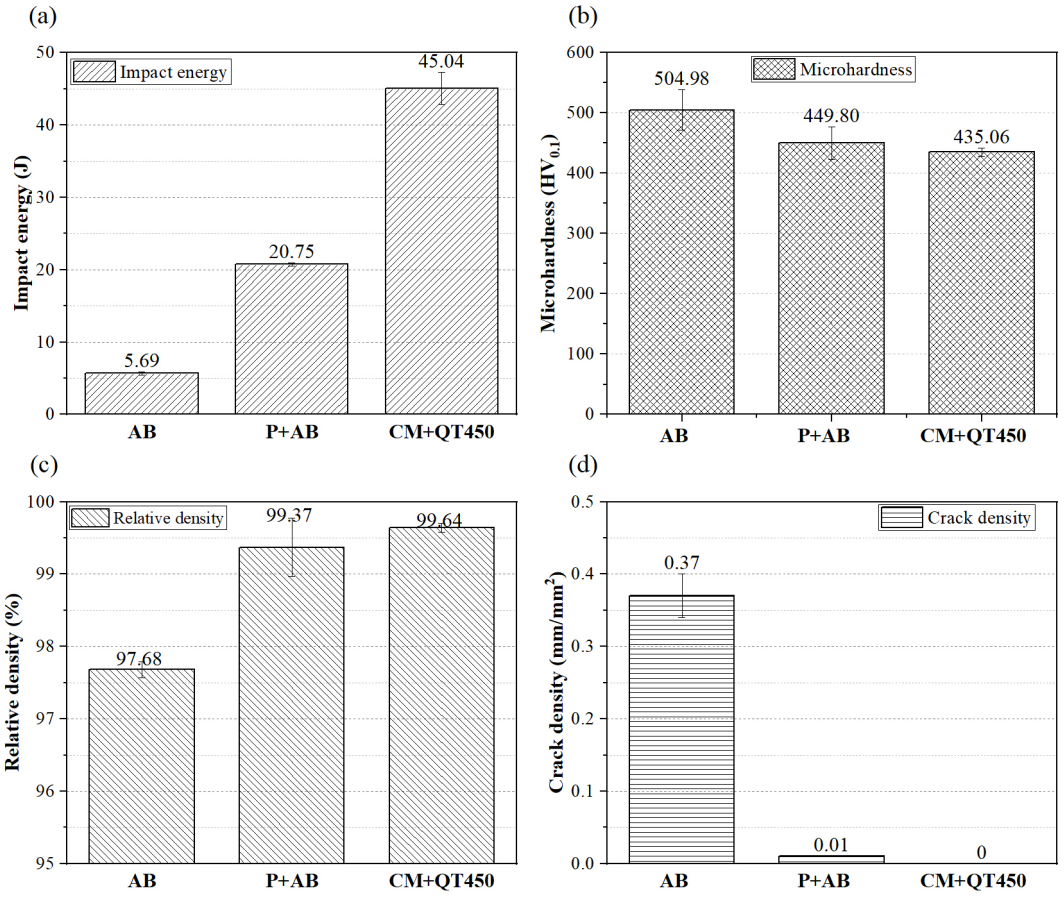

Figure 5.10: The comparison of (a) impact energy, (b) microhardness, (c) relative density and (d) crack density of PBF-LB specimens manufactured with and without base preheating with conventionally manufactured ones [124].

5.4.2 Discussion

5.4.2.1 Fracture mechanism

As shown in Fig. 5.11a, there are plenty of LoF defects in the vicinity of the fractured surfaces of the AB specimen. These LoF pores could serve as quick paths for cracks propagation because of the high stress concentration near the tips of the LoF pores [134]. The low impact energy of AB specimens can be explained by the existence of LoF pores that promote the propagation of cracks (as red arrows in Fig. 5.11a). This can also be verified from SEM figures of the impact fractured surface. As shown in Fig. 5.12a, the initial area near the V-notch and the middle region of the fractured surface exhibits many relatively smooth planes with some unmelted particles (in a dimension about 55 µm) on them. Based on the morphological characteristics observed on the fractured surface, which includes smooth fracture surfaces and the absence of plastic deformation, as shown in Fig. 5.12(a-c), the fracture mode of AB is identified as brittle fracture.

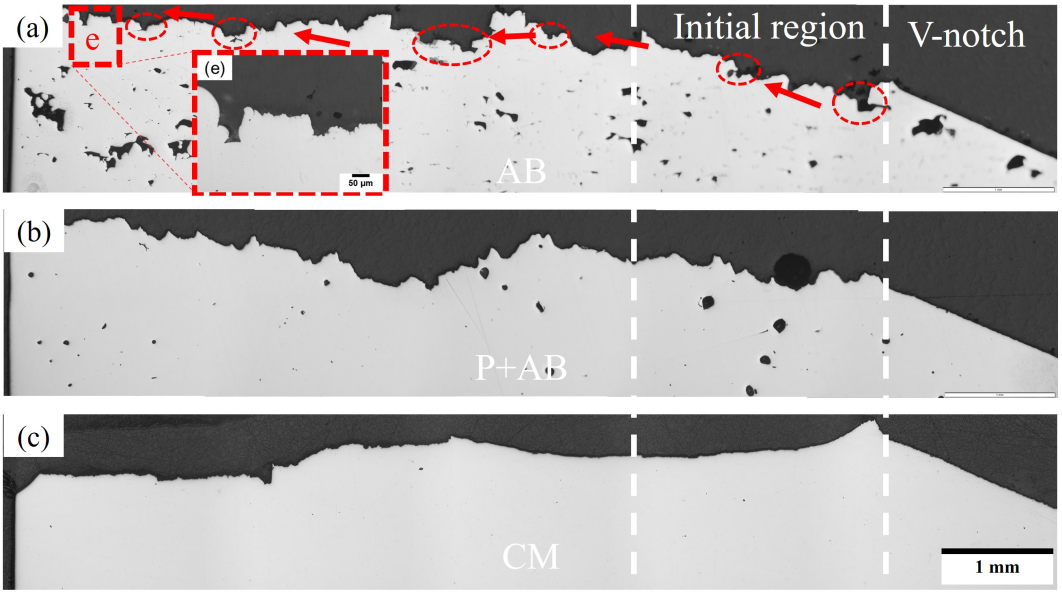

Figure 5.11: The side fractography of specimens after Charpy impact test [124]. (a) AB, (b) P+AB and (c) CM.

Additionally, small secondary microcracks in the AB specimen (Fig. 5.12c) can offer multiple paths for crack propagation. It has been reported that the more corrugated fracture surfaces are better for the impact toughness due to crack deflection and respecting energy exhaustion [76, 135]. However, it shows an inverse trend in this study (Fig. 5.11a and c). One explanation is that the jagged shape of the AB fracture surface is caused by broken LoF pores or pre-existing cracks, as it is the easiest and fastest path for cracks to propagate during the sudden impact (Fig. 5.12e). By contrast, shapes of pores in the P+AB specimen are only regular spherical or ellipsoidal keyhole pores (Fig. 5.11b), resulting in a much lower stress concentration compared to the former.

The porosity of P+AB (0.6 %) is about 74 % lower than the AB specimen (2.3 %), and no apparent cracks occurring in the P+AB microstructure. However, the P+AB

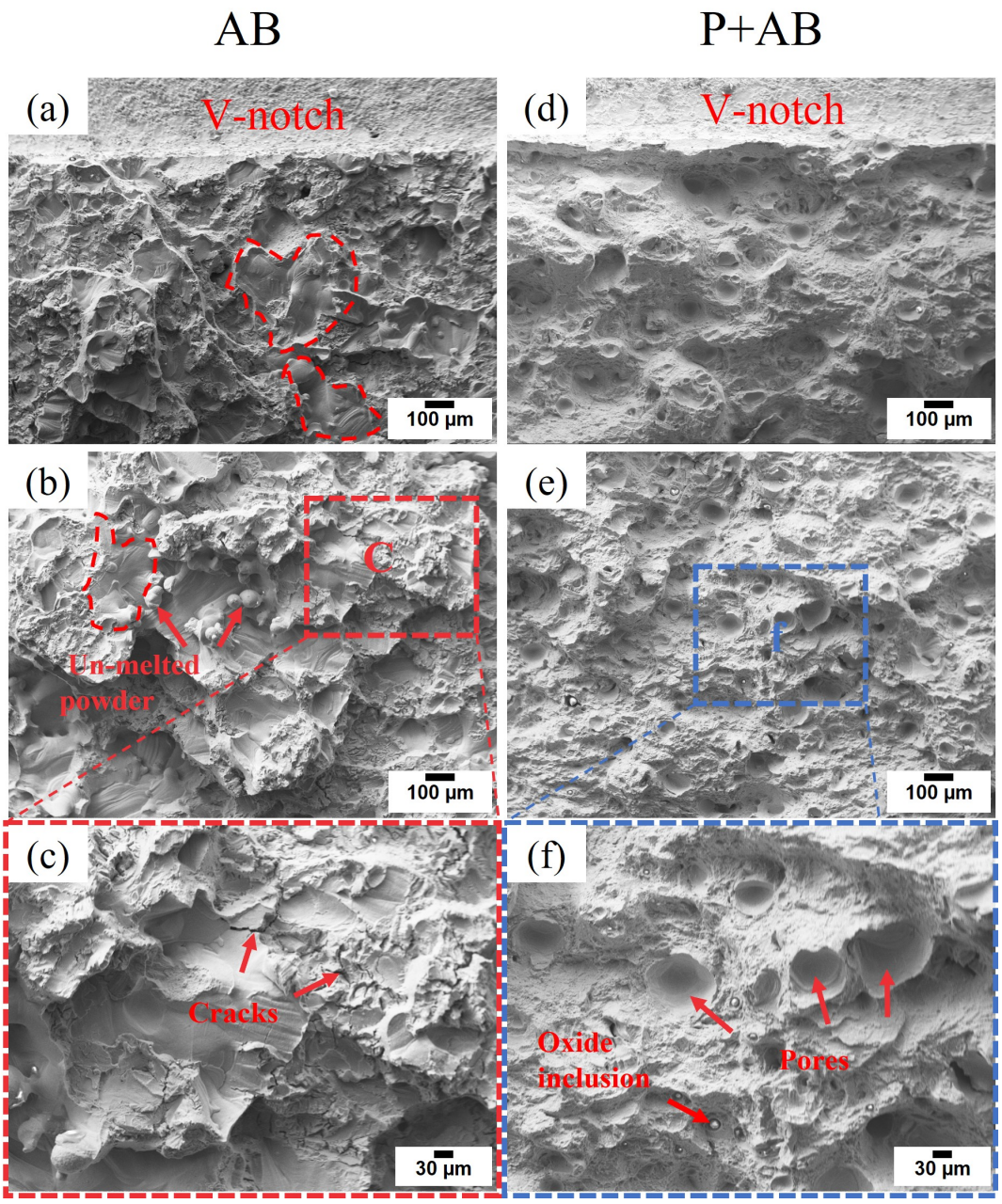

Figure 5.12: The fractography of specimens after the Charpy impact test showing the fracture mechanism and defects affecting the impact ductility [124]. (a) (b) (c) AB and (d) (e) (f) P+AB.

fractography is different from the AB specimen. There are plenty of pores of about 60 µm distributed on the fractured surface and no similar smooth planes in the P+AB specimen, which shows more ductile behaviour than the AB specimen. The dimples that arise from plastic deformation during the impact process can absorb more energy than brittle fracture without plastic deformation. Thus, the combination of low porosity, no microcracks, and low hardness, leading to the finally higher impact absorbed energy for specimens with preheating compared to those without preheating.

5.4.2.2 Influences of porosity on the impact energy

Due to the fact that the impact toughness is sensitive to porosity, as shown in Fig. 5.13, the impact energy drops sharply with increasing the porosity from 0 % to around 2 %, which could explain why the impact energy of the P+AB specimen is only 50 % of that of the CM specimen. Another aspect that should be noted is that the impact energy stays at low values (around 5 J) and does not vary much when the porosity of specimens exceeds 2 %, indicating the impact toughness is not further affected by porosity when the porosity is over 2 %. Therefore, reducing the porosity in the PBF-LB specimen is the best method to prominently improve the impact toughness.

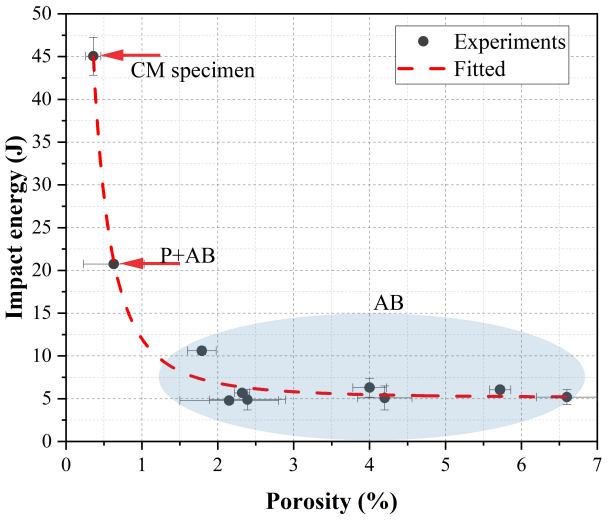

Figure 5.13: The influence of porosity in PBF-LB specimens on impact energy [124].

5.5 High cycle fatigue strength

In this section, the high cycle fatigue behaviour of AISI 4140 manufactured by PBF-LB is studied. Moreover, the influences of different levels of porosity (0-3 %) and defect sizes (50-450 µm) in as-built (AB), with base preheating (P+AB) and specimens subjected to hot isostatic pressing (HIP) are analyzed and discussed, with a focus on their impact on the fatigue strength of AISI 4140.

5.5.1 Results

5.5.1.1 Fatigue S-N curves

The S-N curves of high cycle fatigue of PBF-LB specimens shown in Fig. 5.14 demonstrate that AB specimens have the lowest fatigue limit (50 MPa), which is only about 14.3 % of P+AB specimens (350 MPa). Moreover, the fatigue strength is improved by 766 % and 51 % after the further HIP + QT heat treatment process (433 MPa and 529 MPa), separately, as shown in Fig. 5.15.

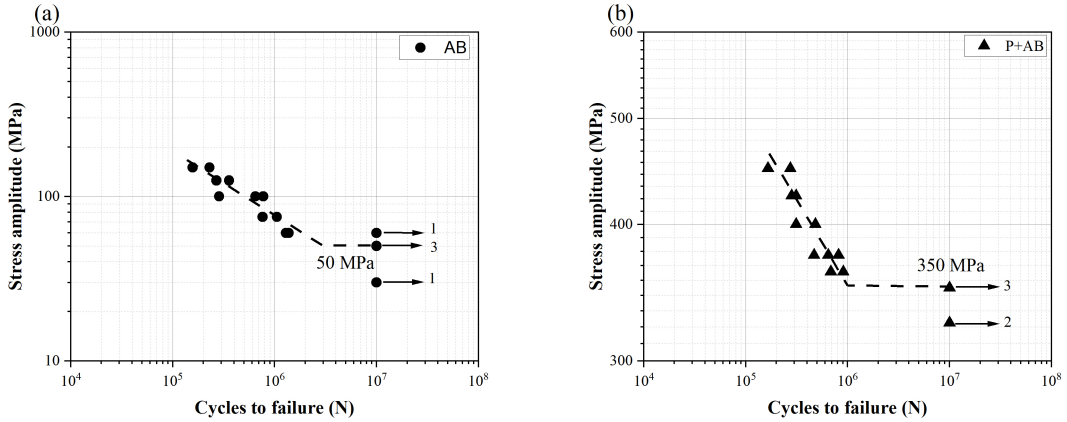

Figure 5.14: The fatigue S-N curves of (a) AB and (b) P+AB specimens.

Although the fatigue strength of the AB and the P+AB specimens are lower than that of the CM counterparts (about 450 MPa with similar microhardness [112]), the fatigue strength of P+AB is only 22 % lower than the CM reference, which is much less than the differences between AB and CM specimens. Additionally, the fatigue strength of specimens processed with the HIP + QT treatment are comparable to or even higher than the CM, demonstrating HIP is an adequate method to improve the fatigue strength of PBF-LB specimens even with a number of large-sized (400-500 µm) LoF defects.

5.5.1.2 Defects for crack nucleation

As shown in Fig. 5.16, the possible initiation sites for crack propagation are analysed on the fracture surface of failed specimens. Irregular pores in the crack initiation regions are later treated using the method proposed by Murakami as described in [119].

It can be found that the LoF defects with large sizes connected to the surface are the sites for crack initiation in AB specimens (Fig. 5.16(a-d)). Moreover, large and flat planes are observed along the edges of the LoF defect. Additionally, it is worth noting that there are two main morphologies of LoF killer defects, one is with adhering unmelted powder, around 15-20 µm, on the surface and the other is with a flat plane. It can be explained that LoF defects generally have sharp tips, which could be easier to induce stress concentration and cracking than other types of pores [136]. The existence of many large LoF defects in the vicinity of specimens' surface could impart convenient paths for cracks to propagate and coalesce quickly with each other, thereby leading AB specimens to fail at a very low stress amplitude.

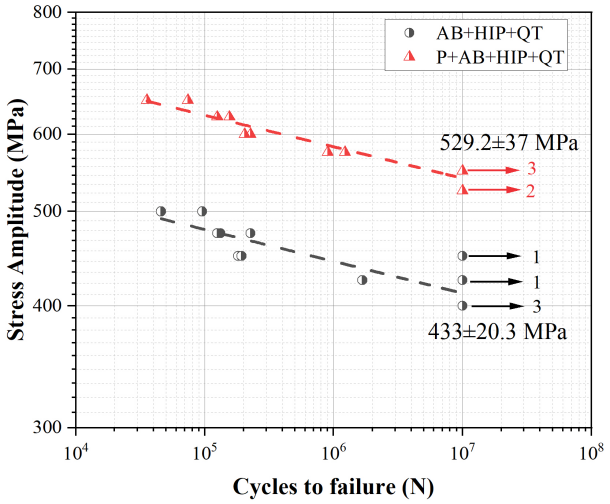

Figure 5.15: The fatigue S-N curves of AB and P+AB specimens after the HIP+QT heat treatment.

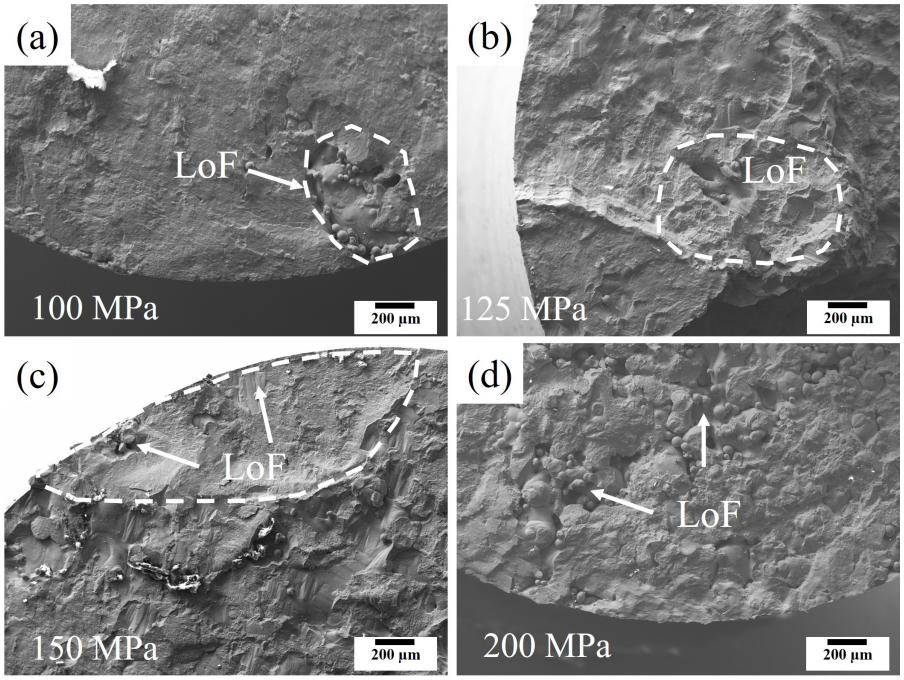

Figure 5.16: The fatigue fractography of AB specimens tested under different stress amplitudes showing the killer defects for crack initation.

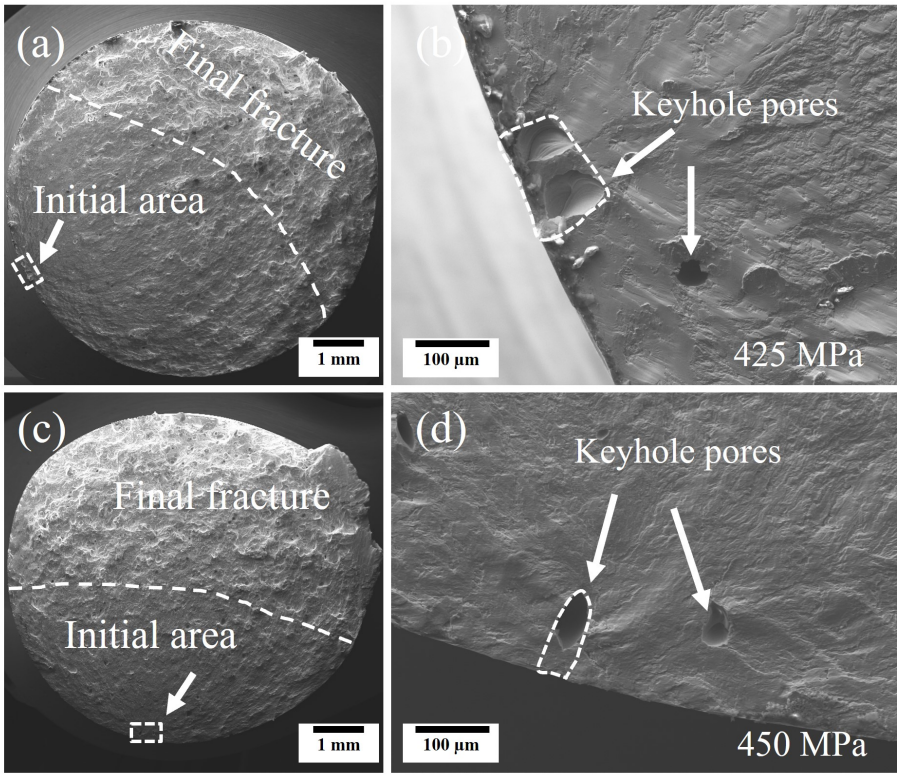

Figure 5.17: The fatigue fractography of P+AB specimens showing the killer defects for crack initation.

Crack initiation in P+AB specimens is attributed to keyhole pores that are interconnected between the surface and subsurface regions (Fig. 5.17). It also can be found that the fractography can be divided into three regions: crack initiation, crack propagation and final fracture. Moreover, the final fracture areas reduce with increasing the stress amplitude from 425 MPa to 450 MPa (Fig. 5.17a and c), indicating that an increase in the stress amplitude could reduce the crack propagation distance, resulting in the decline of fatigue life.

Matrix defects and tiny pores are the dominating killer defects for crack initiation in specimens processed with the HIP + QT treatment (Fig. 5.18). In the HIP process, most of LoF defects and keyhole pores in as-built specimens are forced to close under external pressure, thereby reducing potential crack initiation sites in specimens and thus improving fatigue strength of specimens.

5.5.1.3 Residual stress

The residual stress depth profile of PBF-LB specimens for fatigue testing and that processed with heat treatment are shown in Fig. 5.19. It can be found that the AB specimen without machining has higher tensile residual stress than that processed with mechanical machining, and the maximum tensile residual stress of specimens without machining can exceed 950 MPa, which is about 2.2 times of the maximum value for the AB specimen treated with machining. Mechanically induced subsurface plastic deformation leads to

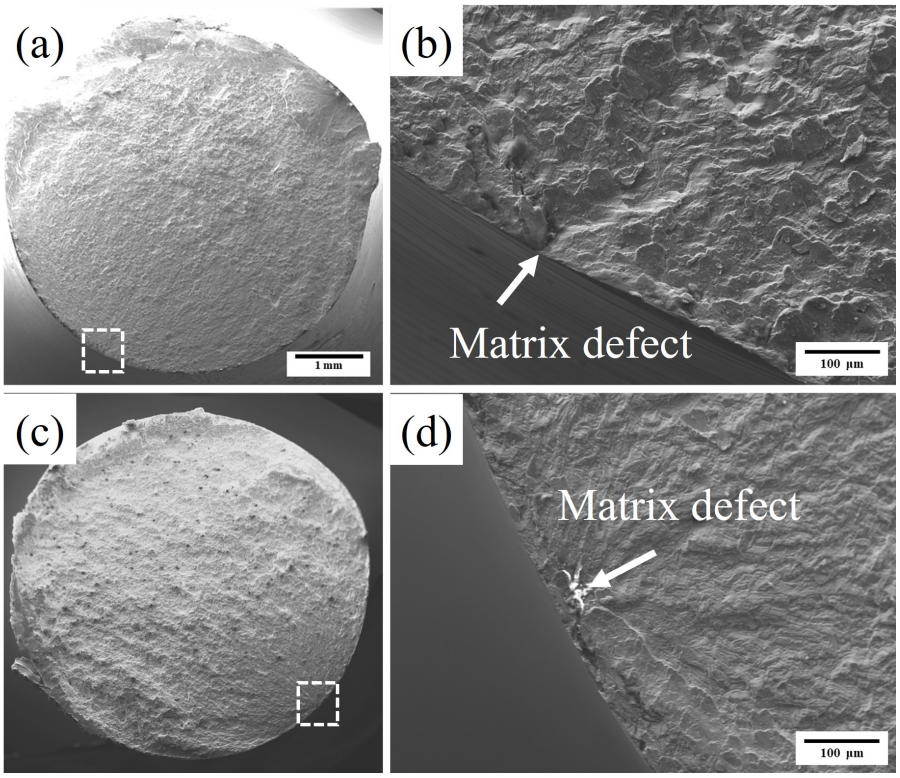

Figure 5.18: The fatigue fractography of specimens treated with HIP+QT. (a) (b) AB and (c) (d) P+AB. Here the matrix defect is regarded as cracks initiating from the intrusion in persistent slip band.

compressive residual stress in the machined workpiece, thereby releasing tensile residual stresses in PBF-LB specimens [137]. This also indicates that the as-built specimen without any post treatment could not be suitable for the implementation in fatigue loading applications.

Residual stress in the as-built specimen (AB) after machining is still tensile stress (with an average value of 341 MPa, exclude the surface value). Although machining can change surface tensile residual stress to compressive stress, it turns to tensile stress again in depths exceeding 30 µm, which can be ascribed to reduced plastic deformation caused by machining and high tensile residual stresses in original AB specimen.

After the HIP+QT heat treatment, residual stress in AB specimen decreases to a mean value of 7.7 MPa, demonstrating post heat treatment is an efficient method to release residual stress in PBF-LB specimens. The mean residual stress (beyond 30 µm in depth) in P+AB is 15.7 MPa, which is similar to the residual stress in AB+HIP+QT specimen, indicating that substrate preheating during the PBF-LB process (P+AB) can effectively reduce residual stresses via the reduction of temperature gradients in the PBF-LB process. However, the residual stress depth profile of P+AB processed with HIP+QT shows that the mean value (-43 MPa) is even lower than that of the AB + HIP + QT sample, although they were treated with the same heat treatment conditions.

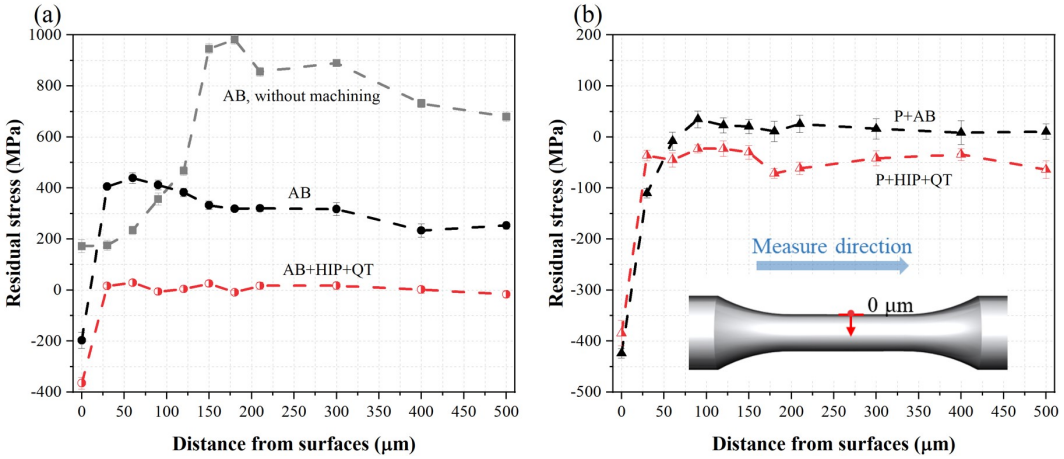

Figure 5.19: The residual stress depth profiles for (a) AB treated with and without machining; and after HIP+QT heat treatment, and (b) P+AB and P+AB+HIP+QT specimens [132]. PBF-LB specimens were machined from 6 mm to 5 mm in diameter.

5.5.2 Discussion

5.5.2.1 Fracture mechanism

Cracks propagate along the weakest direction from one LoF defect to another in multiple locations near the circumference and then coalesce with each other quickly in AB specimens, resulting in clean and flat brittle planes (Fig. 5.20(a-b)). On the contrary, river patterns and smaller cleavage facets are found at the crack propagation site and the final fracture area of the P + AB sample, while LoF defects are reduced (Fig. 5.20(c-d)). Consequently, the tearing of LoF defects is the dominant type of crack propagation in AB, which results in the lowest fatigue limit.

Regarding PBF-LB specimens treated by HIP + QT, a mix of intergranular and transgranular fracture is seen as the dominating crack propagation type for HIP+QT specimens (Fig. 5.21). Additionally, dimples with a size less than 2 μm on the grain facets indicate a mix of intergranular and ductile fractures in the final failure stage (Fig. 5.21b and d).

In AB and P+AB specimens, no prior austenite grain boundaries could be found, which can be attributed to the inhibited growth of austenite due to the fast-cooling rate in the PBF-LB process. However, the phases transform from austenite to martensite in the HIP + QT heat treatment leaving obvious prior austenite boundaries in the microstructure, as shown in Fig. 5.21. Due to the high hardness of martensite, cracks are prone to propagate along grain boundaries, where higher stresses are required for cracks to propagate through martensite. Nevertheless, prior austenite grain boundaries are relatively brittle and weak for cracks to propagate through. Furthermore, inclusions within the microstructure could lead to the final transgranular fracture of HIP+QT specimens. Inclusions with an average diameter of 2.2 μm located on the prior austenite grain boundaries allow voids to grow and coalesce at the tip of the crack front. This is also consistent with results from Abdelwahed et al. [84] in studying the AISI 4130 steel manufactured by PBF-LB, thus forming dimples

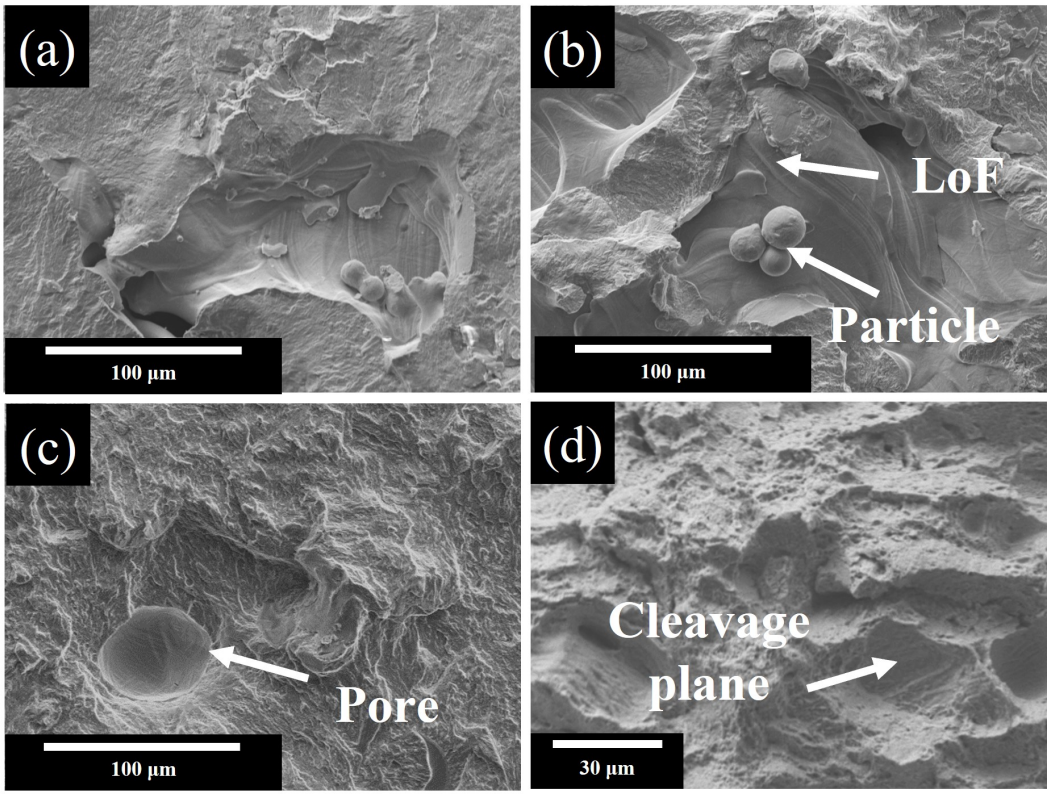

Figure 5.20: The fractography of final fracture areas for (a) (b) AB and (c) (d) P+AB specimens [132].

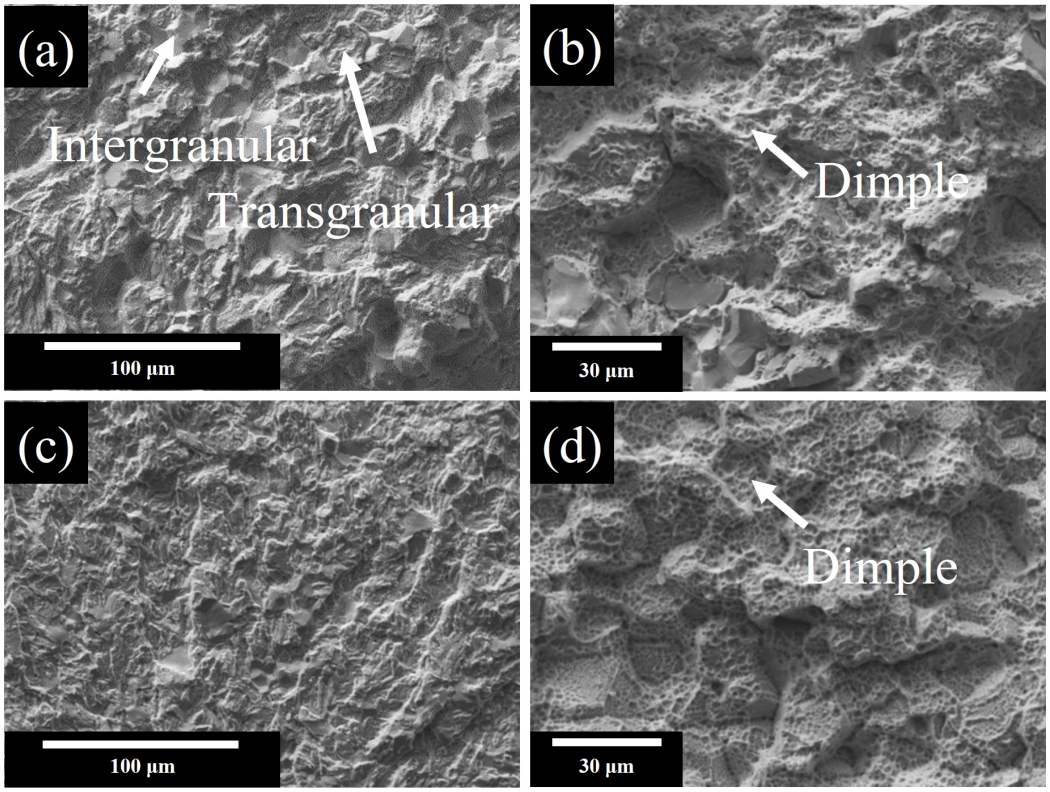

Figure 5.21: The fractography of final fracture areas for (a) (b) AB and (c) (d) P+AB specimens treated with HIP+QT [132].

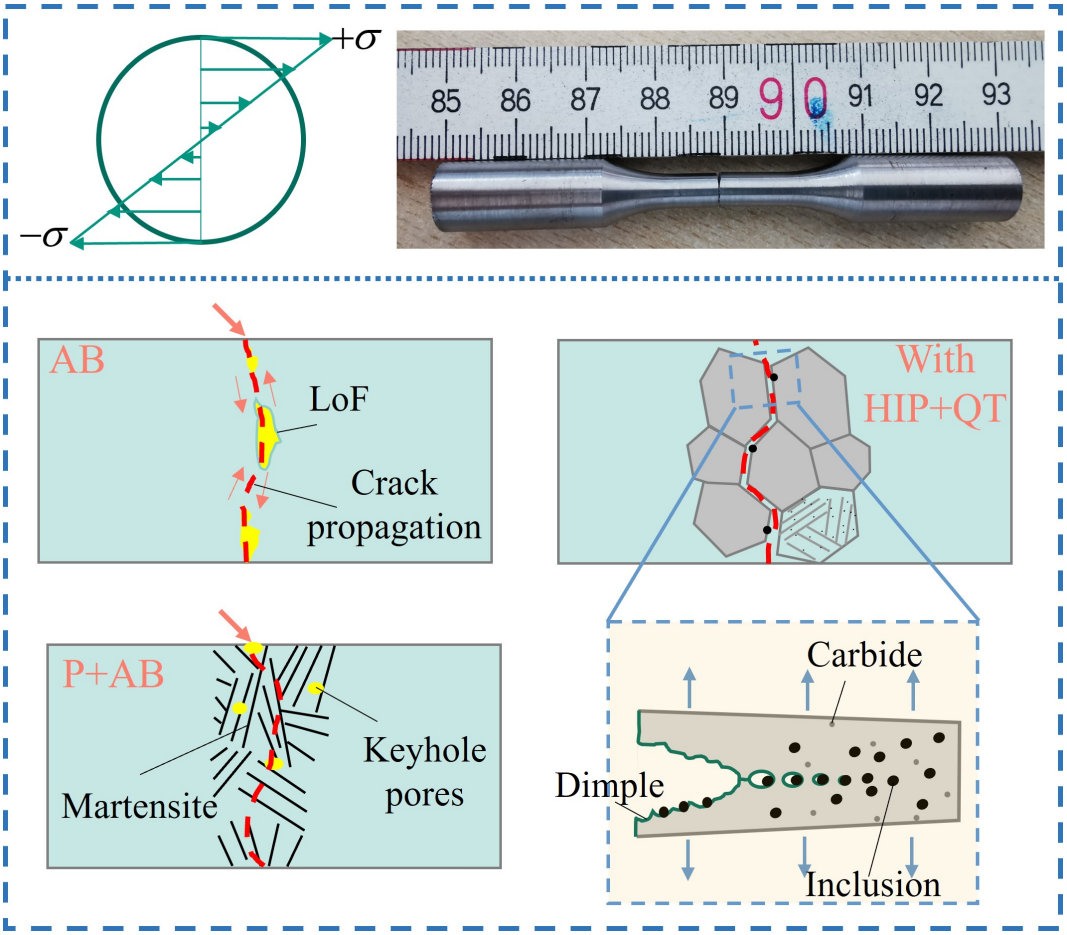

Figure 5.22: The schematic illustrates the crack propagation mechanism during the rotation bending fatigue testing in the AB, P+AB specimens and specimens treated with HIP+QT [132].

in the facets. The improved ductility of specimens after HIP+QT treatment is beneficial for inhibiting crack propagation, which further increases the fatigue life. The crack propagation mechanism in AB, P+AB and specimens with HIP+QT can be also seen in Fig. 5.22.

5.5.2.2 Influence of porosity on fatigue limit

The interplay between porosity, defect size $\sqrt{area}$, and the fatigue limit of the specimens is shown in Fig. 5.23. The results show that the fatigue limit is improved with a decrease in porosity. Here the fatigue limit influenced by porosity can be further ascribed to the change in the killer defect size, and it is shown in the red line that the defect sizes for crack initiation tend to increase while increasing porosity [132].

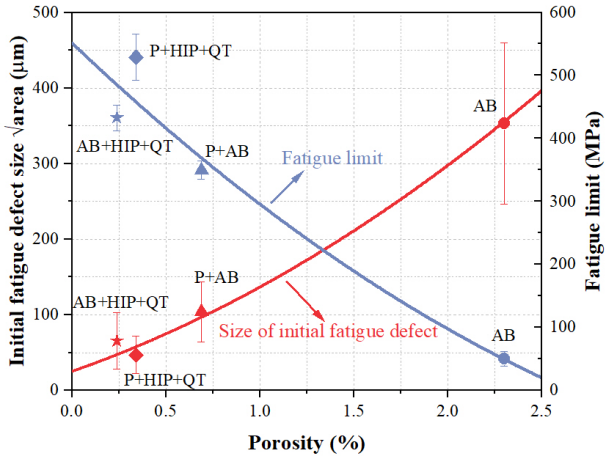

Figure 5.23: Influences of porosity in specimens on the initial fatigue defect sizes and fatigue limit [132].

However, it should be kept in mind that there is no strict relationship between the initial defect size and the final fatigue limit which can be simply concluded here because some specimens with a large initial defect size can still run out after 10^7 cycles. For example, there are two P+AB specimens with the defect size of 112.71 µm (P1) and 63.23 µm (P2), respectively, although the critical defect size of the P1 is about 1.78 times of the P2, both of them have survived after 10^7 cycles with the same stress amplitude, suggesting that the interplay between the defect size and fatigue limit should be further investigated.

5.6 Laser remelting

5.6.1 Microhardness and microstructure

The results of the microhardness tests are shown in Fig. 5.24. The last scanned layer of specimens has a mean microhardness value higher than 700 $HV_{0.1}$, primarily consists of fresh martensite. On the other hand, the average microhardness (excluding the last layer) of specimens without remelting is about 531.4 $HV_{0.1}$, which decreases by 6.8 % to 495 $HV_{0.1}$ after one remelting step (R1). The microhardness continues to decrease to 474.5 $HV_{0.1}$ after two remelting steps (R2), indicating that the remelting process and increasing

the number of remelting steps can increase the intrinsic tempering effect, resulting in a reduction of the microhardness.

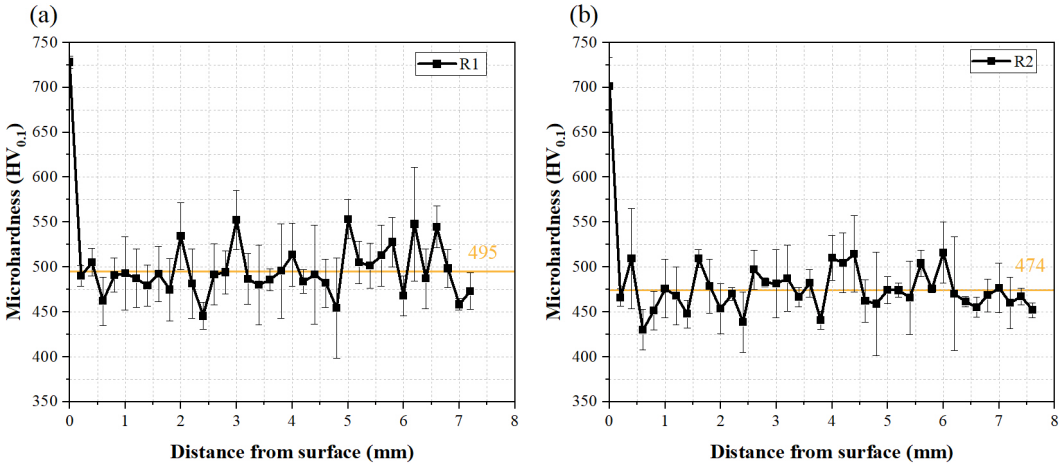

Figure 5.24: The microhardness depth profiles of specimens produced with different remelting steps. The parameters for the first melting (R0): P= 250 W, v= 1300 mm/s, h= 60 µm and t= 30 µm; The parameters for the remelting (R1 and R2): P= 200 W, v= 780 mm/s and h= 60 µm.

The morphology of specimens without and with laser remelting after etching is shown in Fig. 5.25. The microhardness of the white zone is found to be approximately 700 $HV_{0.1}$, which mainly consists of fresh martensite. The microhardness of the dark zones, on the other hand, is measured to be around 450-550 $HV_{0.1}$, and can be considered as tempered martensite, which is in agreement with the findings in [65].

From Fig. 5.25, it can be observed that the grey or dark zones in the microstructure of the R1 specimen (Fig. 5.25b) are much more pronounced than those in the specimen without laser remelting (Fig. 5.25a), suggesting that laser remelting has a beneficial tempering effect. This also explains the observed reduction in microhardness after laser remelting. Additionally, the boundaries of small melting pools disappear after laser remelting, which is advantageous in reducing defects in the vicinity of boundaries.

As aforementioned, microcracks were not inhibited and even increased with increasing remelting steps (Fig. 4.28). The fresh martensite zones have lower plasticity compared to the tempered martensite, because of high concentration of dislocations and supersaturated carbon [138]. The high density of dislocations in the fresh martensite is also responsible for its high microhardness, making it more susceptible to cracking than the tempered zones in the presence of tensile residual stresses.

5.6.2 Tensile properties

The tensile strain-stress curves of R0-R2 specimens manufactured in both the vertical and transverse directions are shown in Fig. 5.26, and their corresponding mechanical properties are listed in Table 5.1. The V-R1 and V-R2 specimens manufactured in the vertical direction show an improvement of 10.69 % and 8.62 %, respectively, in the ultimate

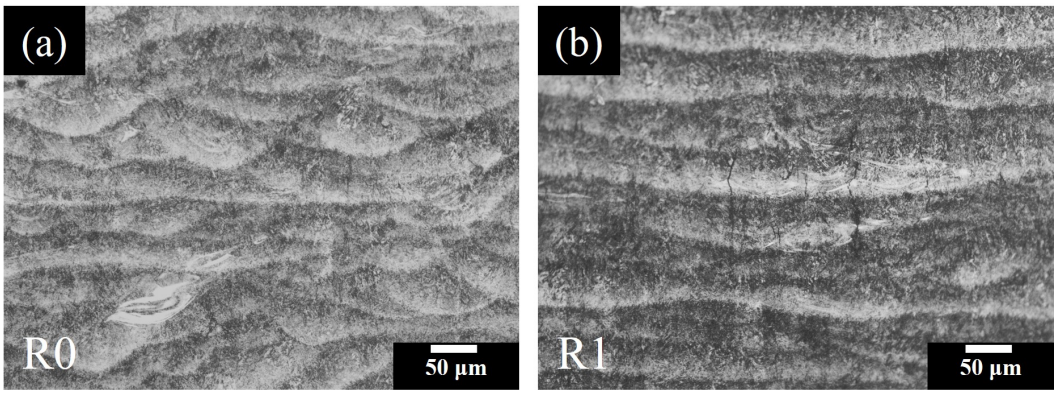

Figure 5.25: Microstructure of specimens (a) without laser remelting, R0 and (b) one-step laser remelting, R1. The parameters for the first melting (R0): P= 250 W, v= 1300 mm/s, h= 60 µm and t= 30 µm; The parameters for the remelting (R1 and R2): P= 200 W, v= 780 mm/s and h= 60 µm.

tensile strength (UTS), and 11.9 % and 9.8 %, respectively, in $YS_{0.2}$ compared to the V-R0 specimen, indicating that LR helps improving tensile strength. However, the elongation at fracture is not significantly changed with increasing the number of remelting steps.

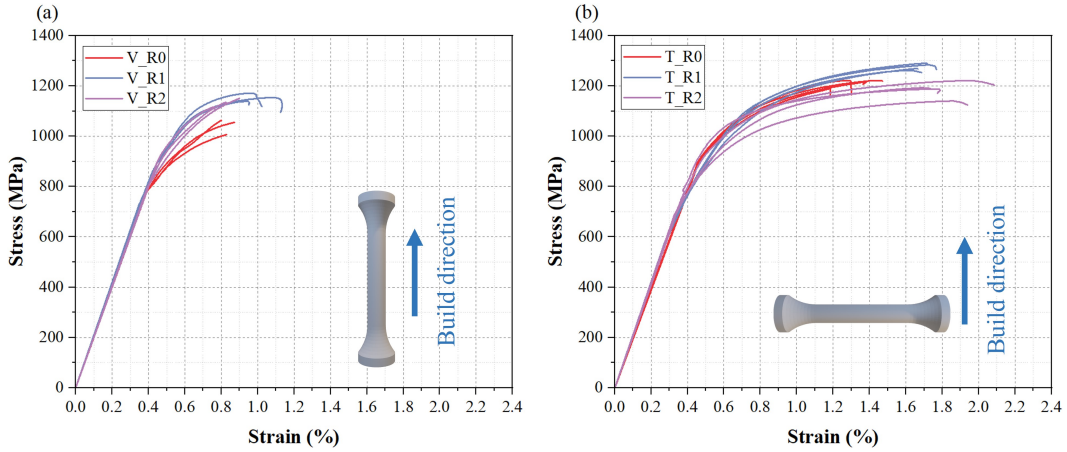

Figure 5.26: Stress-strain curves for PBF-LB specimens produced with three remelting steps and two building orientations [121]. (a) Vertical orientation and (b) transverse orientation.

Specimens produced with LR including R1 and R2 specimens, built in the transverse (T) direction, have higher UTS (increased by 10. 67 % and 5. 97 %, respectively) and elongation (increased by 140 % and 320 %, respectively) than the vertically (V) produced specimens, demonstrating the manufacturing orientation in PBF-LB also has a strong impact on the tensile strength of LR specimens. The T-R1 specimen has the highest tensile strength of 1276.9 MPa compared to specimens without remelting or with twice remelting (T-R0 and T-R2), suggesting that increasing remelting steps beyond once does not further improve the tensile strength.

Table 5.1: Mechanical properties of R0-R2 specimens built in the vertical (V) and transverse (T) orientation [121].

Specimens	UTS (MPa)	$YS_{0.2}$ (MPa)	A_f (%)
V-R0	1042.32±30.22	1001.85±26.72	0.31±0.04
V-R1	1153.78±16.23	1121.34±18.67	0.45±0.09
V-R2	1132.22±17.53	1100.89±13.38	0.30±0.03
T-R0	1217.8±3.2	1102.47±9.64	0.76±0.09
T-R1	1276.91±14.61	1115.64±10.28	1.08±0.03
T-R2	1199.83±17.74	1064.54±30.21	1.26±0.19

5.6.3 Discussion

5.6.3.1 Influence of laser remelting on tensile performance

The microhardness of the specimens decreases with increasing remelting steps, as shown in Fig. 5.24. Hence the yield strength of R1 is higher than that of R2 specimens. However, the $YS_{0.2}$ of the R1 and R2 specimens (vertical direction, for example) is about 10-12 % higher than R0. It could be explained by that there are more LoF flaws in the R0 specimen than in the R1 and R2 specimens resulting in local failure around the defects in R0 during the tensile test.

The fractography of the tensile specimens shown in Fig. 5.27 further demonstrates that LoF porosity is the main defect leading to low tensile properties in the R0 specimen (Fig. 5.27(a-b)), while cleavage fracture with secondary microcracks is the dominating fracture type in R1 and R2 specimens. Additionally, the fractography of R2 specimens show a greater presence of secondary microcracks than in R1 (Fig. 5.27(c-f)), which arise from microcracks. As a result, the high microhardness and the reduced number of microcracks in R1, contribute to higher tensile strength compared to R2.

It is worth noting that the UTS of the vertically oriented specimen (V-R0) increases by 10.69 % after once remelting (V-R1). However, simply switching the build direction from vertical to transverse (T-R0) results in a 16.8 % improvement in UTS, illustrating that the impact of the build orientation on UTS is greater than that of laser remelting in PBF-LB AISI 4140 specimens.

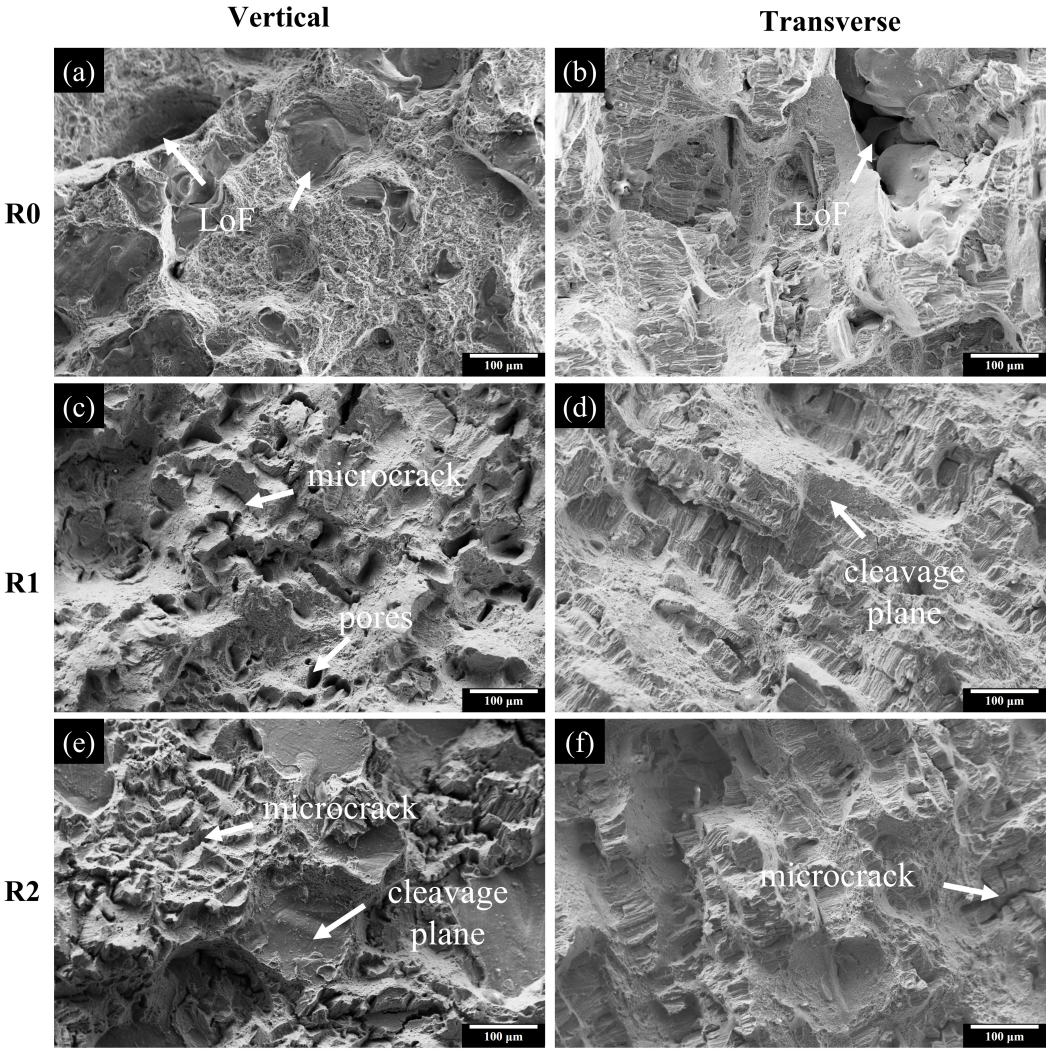

Figure 5.27: Fractography of R0-R2 specimens built in the (a) (c) (e) vertical and (b) (d) (f) transverse orientation after the tensile tests [121].

6. Fatigue limit prediction and validation

As mentioned in Chapter 5, the interplay between defect size and fatigue limit requires further investigation to deepen our understanding of the correlations among the sizes of initial fatigue defects, fatigue limits, and residual stress. Additionally, the fatigue mechanism of PBF-LB AISI 4140 has not been thoroughly investigated before. Therefore, the primary focus of this chapter is on studying the fatigue mechanism and identifying methods for predicting and validating the fatigue limit of AISI 4140 steels produced by PBF-LB.

6.1 Fatigue limit prediction

6.1.1 Background

It is widely known that a crack would not propagate if ΔK is smaller than the threshold ΔK_{th}. As noted previously, cracks in PBF-LB manufactured specimens typically originate from surface-connected LoF or keyhole pores. These defects caused by PBF-LB processing issues can be just handled as short cracks (< 1000 µm, sc) using the method proposed by Murakami [119]. Based on the theory of El-Haddad et al. [118], since $\Delta K_{th,sc}$ (Eq. 6.1-6.2) is smaller than $\Delta K_{th,lc}$ for long cracks (lc), short cracks could propagate below the $\Delta K_{th,lc}$ under certain situations.

$$\Delta K_{th,sc} = \Delta K_{th,lc} \times \sqrt{\frac{\sqrt{area}}{\sqrt{area} + \sqrt{area_0}}} \tag{6.1}$$

$$\sqrt{area_0} = \frac{1}{\pi} \cdot \left(\frac{\Delta K_{th,lc}}{Y \cdot \Delta \sigma_e} \right)^2 \tag{6.2}$$

Meanwhile, it is difficult for cracks to stop propagating when short cracks have already propagated into long cracks (1-2 mm) during the fatigue experiments, especially for brittle martensitic steels. Therefore, the conservative and safe condition for PBF-LB specimens with a high fatigue service life might be that cracks do not propagate from flaws in the microstructure. Due to the irregular shapes and sizes of defects for crack nucleation, it is necessary to figure out under which conditions cracks would not propagate from defects in PBF-LB specimens before 10^7 cycles.

Due to the plasticity at the crack tip, cracks will only reopen when the cyclic tensile stress is sufficiently high, which is known as the crack closure effect. Fatigue cracks can only propagate when the crack is fully open. If the stress intensity factor (SIF) for opening the crack is K_{op}, then the effective SIF range can be expressed as follows,

$$\Delta K_{eff} = K_{max} - K_{op} \tag{6.3}$$

The ΔK_{eff} can be expressed in Eq. 6.4 when considering the influence of residual stresses, which has been applied in Refs [139, 140]. It is assumed that, for the existing killer defects

in PBF-LB specimens, only the stress amplitude and the residual stress in the killer defect tips are directly considered.

$$\Delta K_{eff} = \ Y \cdot (\sigma_a + \ \sigma_{re}) \cdot \sqrt{\pi \cdot \sqrt{area}} \tag{6.4}$$

6.1.2 Two-parameter driving force model

The growth of cracks from the surface to a certain depth could be affected by the non-uniform residual stress depth profile [141]. To solve this question, Noorozi et al. [142] proposed a two-parameter driving force for crack growth analysis, wherein the residual stress was treated as mean stress superposed to external mechanical stress, as demonstrated by Eq. 6.5-6.10,

The fatigue crack driving force considering the mean stress effect can be expressed as follows Eq. 6.5-6.7,

$$\Delta K = K_{\max,tot}^{0.5} \Delta K_{tot}^{0.5} \tag{6.5}$$

$$K_{\max,tot} = K_{\max,appl} + K_{re} \tag{6.6}$$

$$\Delta K_{tot} = K_{\max,appl} - \frac{3}{2Y}\sqrt{\frac{\rho*}{\sqrt{area}}} K_{\min,appl} + K_{re} \tag{6.7}$$

The residual stress intensity factor K_{re} was calculated by integrating the residual stress $\sigma_{re}(x)$ and the weight function m(x,$\sqrt{area}$), as shown in Eq. 6.8-6.10.

$$K_{re} = \int_0^{\sqrt{area}} \sigma_{re}(x) \cdot m(x, \sqrt{area}) dx \tag{6.8}$$

$$m(x, \sqrt{area}) = \frac{2p}{\sqrt{2\pi(\sqrt{area} - x)}} M \tag{6.9}$$

$$M = 1 + M_1(1 - \frac{x}{\sqrt{area}})^{0.5} + M_2(1 - \frac{x}{\sqrt{area}}) + M_3(1 - \frac{x}{\sqrt{area}})^{1.5} \tag{6.10}$$

where $\sigma_{re}(x)$ is the residual stress depth profile, m(x, $\sqrt{area}$) is the universal weight function, and the calculation of geometry dependent factors M_1, M_2 and M_3 can be found in [143]. The parameters relevant to this study are provided in Table 6.1 and are extracted from the literature [144].

Table 6.1: Parameters used in the fatigue limit prediction

$Y_{surf.}$	$Y_{subsurf.}$	$\sqrt{area_0}$ (µm)	$\Delta K_{th,lc}$ (MPa·$\sqrt{m}$)	$\Delta\sigma_e$ (MPa)	ρ^* (m)	p
0.65	0.5	180.03	8.5	550	1.15×10^{-5}	0.5

Table 6.2: Defect size and SIF ranges of PBF-LB specimens [132]

Series	σ_a (MPa)	$\sqrt{area}$ (µm)	$\Delta K_{\text{Empirical}}$ (MPa·$\sqrt{\text{m}}$)	$\Delta K_{\text{two-parameter}}$ (MPa·$\sqrt{\text{m}}$)	$\Delta K_{\text{th,sc}}$ (MPa·$\sqrt{\text{m}}$)
AB	50	263.31	5.30	5.87	6.55
	50	247.88	5.14	5.66	6.47
	50	366.23	6.25	7.20	6.96
	100	469.15	8.32	9.90	7.23
	100	335.60	7.03	8.09	6.86
	125	309.88	7.27	8.33	6.76
	150	363.16	8.42	9.78	6.95
	150	568.20	10.53	12.75	7.41
P+AB	325	62.67	3.15	3.25	4.32
	350	112.71	4.63	5.04	5.27
	350	63.23	3.42	3.60	4.33
	375	155.63	5.82	6.43	5.79
	400	168.96	6.33	7.17	5.91
	400	93.52	4.84	5.29	4.97
	425	97.98	5.11	5.81	5.05
	450	79.96	4.87	5.56	4.71
AB_HIP+QT	400	34.84	2.12	3.09	3.42
	400	38.02	2.21	3.25	3.55
	425	85.57	4.84	5.46	4.82
	450	125.36	5.80	7.01	5.45
	450	41.76	2.52	3.10	3.69
	475	36.48	3.51	3.96	3.49
	500	27.14	3.11	3.62	3.08
	500	77.46	5.07	6.22	4.66
P+AB_HIP+QT	525	37.64	3.50	3.29	3.53
	550	23.88	2.95	2.72	2.91
	550	14.76	2.32	2.09	2.34
	575	61.23	4.96	4.84	4.28
	575	50.63	4.51	4.39	3.98
	600	92.68	6.38	6.25	4.96
	650	36.12	4.33	4.32	3.47
	650	58.48	5.51	5.50	4.21

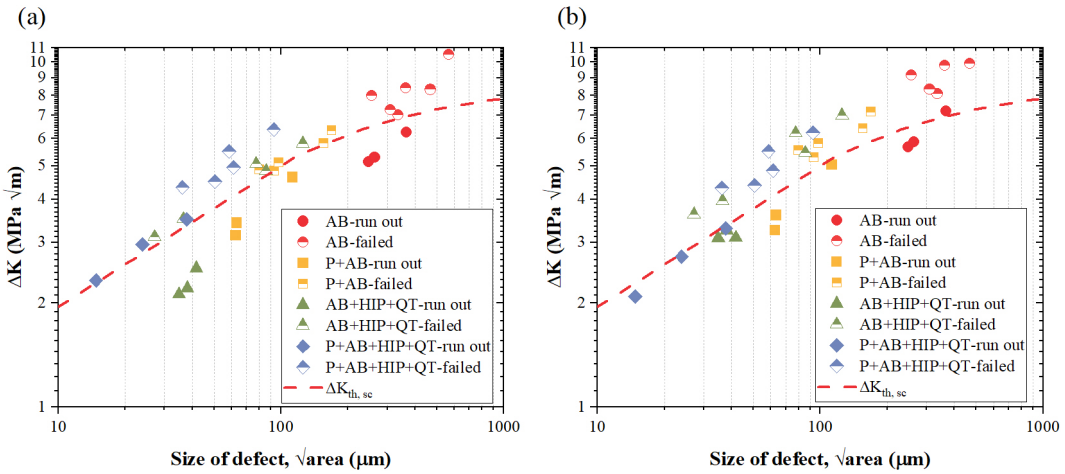

Figure 6.1: The comparison of two models (a) simplified empirical method and (b) two-parameter driving force model to predict run out and failed specimens during the fatigue testing according to various defect sizes [132].

6.1.3 The relationship between killer defect size and SIF range

Based on the interplay between defect sizes $\sqrt{area}$, ΔK and $\Delta K_{th,sc}$ as depicted in Fig. 6.1, these two adopted methods including simplified empirical method and two-parameter driving force method confirmed that all specimens with different defect sizes and stress amplitudes are going to fail before 10^7 when $\Delta K \geq \Delta K_{th,sc}$, whereas specimens tend to run out when $\Delta K < \Delta K_{th,sc}$.

Moreover, it is found that the two-parameter driving force model (Fig. 6.1b, also see Table 6.2) divides the failed and run out specimens much more accurately compared to the simplified empirical method (Fig. 6.1a). The main issue with the empirical method is that it is difficult to determine the run out and failed specimens in the vicinity of the threshold line. However, it still can be understood that the probability of specimens not failing during the rotating bending fatigue test is increased when the condition $\Delta K < \Delta K_{th,sc}$ is met. Consequently, it is reasonable to assume that there should be a theoretical value for the allowable threshold defect size when $\Delta K = \Delta K_{th,sc}$, and it can be rewritten based on Eq. 6.4 as follows,

$$\sqrt{area_{th}} = \frac{1}{\pi} \cdot \left(\frac{\Delta K_{th,sc}}{Y \cdot (\sigma_a + \sigma_{rs})} \right)^2 \tag{6.11}$$

6.1.4 Threshold defect size

The correlations among stress amplitude, the allowable threshold defect size and residual stress can be explained according to Eq. 6.11. As shown in Fig. 6.2, the threshold defect size $\sqrt{area_{th}}$ decreases as the stress amplitude increases with a specific residual stress value. Furthermore, the $\sqrt{area_{th}}$ increases with the increase of compressive residual stress, whereas it is anticipated to decrease as tensile residual stress increases. Consequently, compressive residual stress is beneficial to increase $\sqrt{area_{th}}$, and thus to increase the fatigue limit.

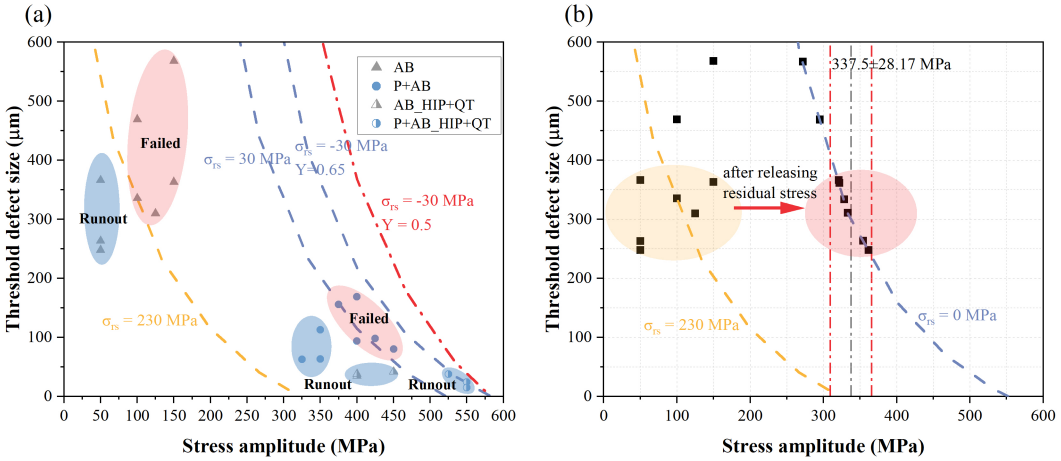

Figure 6.2: (a) The correlations among stress amplitude, threshold defect size and the residual stress in defect tips [132], and (b) The experimental prediction of fatigue limit of PBF-LB specimens with plenty of LoF pores.

According to Eq. 6.11, the threshold defect size for AB specimens to run out at 50 MPa is about 536 µm, while the value is up to 400 µm for P+AB specimens to run out at 350 MPa. Additionally, the threshold defect size could be around 300 µm for both AB and P+AB specimens to run out at 350 MPa when the residual stress in the killer defect tips is zero. Furthermore, the majority of experimental data for run out specimens are below the calculated threshold defect size, and failed specimens are above the threshold line, indicating that the method is effective in predicting the fatigue limit of samples produced by PBF-LB.

It is evident that the shape factor Y also influences the potential threshold defect size according to Eq. 6.11, and the result again fits well with the curve in Fig. 6.2 for defects underneath the surface with the same residual stress level (red dash-dot line). As a result, killer defects in P+AB specimens following HIP+QT can be interpreted as subsurface pores with a smaller shape factor (Y=0.5) than surface defects (Y=0.65). Regarding a surface-connected defect $\sqrt{area_{th1}}$ and a subsurface defect $\sqrt{area_{th2}}$, $\sqrt{area_{th2}} \approx 1.69\sqrt{area_{th1}}$ when they attain the same $\Delta K_{th,sc}$, suggesting subsurface defects have a larger threshold defect size than defects connected to the surface. Additionally, it also explains why most of the crack initiation flaws in PBF-LB specimens are located on the surface.

The correlations shown in Fig. 6.2 also suggest a potential approach to improve the fatigue limit even with significant defects (200-500 µm, LoF), simply by reducing tensile residual stresses from 230 MPa to 0 MPa in specimens. In this chapter, three methods including tempering, deep rolling (DR) and laser remelting (LR) are investigated to evaluate their effectiveness in enhancing the fatigue limit of PBF-LB AISI 4140 steel.

6.2 Validation and other methods

6.2.1 Heat treatment

To validate the correlations, additional machined as-built specimens (AB) are quenched and tempered at 450 °C for 2 hours to release residual tensile stress. The residual stresses distribution and the S-N curve for AB + QT 450 °C are shown in Fig. 6.3. It can be found that the residual stresses in the AB specimen are nearly released (Fig. 6.3a), and the fatigue limit increases from 50 MPa to 337.5 MPa (Fig. 6.3b), which is close to the fatigue limit of P+AB (350 MPa).

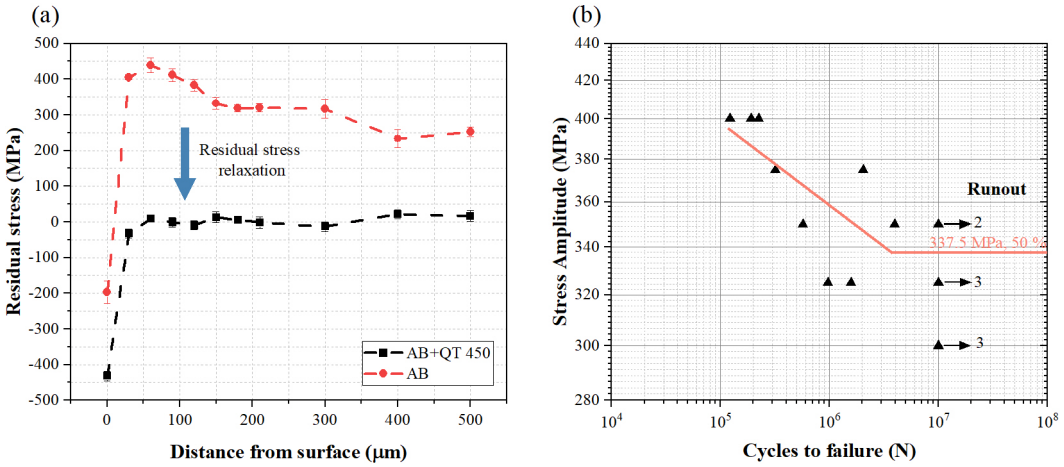

Figure 6.3: (a) The relaxation of residual stresses in the AB sample by tempering at 450 °C, and (b) the S-N curve for tempered AB specimens [132].

6.2.2 Laser remelting

As shown in Fig. 6.4a, the high cycle fatigue limit of the R1 specimen manufactured in the vertical direction is 72.5 MPa, which is a 45 % increase compared to the as-built specimens without remelting (AB/R0, 50 MPa) as reported in chapter 5.

However, this fatigue limit of R1 is still only a fraction (about 3 times lower) of the desirable fatigue limit of AISI 4140 manufactured by PBF-LB with preheating (350 MPa), indicating that the only improvement in relative density from 99.3 % to 99.6 % by LR does not have a significant influence on improving the fatigue limit. It is interesting to note that the fatigue limit of the R1 specimen built in the transverse direction is 200 MPa, which increases by 176 % compared to the V-R1 specimen, as shown in Fig. 6.4b. This indicates that the building orientation in PBF-LB influences the fatigue behavior of materials more significantly than laser remelting.

The residual stress depth profiles in the XY and XZ planes, measured experimentally from the surface to a maximum depth of 500 µm (as shown in Fig. 6.5), reveal that the specimen manufactured with LR has lower residual stress compared to the specimen without remelting in both two planes.

In the XZ plane (Fig. 6.5a), the residual stress on the surface is the lowest, with values of about 240 MPa and 89 MPa for the R0 and R1 specimens, respectively. The residual

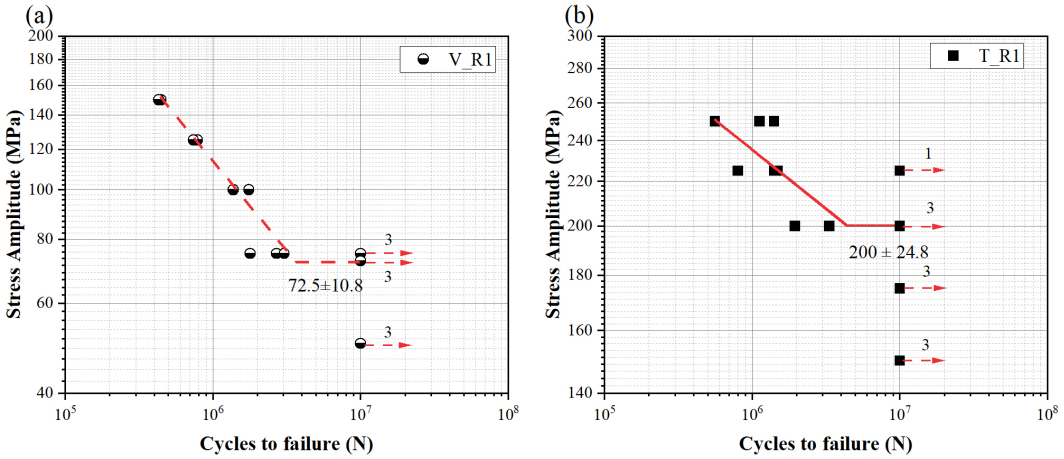

Figure 6.4: High cycle fatigue S-N curves of PBF-LB specimens produced with laser remelting (R1) in (a) vertical direction and (b) transverse direction.

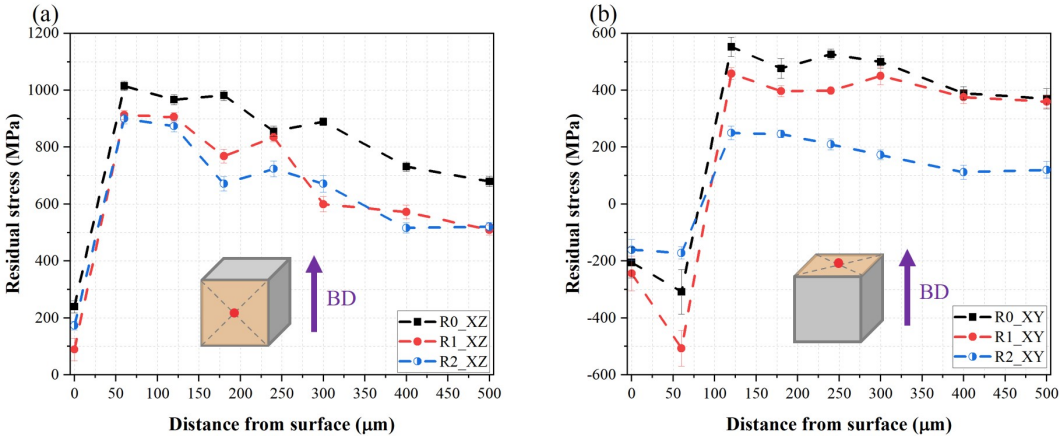

Figure 6.5: The residual stress depth profiles of R0, R1 and R2 specimens measured from the center of the surface to 500 µm in depth [121].

stress then sharply increases to a peak, reaching 913 MPa and 1015 MPa for the R0 and R1 specimens, respectively, when the depth reaches 60 µm. However, the residual stress shows a decreasing trend with further increasing depth from 60 µm to 500 µm. In the XY plane (Fig. 6.5b), which is perpendicular to the building orientation, the surface residual stress is compressive and the maximum compressive residual stress occurring at a depth of about 60 µm, with values of -308 MPa and -506 MPa for the R0 and R1, respectively. However, the compressive residual stress changes to a tensile state with increasing depth from 120 µm to 500 µm and shows a similar declining trend as seen in the XZ plane. The residual stress of the R2 specimen in the XZ plane is slightly lower compared to the R1 specimen, but it drops by about 50 % in the XY plane.

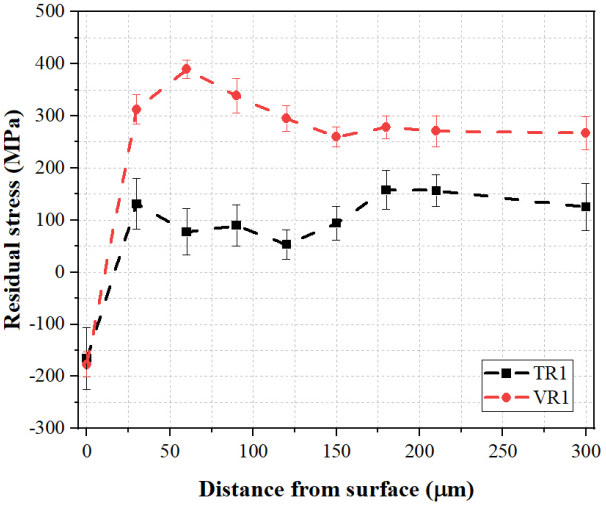

Figure 6.6: The residual stresses depth profiles of fatigue specimens built with laser remelting in the vertical and transverse directions.

The depth profiles of residual stresses in fatigue specimens manufactured with laser remelting in the vertical and horizontal directions are shown in Fig. 6.6. The residual stresses in the fatigue specimen built in the vertical direction exhibit only a marginal decrease compared to fatigue specimens without laser remelting (Fig. 6.3a, AB). This suggests that laser remelting does not prominently relieve the residual stresses distributed along the building orientation in fatigue specimens, aligning with results presented in Fig. 6.5a. However, a significant drop of over 100 MPa in residual stresses occurs when the fatigue specimen is built in the transverse direction.

6.2.3 Deep rolling

Deep rolling (DR) is an effective method of applying compressive residual stresses on the surface of components to inhibit crack propagation, and it can be done during the machining process. In order to further investigate the influence of residual stresses on the fatigue limit and to have a comparison with that treated with HIP, deep rolling is applied and investigated in this section. In previous experiments, it was found that 99.9 % of specimens can run out of 10^7 when the number of cycles surpasses 5×10^6, so 5×10^6 can be set as the threshold instead of 10^7 to improve the testing efficiency.

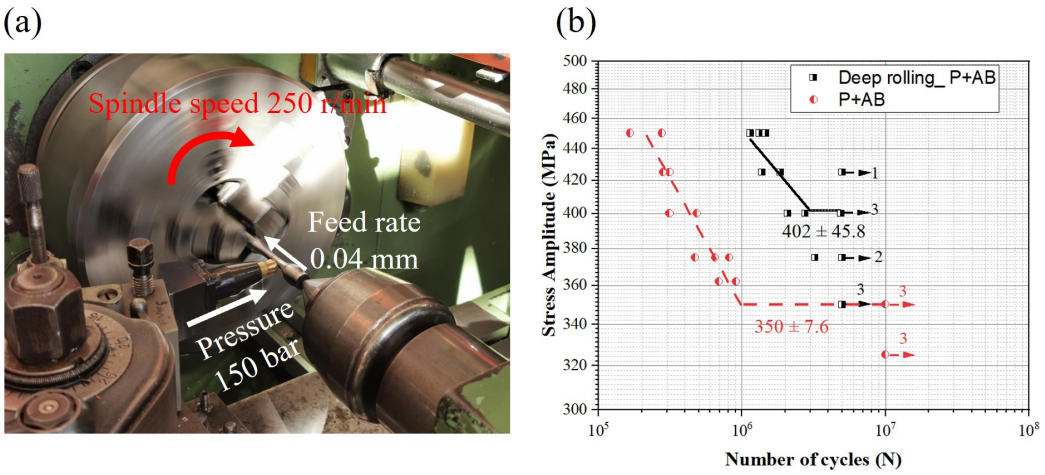

Figure 6.7: (a) The process of deep rolling and (b) the fatigue S-N curve of P+AB specimen following the deep rolling process.

As shown in Fig. 6.7, the fatigue limit of the P+AB specimen following the DR is about 402 MPa, which increases by 15 % compared to that without DR (350 MPa). Moreover, DR also increases the number of cycles for specimens tested under high stress amplitudes. For example, the number of cycles increase from 275100 at 450 MPa to beyond 10^6 at the same stress amplitude level, with an increase of more than 300 %, indicating DR is efficient in increasing fatigue life in the high cycle fatigue (HCF) regime. However, the fatigue limit of the P+AB specimen treated with DR is still about 24 % lower than that treated with HIP.

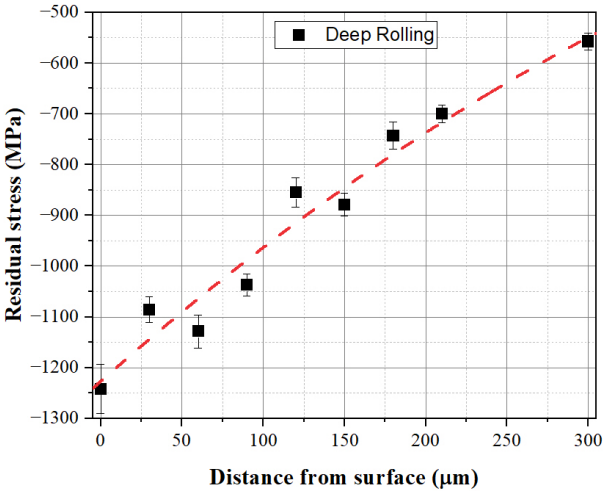

Figure 6.8: Residual stresses depth profile of the P+AB specimen treated with deep rolling.

In terms of residual stresses, as shown in Fig. 6.8, the residual stresses are compressive, and the maximum value is about -1240 MPa on the surface following the deep rolling treatment. The distribution of compressive residual stresses from the surface to a depth of 300 μm exhibits a fluctuating decreasing trend from -1240 MPa to -550 MPa, which can be attributed to the decreased effect of plastic deformation by DR along the depth.

6.3 Discussion

6.3.1 Influence of heat treatment on fatigue limit

The fatigue fractography of the AB + QT 450 sample shows that the LoF defect with similar defect size (200-300 µm) as that in the AB samples is still the dominant killer defect for crack initiation (as shown in Fig. 6.9), indicating the residual stresses have a more significant effect on the fatigue limit of PBF-LB AISI 4140 specimens than defect size itself. In addition, it also confirmed the validity of the correlations proposed, as shown in Fig. 6.2b. As a consequence, reliefing residual stresses in specimens can effectively enhance the fatigue limit of AISI 4140 steel manufactured by PBF-LB.

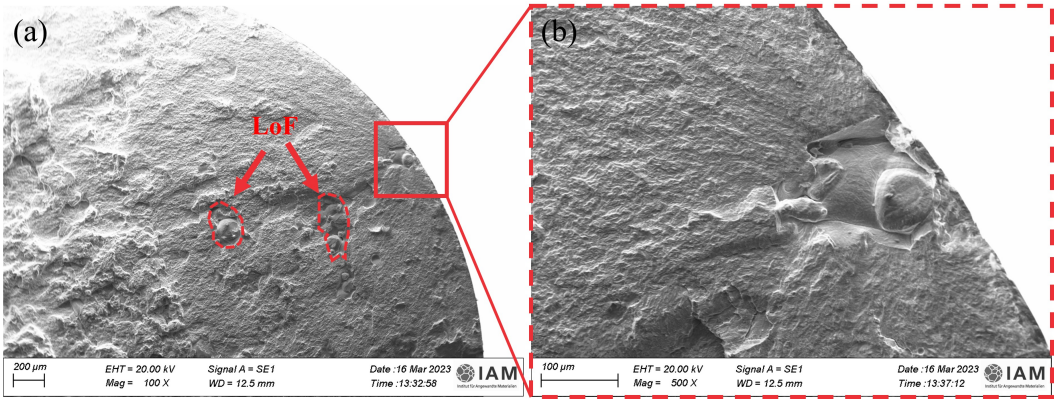

Figure 6.9: The fatigue fratography of AB+QT 450 °C specimen.

6.3.2 Influence of laser remelting on fatigue limit

As aforementioned, the fatigue limit of the LR specimens (R1) is only 20-24 % of the fatigue limit of the AISI 4140 steel produced through PBF-LB without laser remelting (R0, with preheating) which has been discussed in Chapter 5. The type of defects for crack nucleation in the R1 specimens is the keyhole porosity with a mean size $\sqrt{area}$ of about 54 µm (Fig. 6.10), which is only around 13.5 % of the killer defect size in R0. As the RD of the specimens increases to a maximum value of 99.6 % by implementing LR, some potential killer defects for crack propagation are eliminated by LR, thereby increasing the fatigue limit compared to the specimen produced without remelting but under similar manufacturing conditions [121].

However, the fatigue limit of PBF-LB specimens is not only influenced by porosity but also by residual stresses present around defect tips. Furthermore, residual stresses have a stronger effect on the killer defect in fatigue strength compared to the size of the defect. Despite the reduction of defect size after LR (54 µm) and the distance from surface to the front tip of killer defects (about 70 µm), the residual stresses do not prominently decline. The mean residual stresses in front of killer defects in machined R1 is about 400 MPa (see Fig. 6.6), which can be regarded as the dominanting reason for the low fatigue limit of the LR specimens compared to P+AB specimens, despite the high relative density (99.6 %). Additionally, apart from the defect direction, the higher fatigue limit of the transversely

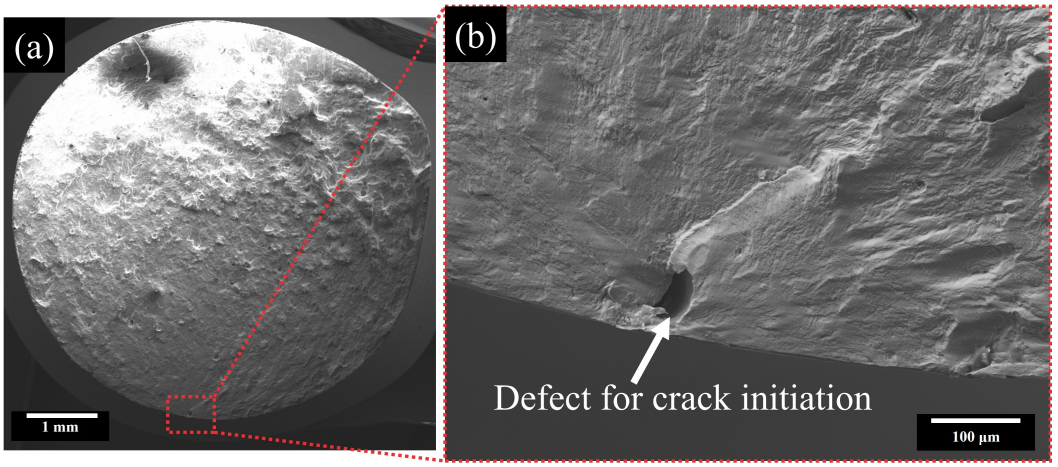

Figure 6.10: The fatigue fractography of R1 tested under 150 MPa, showing the killer defect size and location [121].

built specimen compared to the vertically built specimen can also be attributed to the lower tensile residual stresses in the transversely built specimen.

The increased microcrack density in the R1 specimens should be another reason for the low fatigue limit. However, the crack density in R1 increases by about 37 % compared to R0, but the fatigue limit does not further decrease. This can be explained by the fact that the length of the microcracks measured from metallographic images, with an average value of 35 µm, is far below the threshold for the short crack to propagate, 65 µm, according to the El-Haddad model (Eq. 6.1-6.2) [118] at a low stress amplitude of 72.5 MPa. Consequently, the impact of microcracks on the fatigue limit of R1 is negligible when applying low stress amplitudes.

6.3.3 Influence of deep rolling on fatigue limit

The fractography of P+AB samples after DR treatment (Fig. 6.11) shows that the location of the initial fatigue defect, with a defect length $\sqrt{area}$ of 70-120 µm, is shifted from a mean value of 120 µm underneath the surface in P+AB specimens far away from the surface to about 400-600 µm. Consequently, the high compressive residual stresses due to deep rolling force the pores in the vicinity of the surface to be enclosed, which could be the dominant reason for the improved fatigue limit.

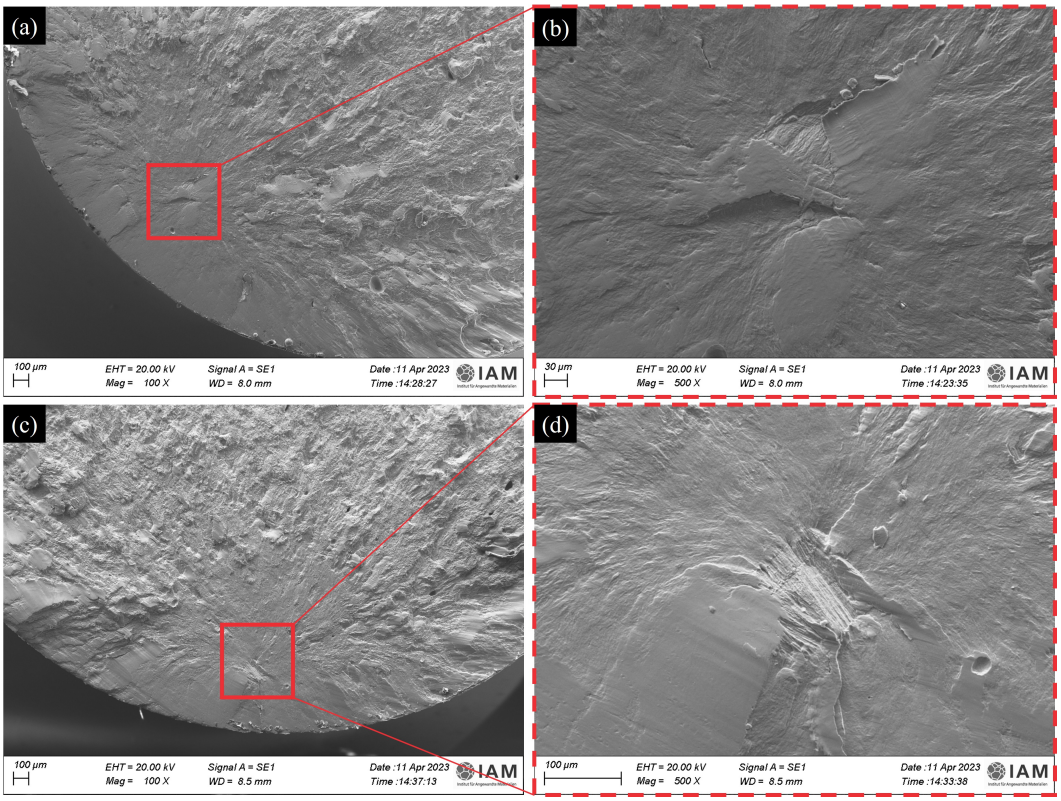

Figure 6.11: The fractography of P+AB specimen following the deep rolling process shows the location of initial fatigue defects. Specimens (a) and (c) survived at the stress amplitude of 400 MPa ($> 10^7$ cycles) and then broke at 450 MPa. (b) and (d) show the magnified killer fatigue defects.

7. Conclusion and outlook

7.1 Conclusion

This thesis systematically investigated the correlations among the process parameters, defects, and mechanical properties of AISI 4140 steel fabricated by Powder Bed Fusion-Laser Beam, as well as the effects of heat treatment including Q&T and HIP on relative density and mechanical properties. The main conclusions of this study are shown as follows.

In the single-track PBF-LB experiments, the width of the single-track melt pool is mainly influenced by the laser scanning speed and decreases with the increase of scanning speed. The increase of scanning speed also reduces the depth of the melt pool. There is a positive linear correlation between the laser power and the melt pool depth, i.e., the depth increases with the increase of laser power, but the effect of laser power on the width of the single-track can be neglected when applying high scanning speed (1300 mm/s). Microcracks appear on the single track due to the high linear energy density when the laser scanning speed is $\leq$ 500 mm/s.

In the multi-layer PBF-LB experiments, it is found that with a laser power of P = 250 W, a laser scanning speed of v = 1300 mm/s, a hatching distance of h = 60 µm and a powder layer thickness of t = 30 µm, the relative density can reach up to 99 %. Increasing laser power significantly reduces the amount of lack of fusion defects. Meanwhile, increasing scanning speed reduces not only the formation of keyholes, but also increases the probability of LoF defects. The effect of hatching distance on the relative density is smaller than the effect of laser power.

Increasing laser power increases the crack density, while increasing laser scanning speed reduces the crack density. However, when the scanning speed exceeds 900 mm/s, the crack density does not decrease significantly. There is no significant correlation between volumetric energy density and relative density, but crack density increases with improving volumetric energy density. Although the improvement in relative density due to substrate preheating is not significant, the crack density is reduced by about 95 % compared to as-built specimens, which could be explained by the fact that substrate preheating reduces the temperature gradient, thus reducing the formation of microcracks.

Increasing laser power could increase the lateral surface roughness, while increasing the scanning speed is beneficial for reducing the lateral surface roughness. Compared to the 45° building direction, specimens manufactured in the vertical (90°) and horizontal (0°) directions have lower surface roughness values on the top surface. Increasing the thickness of the powder layer is beneficial for reducing the roughness value on the lateral surface, but it could increase the roughness value on the top surface. Additionally, specimens produced in the horizontal direction have the highest lateral surface roughness values for all powder layer thicknesses within this work. Specimens manufactured in the vertical direction have a higher quality on both the top and lateral surfaces than those manufactured in the horizontal direction.

Hot isostatic pressing is an efficient method for significantly reducing the size, number and sphericity of defects in additively manufactured samples. However, the closure efficiency of hot isostatic pressing could be affected by unmelted powder particles, stress relaxation effects during subsequent heat treatment, and trapped argon gas.

With regard to microhardness, increasing laser power or decreasing scanning speed could both result in a decrease in microhardness, due to the enhanced intrinsic tempering effect caused by the increase of input energy density. Additionally, the preheating of the substrate also has an effect on reducing the microhardness.

Compared to keyholes and gas pores, LoF defects have the greatest impact on tensile strength, mainly because LoF defects are easier to induce crack propagation. Since LoF defects are mainly controlled by laser power, the tensile strength of AISI 4140 is more affected by laser power than by laser scanning speed. Samples produced horizontally exhibit better tensile properties than those produced vertically. Due to preheating, the crack density and porosity of the samples are lower and the hardness is also reduced, leading to improved ductility. Therefore, samples manufactured horizontally with preheating have the highest tensile properties.

The highest Charpy impact energy of PBF-LB specimen is only around 50 % of the conventionally manufactured specimen. As-built specimens AB have the lowest impact energy, about 5.7 J, and the common tempering heat treatment has no significant influence on improving the impact energy of the AB state. The impact energy of the P+AB specimen is about 3 times higher than that of AB, which can be attributed to different fracture mechanisms of AB and P+AB, brittle and ductile, respectively. The Charpy impact energy drops dramatically with increasing porosity, and the impact energy does not vary much after porosity exceeds 2 %.

The surface residual stress of the unmachined AB specimen is about 200 MPa, and its maximum internal stress can exceed 950 MPa. After machining, the surface residual stress becomes compressive, about -200 MPa, but beyond a depth of 30 microns, it will turn into high tensile residual stress with an average value of 341 MPa. Preheating of the substrate can effectively release the residual stress generated during the manufacturing process, with an average value of 15.7 MPa. After the hot isostatic pressing (HIP) and subsequent quenching and tempering (QT) heat treatment, the residual tensile stress is released in the samples. The average residual stress for AB+HIP+QT specimens is 7.7 MPa, but for P+AB+HIP+QT specimens, the average stress is -43 MPa, indicating that the initial residual stress state in AB and P+AB specimens could have an impact on the residual stress in subsequent hot isostatic pressing.

The fatigue limit of the AB samples is only 50 MPa, which is 14.3 % of the P+AB specimens (350 MPa). However, after being treated with hot isostatic pressing, the fatigue limits of AB and P+AB specimens increase by 766 % and 51 %, respectively, which are comparable to specimens produced by traditional methods. An increase in porosity leads to an increase in the average size of killer defects, which in turn reduces the fatigue limit. However, within a certain range, the defect size does not affect the fatigue limit. Once the defect size exceeds

a threshold which is determined by stress amplitude and residual stress, the specimen tends to fail prematurely. After releasing the residual stress in AB, the fatigue limit increases to 337 MPa, indicating that the residual stress at the tip of the killer defects has a greater impact on the fatigue limit than the defect size itself. Additionally, compressive residual stress and defects far from the surface are helpful in improving the tolerance of the defect for crack propagation. Hence, it is possible to manufacture specimens by PBF-LB with defects in a certain range that do only marginally affect the desired fatigue strength.

Laser remelting can significantly increase the relative density, reaching a maximum value of 99. 6 %, but the processing parameters of the remelting also need to be optimised. Laser remelting is beneficial for reducing the top surface roughness with increasing the number of remelting steps. However, surface roughness on lateral surfaces increases with increasing the number of remelting steps due to the increased and irregular width of tracks and adhering particles. Although the increased remelting steps are helpful in reducing residual stress, the samples are still in the tensile state. Moreover, the increased crack density with an increase of remelting steps could be one mechanism releasing residual stresses.

The tensile properties of specimens produced with one remelting step are the highest, and further increasing the number of remelting steps cannot further increase the tensile properties. The fatigue limit of specimens manufactured with one remelting step is about 72.5 MPa, which is a 45 % increase compared to AB specimen. Although the microcrack density in the R1 specimen improves by 37 % compared to the AB specimens, the length of the microcracks, 35 µm, is much lower than the length threshold for the propagation of short cracks (65 µm). The low fatigue limit of R1 specimens compared to P+AB (350 MPa) could be ascribed to high residual stress in defect tips, around 400 MPa.

7.2 Outlook

In this thesis, samples with substrate preheating were manufactured on a different PBF-LB device due to the experiment conditions. However, a comprehensive study of the complete process window for samples with substrate preheating was not conducted in this research. Therefore, it is recommended that future work focuses on comparing the process windows of samples manufactured with and without preheating. This comparison will provide a deeper understanding of the role of substrate preheating in the PBF-LB process.

The fatigue study of AISI 4140 steel manufactured by PBF-LB combines theoretical knowledge from the literature with experimental verification. Residual stress has a significant impact on the fatigue limit of PBF-LB samples. However, the overall distribution of residual stresses in fatigue specimens before and after fatigue testing remain unclear. Therefore, future research should utilize finite element software, based on existing experimental data, to simulate the distribution of residual stress in specimens after PBF-LB. The simulation results can be further coupled with fatigue analysis software to predict fatigue life of PBF-LB parts. Moreover, the presence of defects such as pores and cracks in PBF-LB specimens presents challenges in reliably measuring crack growth rates using experimental methods, and only refer to the data from conventionally manufactured counterparts.

Future research could also employ finite element simulations to validate relevant data and compare them with experimental results.

Deep rolling is an effective process for improving the fatigue life of components by introducing higher residual compressive stress to close pores on the surface or subsurface. However, it is not necessarily the case that higher residual compressive stress is more beneficial for improving the fatigue limit. Its effectiveness in enhancing the fatigue limit is not superior to that of other methods, such as hot isostatic pressing. Therefore, further analysis and research are needed to better understand the relevant mechanisms. In addition, for larger porosity rates, the impact of deep rolling on fatigue should also be further investigated.

Although this thesis presents detailed experimental work on AISI 4140 steels produced by Powder Bed Fusion-Laser Beam, it can be seen that the parameter optimization process is troublesome and requires a large number of specimens for experimentation. With the deepening development of technologies such as artificial intelligence and machine learning, it is a potential trend to integrate artificial intelligence and machine learning into the research of processing parameters optimization for Powder Bed Fusion-Laser Beam. Machine learning and artificial intelligence can help solve problems such as low efficiency of manual processing optimization and unstable product quality in Powder Bed Fusion-Laser Beam. By using a large amount of data and algorithms, machine learning can automatically adjust the parameters in the Powder Bed Fusion-Laser Beam process to obtain parts with the highest relative density. For example, machine learning algorithms can be used to automatically adjust the position and intensity of the laser beam to ensure that each layer of powder is completely melted and to avoid structural defects or deformations.

It is worth mentioning that the recycling of powders in PBF-LB is currently based on manual or semi-automatic sieving processes. During this process, the powder may come into contact with moist air, necessitating additional drying treatments. Moreover, there are safety concerns. In the future, achieving a fully closed-loop system encompassing automatic powder recycling, sieving, and refilling into the powder reservoir for additive manufacturing will significantly enhance the efficiency of powder bed fusion processes.

Bibliography

[1] M.H. Khani Sanij, S.S. Ghasemi Banadkouki, A.R. Mashreghi, et al. "The effect of single and double quenching and tempering heat treatments on the microstructure and mechanical properties of AISI 4140 steel". In: *Materials & Design* 42 (2012), pp. 339–346. DOI: https://doi.org/10.1016/j.matdes.2012.06.017.

[2] V. Schulze. "Procedures of Mechanical Surface Treatments". In: *Modern Mechanical Surface Treatment*. Weinheim: Wiley-VCH Verlag GmbH & Co. KGaA, 2005. Chap. 2, pp. 9–24. ISBN: 9783527607815. DOI: https://doi.org/10.1002/3527607811.ch2.

[3] A.H. Meysami, R. Ghasemzadeh, S.H. Seyedein, et al. "An investigation on the microstructure and mechanical properties of direct-quenched and tempered AISI 4140 steel". In: *Materials & Design* 31.3 (2010), pp. 1570–1575. DOI: https://doi.org/10.1016/j.matdes.2009.09.040.

[4] N. Haghdadi, M. Laleh, M. Moyle, et al. "Additive manufacturing of steels: a review of achievements and challenges". In: *Journal of Materials Science* 56 (2021), pp. 64–107. DOI: https://doi.org/10.1007/s10853-020-05109-0.

[5] D. Herzog, V. Seyda, E. Wycisk, et al. "Additive manufacturing of metals". In: *Acta Materialia* 117 (2016), pp. 371–392. DOI: https://doi.org/10.1016/j.actamat.2016.07.019.

[6] N. Li, S. Huang, G. Zhang, et al. "Progress in additive manufacturing on new materials: A review". In: *Journal of Materials Science & Technology* 35.2 (2019), pp. 242–269. DOI: https://doi.org/10.1016/j.jmst.2018.09.002.

[7] T. Fedina, J. Sundqvist, J. Powell, et al. "A comparative study of water and gas atomized low alloy steel powders for additive manufacturing". In: *Additive Manufacturing* 36 (2020), p. 101675. DOI: https://doi.org/10.1016/j.addma.2020.101675.

[8] R. Dörfert, J. Zhang, B. Clausen, et al. "Comparison of the fatigue strength between additively and conventionally fabricated tool steel 1.2344". In: *Additive Manufacturing* 27 (2019), pp. 217–223. DOI: https://doi.org/10.1016/j.addma.2019.01.010.

[9] P. Bajaj, A. Hariharan, A. Kini, et al. "Steels in additive manufacturing: A review of their microstructure and properties". In: *Materials Science and Engineering: A* 772 (2020), p. 138633. DOI: https://doi.org/10.1016/j.msea.2019.138633.

[10] R. Molaei, A. Fatemi, and N. Phan. "Significance of hot isostatic pressing (HIP) on multiaxial deformation and fatigue behaviors of additive manufactured Ti-6Al-4V including build orientation and surface roughness effects". In: *International Journal of Fatigue* 117 (2018), pp. 352–370. DOI: https://doi.org/10.1016/j.ijfatigue.2018.07.035.

[11] J. Damon, S. Czink, P. Schüßler, et al. "Mechanical surface treatment of EBM Ti6Al4V components: Effects of the resulting surface layer state on fatigue mechanisms and service life". In: *Materials Science and Engineering: A* 849 (2022), p. 143422. DOI: https://doi.org/10.1016/j.msea.2022.143422.

[12] C. Hull. "Apparatus for production of three-dimensional objects by stereolithography". United States patent US4575330A. Mar. 11, 1986.

[13] S. Crump. "Apparatus and method for creating three-dimensional objects". United States patent US5121329A. Jun. 9, 1992.

[14] C.R. Deckard. "Part generation by layer-wise selective laser sintering". M.Sc. thesis. Univeristy of Texas-Austin, Austin, USA, 1986.

[15] C.Y. Yap, C.K. Chua, Z. Dong, et al. "Review of selective laser melting: Materials and applications". In: *Applied Physics Reviews* 2.4 (2015), p. 041101. DOI: https://doi.org/10.1063/1.4935926.

[16] H. Fayazfar, M. Salarian, A. Rogalsky, et al. "A critical review of powder-based additive manufacturing of ferrous alloys: Process parameters, microstructure and mechanical properties". In: *Materials & Design* 144 (2018), pp. 98–128. DOI: https://doi.org/10.1016/j.matdes.2018.02.018.

[17] A. Gaikwad, R.J. Williams, H. de Winton, et al. "Multi phenomena melt pool sensor data fusion for enhanced process monitoring of laser powder bed fusion additive manufacturing". In: *Materials & Design* 221 (2022), p. 110919. DOI: https://doi.org/10.1016/j.matdes.2022.110919.

[18] J. Liu, Y. Shi, Z. Lu, et al. "Manufacturing metal parts via indirect SLS of composite elemental powders". In: *Materials Science and Engineering: A* 444.1 (2007), pp. 146–152. DOI: https://doi.org/10.1016/j.msea.2006.08.070.

[19] K. Maeda and T.H.C Childs. "Laser sintering (SLS) of hard metal powders for abrasion resistant coatings". In: *Journal of Materials Processing Technology* 149.1 (2004), pp. 609–615. DOI: https://doi.org/10.1016/j.jmatprotec.2004.02.024.

[20] S. Kumar. "Manufacturing of WC–Co moulds using SLS machine". In: *Journal of Materials Processing Technology* 209.8 (2009), pp. 3840–3848. DOI: https://doi.org/10.1016/j.jmatprotec.2008.08.037.

[21] L. Dall'Ava, H. Hothi, A. Di Laura, et al. "3D Printed Acetabular Cups for Total Hip Arthroplasty: A Review Article". In: *Metals* 9.7 (2019), p. 729. DOI: https://doi.org/10.3390/met9070729.

[22] T. DebRoy, H. Wei, J. Zuback, et al. "Additive manufacturing of metallic components – Process, structure and properties". In: *Progress in Materials Science* 92 (2018), pp. 112–224. DOI: https://doi.org/10.1016/j.pmatsci.2017.10.001.

[23] S.L. Sing, J. An, W.Y. Yeong, et al. "Laser and electron-beam powder-bed additive manufacturing of metallic implants: A review on processes, materials and designs". In: *Journal of Orthopaedic Research* 34.3 (2016), pp. 369–385. DOI: https://doi.org/10.1002/jor.23075.

[24] D. Ahn. "Directed Energy Deposition (DED) Process: State of the Art". In: *International Journal of Precision Engineering and Manufacturing-Green Technology* 8 (2021), pp. 703–742. DOI: https://doi.org/10.1007/s40684-020-00302-7.

[25] T. Moritz and S. Maleksaeedi. "Additive manufacturing of ceramic components". In: *Additive Manufacturing*. Oxford: Butterworth-Heinemann, 2018, pp. 105–161. ISBN: 978-0-12-812155-9. DOI: https://doi.org/10.1016/B978-0-12-812155-9.00004-9.

[26] W.F. Smith. "Carbon steels". In: *Structure and Properties of Engineering Alloys*. New York: McGraw-Hill, 1993. Chap. 3, pp. 110–111. ISBN: 9780070591721.

[27] S. Qu, C. Huang, Y. Gao, et al. "Tensile and compressive properties of AISI 304L stainless steel subjected to equal channel angular pressing". In: *Materials Science and Engineering: A* 475.1 (2008), pp. 207–216. DOI: https://doi.org/10.1016/j.msea.2007.04.111.

[28] A. Röttger, K. Geenen, M. Windmann, et al. "Comparison of microstructure and mechanical properties of 316L austenitic steel processed by selective laser melting with hot-isostatic pressed and cast material". In: *Materials Science and Engineering: A* 678 (2016), pp. 365–376. DOI: https://doi.org/10.1016/j.msea.2016.10.012.

[29] J. Wu and C. Lin. "Influence of high temperature exposure on the mechanical behavior and microstructure of 17-4 PH stainless steel". In: *Journal of materials science* 38 (2003), pp. 965–971. DOI: https://doi.org/10.1023/A:1022377225704.

[30] C. Tan, K. Zhou, W. Ma, et al. "Microstructural evolution, nanoprecipitation behavior and mechanical properties of selective laser melted high-performance grade 300 maraging steel". In: *Materials & Design* 134 (2017), pp. 23–34. DOI: https://doi.org/10.1016/j.matdes.2017.08.026.

[31] Y. Bai, Y. Yang, D. Wang, et al. "Influence mechanism of parameters process and mechanical properties evolution mechanism of maraging steel 300 by selective laser melting". In: *Materials Science and Engineering: A* 703 (2017), pp. 116–123. DOI: https://doi.org/10.1016/j.msea.2017.06.033.

[32] K. Kempen, B. Vrancken, S. Buls, et al. "Selective Laser Melting of Crack-Free High Density M2 High Speed Steel Parts by Baseplate Preheating". In: *Journal of Manufacturing Science and Engineering* 136 (2014), p. 061026. DOI: https://doi.org/10.1115/1.4028513.

[33] Rochester institute of technology. "Comparison of a Low-Pressure Turbine (LPT) Bracket by Two Manufacturing Methods". In: *Life cycle assessment (LCA) report* (2023). Accessed on 2023-08-23, pp. 69–102. URL: https://amgta.org/wp-content/uploads/2023/04/Comparative-LCA-of-a-Low-Pressure-Turbine-LPT-Bracket-by-Two-Manufacturing-Methods.pdf.

[34] Wohlers Associates. *Wohlers Report 2022: 3D Printing and Additive Manufacturing Global State of the Industry*. Washington, DC: Wohlers Associates, 2022, pp. 152–156. ISBN: 9780991333295.

[35] P. Moghimian, T. Poirié, M. Habibnejad-Korayem, et al. "Metal powders in additive manufacturing: A review on reusability and recyclability of common titanium, nickel and aluminum alloys". In: *Additive Manufacturing* 43 (2021), p. 102017. DOI: https://doi.org/10.1016/j.addma.2021.102017.

[36] Q. Zhang, D. Yu, P. Zhang, et al. "Modeling and analysis of the plasma primary atomization for controllable preparation of high-quality spherical metal powders". In: *Journal of Materials Processing Technology* 309 (2022), p. 117753. DOI: https://doi.org/10.1016/j.jmatprotec.2022.117753.

[37] M. Gao, B. Ludwig, and T.A. Palmer. "Impact of atomization gas on characteristics of austenitic stainless steel powder feedstocks for additive manufacturing". In: *Powder Technology* 383 (2021), pp. 30–42. DOI: https://doi.org/10.1016/j.powtec.2020.12.005.

[38] T.L. Starr, K. Rafi, B. Stucker, et al. "Controlling phase composition in selective laser melted stainless steels". In: *2012 International Solid Freeform Fabrication Symposium* (Aug. 2012), pp. 439–446. DOI: http://dx.doi.org/10.26153/tsw/15363.

[39] E.O. Olakanmi, R.F. Cochrane, and K.W. Dalgarno. "A review on selective laser sintering/melting (SLS/SLM) of aluminium alloy powders: Processing, microstructure, and properties". In: *Progress in Materials Science* 74 (2015), pp. 401–477. DOI: https://doi.org/10.1016/j.pmatsci.2015.03.002.

[40] S. Dietrich, M. Wunderer, A. Huissel, et al. "A New Approach for a Flexible Powder Production for Additive Manufacturing". In: *Procedia Manufacturing* 6 (2016), pp. 88–95. DOI: https://doi.org/10.1016/j.promfg.2016.11.012.

[41] A.B. Spierings and G. Levy. "Comparison of density of stainless steel 316L parts produced with selective laser melting using different powder grades". In: *2009 International Solid Freeform Fabrication Symposium* (Sept. 2009), pp. 342–353. DOI: http://dx.doi.org/10.26153/tsw/15113.

[42] J.H. Tan, W.L.E. Wong, and K.W. Dalgarno. "An overview of powder granulometry on feedstock and part performance in the selective laser melting process". In: *Additive Manufacturing* 18 (2017), pp. 228–255. DOI: https://doi.org/10.1016/j.addma.2017.10.011.

[43] S. Vunnam, A. Saboo, C. Sudbrack, et al. "Effect of powder chemical composition on the as-built microstructure of 17-4 PH stainless steel processed by selective laser melting". In: *Additive Manufacturing* 30 (2019), p. 100876. DOI: https://doi.org/10.1016/j.addma.2019.100876.

[44] C. Panwisawas, Y. Tang, and R.C. Reed. "Metal 3D printing as a disruptive technology for superalloys". In: *Nature Communications* 11.1 (2020), p. 2327. DOI: https://doi.org/10.1038/s41467-020-16188-7.

[45] N. Ahmed, I. Barsoum, G. Haidemenopoulos, et al. "Process parameter selection and optimization of laser powder bed fusion for 316L stainless steel: A review". In: *Journal of Manufacturing Processes* 75 (2022), pp. 415–434. DOI: https://doi.org/10.1016/j.jmapro.2021.12.064.

[46] A.A. Martin, N.P. Calta, S.A. Khairallah, et al. "Dynamics of pore formation during laser powder bed fusion additive manufacturing". In: *Nature Communications* 10 (2019), pp. 1–10. DOI: https://doi.org/10.1038/s41467-019-10009-2.

[47] R. Cunningham, C. Zhao, N. Parab, et al. "Keyhole threshold and morphology in laser melting revealed by ultrahigh-speed x-ray imaging". In: *Science* 363.6429 (2019), pp. 849–852. DOI: 10.1126/science.aav4687.

[48] M. Bayat, A. Thanki, S. Mohanty, et al. "Keyhole-induced porosities in Laser-based Powder Bed Fusion (L-PBF) of Ti6Al4V: High-fidelity modelling and experimental validation". In: *Additive Manufacturing* 30 (2019), p. 100835. DOI: https://doi.org/10.1016/j.addma.2019.100835.

[49] R. Li, J. Liu, Y. Shi, et al. "Balling behavior of stainless steel and nickel powder during selective laser melting process". In: *International Journal of Advanced Manufacturing Technology* 59 (2012), pp. 1025–1035. DOI: https://doi.org/10.1007/s00170-011-3566-1.

[50] J.V. Gordon, S.P. Narra, R.W. Cunningham, et al. "Defect structure process maps for laser powder bed fusion additive manufacturing". In: *Additive Manufacturing* 36 (2020), p. 101552. DOI: https://doi.org/10.1016/j.addma.2020.101552.

[51] M. Laleh, A.E. Hughes, S. Yang, et al. "A critical insight into lack-of-fusion pore structures in additively manufactured stainless steel". In: *Additive Manufacturing* 38 (2021), p. 101762. DOI: https://doi.org/10.1016/j.addma.2020.101762.

[52] L. Rayleigh. "On The Instability Of Jets". In: *Proceedings of the London Mathematical Society* s1-10.1 (1878), pp. 4–13. DOI: https://doi.org/10.1112/plms/s1-10.1.4.

[53] I. Yadroitsev, A. Gusarov, I. Yadroitsava, et al. "Single track formation in selective laser melting of metal powders". In: *Journal of Materials Processing Technology* 210.12 (2010), pp. 1624–1631. DOI: https://doi.org/10.1016/j.jmatprotec.2010.05.010.

[54] E. Yasa and J.P. Kruth. "Microstructural investigation of Selective Laser Melting 316L stainless steel parts exposed to laser re-melting". In: *Procedia Engineering* 19 (2011), pp. 389–395. DOI: https://doi.org/10.1016/j.proeng.2011.11.130.

[55] F. Lv, H. Liang, D. Xie, et al. "On the role of laser in situ re-melting into pore elimination of Ti–6Al–4V components fabricated by selective laser melting". In: *Journal of Alloys and Compounds* 854 (2021), p. 156866. DOI: https://doi.org/10.1016/j.jallcom.2020.156866.

[56] J.P. Kruth, L. Froyen, J. Van Vaerenbergh, et al. "Selective laser melting of iron-based powder". In: *Journal of Materials Processing Technology* 149.1 (2004), pp. 616–622. DOI: https://doi.org/10.1016/j.jmatprotec.2003.11.051.

[57] Y. Tang, C. Panwisawas, J.N. Ghoussoub, et al. "Alloys-by-design: Application to new superalloys for additive manufacturing". In: *Acta Materialia* 202 (2021), pp. 417–436. DOI: https://doi.org/10.1016/j.actamat.2020.09.023.

[58] Y. Li and D. Gu. "Thermal behavior during selective laser melting of commercially pure titanium powder: Numerical simulation and experimental study". In: *Additive Manufacturing* 1-4 (2014), pp. 99–109. DOI: https://doi.org/10.1016/j.addma.2014.09.001.

[59] M.C. Brennan, J.S. Keist, and T.A. Palmer. "Defects in Metal Additive Manufacturing Processes". In: *Journal of Materials Engineering and Performance* 30 (2021), pp. 4808–4818. DOI: https://doi.org/10.1007/s11665-021-05919-6.

[60] Z. Zhou, L. Huang, Y. Shang, et al. "Causes analysis on cracks in nickel-based single crystal superalloy fabricated by laser powder deposition additive manufacturing". In: *Materials & Design* 160 (2018), pp. 1238–1249. DOI: https://doi.org/10.1016/j.matdes.2018.10.042.

[61] M. Zhong, H. Sun, W. Liu, et al. "Boundary liquation and interface cracking characterization in laser deposition of Inconel 738 on directionally solidified Ni-based superalloy". In: *Scripta Materialia* 53.2 (2005), pp. 159–164. DOI: https://doi.org/10.1016/j.scriptamat.2005.03.047.

[62] E. Chauvet, P. Kontis, E.A. Jägle, et al. "Hot cracking mechanism affecting a non-weldable Ni-based superalloy produced by selective electron Beam Melting". In: *Acta Materialia* 142 (2018), pp. 82–94. DOI: https://doi.org/10.1016/j.actamat.2017.09.047.

[63] J.H. Martin, B.D. Yahata, J.M. Hundley, et al. "3D printing of high-strength aluminium alloys". In: *Nature* 549 (2017), pp. 365–369. DOI: https://doi.org/10.1038/nature23894.

[64] M.L. Köhler, J. Kunz, S. Herzog, et al. "Microstructure analysis of novel LPBF-processed duplex stainless steels correlated to their mechanical and corrosion properties". In: *Materials Science and Engineering: A* 801 (2021), p. 140432. DOI: https://doi.org/10.1016/j.msea.2020.140432.

[65] W. Hearn, R. Steinlechner, and E. Hryha. "Laser-based powder bed fusion of non-weldable low-alloy steels". In: *Powder Metallurgy* 65.2 (2022), pp. 121–132. DOI: https://doi.org/10.1080/00325899.2021.1959695.

[66] J. Damon, R. Koch, D. Kaiser, et al. "Process development and impact of intrinsic heat treatment on the mechanical performance of selective laser melted AISI 4140". In: *Additive Manufacturing* 28 (2019), pp. 275–284. DOI: https://doi.org/10.1016/j.addma.2019.05.012.

[67] F. Deirmina, N. Peghini, B. AlMangour, et al. "Heat treatment and properties of a hot work tool steel fabricated by additive manufacturing". In: *Materials Science and Engineering: A* 753 (2019), pp. 109–121. DOI: https://doi.org/10.1016/j.msea.2019.03.027.

[68] R. Mertens, B. Vrancken, N. Holmstock, et al. "Influence of Powder Bed Preheating on Microstructure and Mechanical Properties of H13 Tool Steel SLM Parts". In: *Physics Procedia* 83 (2016), pp. 882–890. DOI: https://doi.org/10.1016/j.phpro.2016.08.092.

[69] S. Kou. "Solidification and liquation cracking issues in welding". In: *JOM* 55 (2003), pp. 37–42. DOI: https://doi.org/10.1007/s11837-003-0137-4.

[70] A.G. Demir and B. Previtali. "Investigation of remelting and preheating in SLM of 18Ni300 maraging steel as corrective and preventive measures for porosity reduction". In: *International Journal of Advanced Manufacturing Technology* 93 (2017), pp. 2697–2709. DOI: https://doi.org/10.1007/s00170-017-0697-z.

[71] C. Qiu, Z. Wang, A.S. Aladawi, et al. "Influence of Laser Processing Strategy and Remelting on Surface Structure and Porosity Development during Selective Laser Melting of a Metallic Material". In: *Metallurgical and Materials Transactions A: Physical Metallurgy and Materials Science* 50 (2019), pp. 4423–4434. DOI: https://doi.org/10.1007/s11661-019-05348-0.

[72] J. Ghorbani, J. Li, and A.K. Srivastava. "Application of optimized laser surface re-melting process on selective laser melted 316L stainless steel inclined parts". In: *Journal of Manufacturing Processes* 56 (2020), pp. 726–734. DOI: https://doi.org/10.1016/j.jmapro.2020.05.025.

[73] E. Yasa, J. Deckers, and J.P. Kruth. "The investigation of the influence of laser re-melting on density, surface quality and microstructure of selective laser melting parts". In: *Rapid Prototyping Journal* 17 (2011), pp. 312–327. DOI: https://doi.org/10.1108/13552541111156450.

[74] J. Zhou, X. Han, H. Li, et al. "Investigation of layer-by-layer laser remelting to improve surface quality, microstructure, and mechanical properties of laser powder bed fused AlSi10Mg alloy". In: *Materials & Design* 210 (2021), p. 110092. DOI: https://doi.org/10.1016/j.matdes.2021.110092.

[75] J. Song, Q. Tang, Q. Feng, et al. "Effect of remelting processes on the microstructure and mechanical behaviours of 18Ni-300 maraging steel manufactured by selective laser melting". In: *Materials Characterization* 184 (2022), p. 111648. DOI: https://doi.org/10.1016/j.matchar.2021.111648.

[76] H. Kim, J. Park, M. Kang, et al. "Interpretation of Charpy impact energy characteristics by microstructural evolution of dynamically compressed specimens in three tempered martensitic steels". In: *Materials Science and Engineering: A* 649 (2016), pp. 57–67. DOI: https://doi.org/10.1016/j.msea.2015.09.099.

[77] Q. Chen, J. Chen, J. Ren, et al. "Effect of Si content on microstructure and cryogenic toughness of heat affected zone of low nickel steel". In: *Materials Science and Engineering: A* 771 (2020), p. 138621. DOI: https://doi.org/10.1016/j.msea.2019.138621.

[78] M.C. Jo, J. Park, S.S. Sohn, et al. "Effects of untransformed ferrite on Charpy impact toughness in 1.8-GPa-grade hot-press-forming steel sheets". In: *Materials Science and Engineering: A* 707 (2017), pp. 65–72. DOI: https://doi.org/10.1016/j.msea.2017.09.027.

[79] Q. Saby, J.Y. Buffière, E. Maire, et al. "Laser Powder Bed Fusion printability of cobalt-free steel powders for manufacturing injection molds". In: *Additive Manufacturing* 44 (2021), p. 102031. DOI: https://doi.org/10.1016/j.addma.2021.102031.

[80] L. Wang, J. Wu, X. Huang, et al. "SLM-manufactured 30CrMnSiA alloy: Mechanical properties and microstructural effects of designed heat treatment". In: *Optics & Laser Technology* 107 (2018), pp. 89–98. DOI: https://doi.org/10.1016/j.optlastec.2018.05.020.

[81] B. Huang, Y. Zhai, S. Liu, et al. "Microstructure anisotropy and its effect on mechanical properties of reduced activation ferritic/martensitic steel fabricated by selective laser melting". In: *Journal of Nuclear Materials* 500 (2018), pp. 33–41. DOI: https://doi.org/10.1016/j.jnucmat.2017.12.011.

[82] R. Seede, B. Zhang, A. Whitt, et al. "Effect of heat treatments on the microstructure and mechanical properties of an ultra-high strength martensitic steel fabricated via laser powder bed fusion additive manufacturing". In: *Additive Manufacturing* 47 (2021), p. 102255. DOI: https://doi.org/10.1016/j.addma.2021.102255.

[83] W. Wang and S. Kelly. "A metallurgical evaluation of the powder-bed laser additive manufactured 4140 steel material". In: *JOM* 68 (2016), pp. 869–875. DOI: https://doi.org/10.1007/s11837-015-1804-y.

[84] M. Abdelwahed, S. Bengtsson, R. Casati, et al. "Effect of water atomization on properties of type 4130 steel processed by L-PBF". In: *Materials & Design* 210 (2021), p. 110085. DOI: https://doi.org/10.1016/j.matdes.2021.110085.

[85] E. Jelis, M. Clemente, S. Kerwien, et al. "Metallurgical and mechanical evaluation of 4340 steel produced by direct metal laser sintering". In: *JOM* 67 (2015), pp. 582–589. DOI: https://doi.org/10.1007/s11837-014-1273-8.

[86] M. Jamshidinia, A. Sadek, W. Wang, et al. "Additive manufacturing of steel alloys using laser powder-bed fusion". In: *Advanced Materials & Processes* 173.1 (2015), pp. 20–25. DOI: https://doi.org/10.31399/asm.amp.2015-01.p020.

[87] M. Schmitt, T. Kamps, F. Siglmüller, et al. "Laser-based powder bed fusion of 16MnCr5 and resulting material properties". In: *Additive Manufacturing* 35 (2020), p. 101372. DOI: https://doi.org/10.1016/j.addma.2020.101372.

[88] E. Jelis, M.R. Hespos, and N.M. Ravindra. "Process evaluation of AISI 4340 steel manufactured by laser powder bed fusion". In: *Journal of Materials Engineering and Performance* 27 (2018), pp. 63–71. DOI: https://doi.org/10.1007/s11665-017-2989-8.

[89] M. Jurisch, B. Klöden, A. Kirchner, et al. "SEBM processing of 42CrMo4". In: *Progress in Additive Manufacturing* 5 (2020), pp. 27–32. DOI: https://doi.org/10.1007/s40964-020-00116-8.

[90] M. Abdelwahed, R. Casati, A. Larsson, et al. "On the Recycling of Water Atomized Powder and the Effects on Properties of L-PBF Processed 4130 Low-Alloy Steel". In: *Materials* 15.1 (2022), p. 336. DOI: https://doi.org/10.3390/ma15010336.

[91] R. Seede, D. Shoukr, B. Zhang, et al. "An ultra-high strength martensitic steel fabricated using selective laser melting additive manufacturing: Densification, microstructure, and mechanical properties". In: *Acta Materialia* 186 (2020), pp. 199–214. DOI: https://doi.org/10.1016/j.actamat.2019.12.037.

[92] J.J.S. Dilip, G.D. Janaki Ram, T.L. Starr, et al. "Selective laser melting of HY100 steel: Process parameters, microstructure and mechanical properties". In: *Additive Manufacturing* 13 (2017), pp. 49–60. DOI: https://doi.org/10.1016/j.addma.2016.11.003.

[93] H. Kim, Z. Liu, W. Cong, et al. "Tensile Fracture Behavior and Failure Mechanism of Additively-Manufactured AISI 4140 Low Alloy Steel by Laser Engineered Net Shaping". In: *Materials* 10.11 (2017), p. 1283. DOI: https://doi.org/10.3390/ma10111283.

[94] M. Mazur, P. Brincat, M. Leary, et al. "Numerical and experimental evaluation of a conformally cooled H13 steel injection mould manufactured with selective laser melting". In: *International Journal of Advanced Manufacturing Technology* 93 (2017), pp. 881–900. DOI: https://doi.org/10.1007/s00170-017-0426-7.

[95] N. Sanaei and A. Fatemi. "Defects in additive manufactured metals and their effect on fatigue performance: A state-of-the-art review". In: *Progress in Materials Science* 117 (2021), p. 100724. DOI: https://doi.org/10.1016/j.pmatsci.2020.100724.

[96] D. Ren, S. Li, H. Wang, et al. "Fatigue behavior of Ti-6Al-4V cellular structures fabricated by additive manufacturing technique". In: *Journal of Materials Science & Technology* 35 (2019), pp. 285–294. DOI: https://doi.org/10.1016/j.jmst.2018.09.066.

[97] P. Kumar and U. Ramamurty. "High cycle fatigue in selective laser melted Ti-6Al-4V". In: *Acta Materialia* 194 (2020), pp. 305–320. DOI: https://doi.org/10.1016/j.actamat.2020.05.041.

[98] A. Raja, S.R. Cheethirala, P. Gupta, et al. "A review on the fatigue behaviour of AlSi10Mg alloy fabricated using laser powder bed fusion technique". In: *Journal of Materials Research and Technology* 17 (2022), pp. 1013–1029. DOI: https://doi.org/10.1016/j.jmrt.2022.01.028.

[99] C. Elangeswaran, A. Cutolo, G.K. Muralidharan, et al. "Effect of post-treatments on the fatigue behaviour of 316L stainless steel manufactured by laser powder bed fusion". In: *International Journal of Fatigue* 123 (2019), pp. 31–39. DOI: https://doi.org/10.1016/j.ijfatigue.2019.01.013.

[100] S. Romano, P.D. Nezhadfar, N. Shamsaei, et al. "High cycle fatigue behavior and life prediction for additively manufactured 17-4 PH stainless steel: Effect of sub-surface porosity and surface roughness". In: *Theoretical and Applied Fracture Mechanics* 106 (2020), p. 102477. DOI: https://doi.org/10.1016/j.tafmec.2020.102477.

[101] M. Pellizzari, B. AlMangour, M. Benedetti, et al. "Effects of building direction and defect sensitivity on the fatigue behavior of additively manufactured H13 tool steel". In: *Theoretical and Applied Fracture Mechanics* 108 (2020), p. 102634. DOI: https://doi.org/10.1016/j.tafmec.2020.102634.

[102] S. Beretta and S. Romano. "A comparison of fatigue strength sensitivity to defects for materials manufactured by AM or traditional processes". In: *International Journal of Fatigue* 94 (2017), pp. 178–191. DOI: https://doi.org/10.1016/j.ijfatigue.2016.06.020.

[103] N. Sanaei and A. Fatemi. "Analysis of the effect of surface roughness on fatigue performance of powder bed fusion additive manufactured metals". In: *Theoretical and Applied Fracture Mechanics* 108 (2020), p. 102638. DOI: https://doi.org/10.1016/j.tafmec.2020.102638.

[104] A. Yadollahi, N. Shamsaei, S.M. Thompson, et al. "Effects of building orientation and heat treatment on fatigue behavior of selective laser melted 17-4 PH stainless steel". In: *International Journal of Fatigue* 94 (2017), pp. 218–235. DOI: https://doi.org/10.1016/j.ijfatigue.2016.03.014.

[105] H. Wan, Y. Luo, B. Zhang, et al. "Effects of surface roughness and build thickness on fatigue properties of selective laser melted Inconel 718 at 650 °C". In: *International Journal of Fatigue* 137 (2020), p. 105654. DOI: https://doi.org/10.1016/j.ijfatigue.2020.105654.

[106] J. Kunz, S. Herzog, A. Kaletsch, et al. "Influence of initial defect density on mechanical properties of AISI H13 hot-work tool steel produced by laser powder bed fusion and hot isostatic pressing". In: *Powder Metallurgy* 65 (2022), pp. 1–12. DOI: https://doi.org/10.1080/00325899.2021.1934634.

[107] V. Chastand, A. Tezenas, Y. Cadoret, et al. "Fatigue characterization of Titanium Ti-6Al-4V samples produced by Additive Manufacturing". In: *Procedia Structural Integrity* 2 (2016), pp. 3168–3176. DOI: https://doi.org/10.1016/j.prostr.2016.06.395.

[108] F. Stern, J. Kleinhorst, J. Tenkamp, et al. "Investigation of the anisotropic cyclic damage behavior of selective laser melted AISI 316L stainless steel". In: *Fatigue & Fracture of Engineering Materials & Structures* 42.11 (2019), pp. 2422–2430. DOI: https://doi.org/10.1111/ffe.13029.

[109] A. Riemer, S. Leuders, M. Thöne, et al. "On the fatigue crack growth behavior in 316L stainless steel manufactured by selective laser melting". In: *Engineering Fracture Mechanics* 120 (2014), pp. 15–25. DOI: https://doi.org/10.1016/j.engfracmech.2014.03.008.

[110] A. Fatemi, R. Molaei, S. Sharifimehr, et al. "Torsional fatigue behavior of wrought and additive manufactured Ti-6Al-4V by powder bed fusion including surface finish effect". In: *International Journal of Fatigue* 99 (2017), pp. 187–201. DOI: https://doi.org/10.1016/j.ijfatigue.2017.03.002.

[111] A. Plessis and E. Macdonald. "Hot isostatic pressing in metal additive manufacturing: X-ray tomography reveals details of pore closure". In: *Additive Manufacturing* 34 (2020), p. 101191. DOI: https://doi.org/10.1016/j.addma.2020.101191.

[112] R. Menig, V. Schulze, and O. Vöhringer. "Influence of Optimized Warm Peening on Residual Stress Stability and Fatigue Strength of AISI 4140 in Different Material States". In: *Shot Peening*. Weinheim: Wiley-VCH Verlag GmbH & Co. KGaA, 2003, pp. 317–323. ISBN: 9783527606580. DOI: https://doi.org/10.1002/3527606580.ch40.

[113] Z. Yang, S. Li, J. Zhang, et al. "The fatigue behaviors of zero-inclusion and commercial 42CrMo steels in the super-long fatigue life regime". In: *Acta Materialia* 52.18 (2004), pp. 5235–5241. DOI: https://doi.org/10.1016/j.actamat.2004.06.031.

[114] A. Schmiedel, T. Kirste, R. Morgenstern, et al. "The fatigue life of 42CrMo4 steel in the range of HCF to VHCF at elevated temperatures up to 773 K". In: *International Journal of Fatigue* 152 (2021), p. 106437. DOI: https://doi.org/10.1016/j.ijfatigue.2021.106437.

[115] M.A. Miner. "Cumulative Damage in Fatigue". In: *Journal of Applied Mechanics* 12 (2021), pp. 159–164. DOI: https://doi.org/10.1115/1.4009458.

[116] P. Paris and F. Erdogan. "A Critical Analysis of Crack Propagation Laws". In: *Journal of Basic Engineering* 85.4 (1963), pp. 528–533. DOI: https://doi.org/10.1115/1.3656900.

[117] M. Benedetti and C. Santus. "Building the Kitagawa-Takahashi diagram of flawed materials and components using an optimized V-notched cylindrical specimen". In: *Engineering Fracture Mechanics* 224 (2020), p. 106810. DOI: https://doi.org/10.1016/j.engfracmech.2019.106810.

[118] M.H. El Haddad, K.N. Smith, and T.H. Topper. "Fatigue Crack Propagation of Short Cracks". In: *Journal of Engineering Materials and Technology* 101.1 (1979), pp. 42–46. DOI: https://doi.org/10.1115/1.3443647.

[119] Y. Murakami. "Additive manufacturing: effects of defects". In: *Metal fatigue: effects of small defects and nonmetallic inclusions*. Second Edition. Academic Press, 2019. Chap. 18, pp. 453–483. ISBN: 9780128138762. DOI: https://doi.org/10.1016/B978-0-12-813876-2.00018-2.

[120] B. De Graaff, H. Autenrieth, J. Hoffmeister, et al. "Investigation on Short Time Tempering by Induction Heating of the low alloyed AISI4140 steel". In: *Proceedings - European Conference on Heat Treatment and 21st IFHTSE Congress* (2014), pp. 12–15.

[121] C. Shi, V. Schulze, and S. Dietrich. "Influences of laser remelting on mechanical performances of AISI4140 steel". In: *Materials Science and Technology* 40.2 (2024), pp. 107–119. DOI: https://doi.org/10.1177/02670836231212614.

[122] E. Yasa, J. Deckers, J.P. Kruth, et al. "Charpy impact testing of metallic selective laser melting parts". In: *Virtual and Physical Prototyping* 5.2 (2010), pp. 89–98. DOI: https://doi.org/10.1080/17452751003703894.

[123] C. Müller, M. Wächter, R. Masendorf, et al. "Accuracy of fatigue limits estimated by the staircase method using different evaluation techniques". In: *International Journal of Fatigue* 100 (2017), pp. 296–307. DOI: https://doi.org/10.1016/j.ijfatigue.2017.03.030.

[124] C. Shi, S. Dietrich, and V. Schulze. "Parameter optimization and mechanical properties of 42CrMo4 manufactured by laser powder bed fusion". In: *The International Journal of Advanced Manufacturing Technology* 121.3 (2022), pp. 1899–1913. DOI: https://doi.org/10.1007/s00170-022-09474-9.

[125] X. Yan, S. Gao, C. Chang, et al. "Effect of building directions on the surface roughness, microstructure, and tribological properties of selective laser melted Inconel 625". In: *Journal of Materials Processing Technology* 288 (2021), p. 116878. DOI: https://doi.org/10.1016/j.jmatprotec.2020.116878.

[126] S.A. Khairallah, A.T. Anderson, A. Rubenchik, et al. "Laser powder-bed fusion additive manufacturing: Physics of complex melt flow and formation mechanisms of pores, spatter, and denudation zones". In: *Acta Materialia* 108 (2016), pp. 36–45. DOI: https://doi.org/10.1016/j.actamat.2016.02.014.

[127] A.R. Nassar, M.A. Gundermann, E.W. Reutzel, et al. "Formation processes for large ejecta and interactions with melt pool formation in powder bed fusion additive manufacturing". In: *Scientific reports* 9.1 (2019), p. 5038. DOI: https://doi.org/10.1038/s41598-019-41415-7.

[128] D. Gu, W. Meiners, K. Wissenbach, et al. "Laser additive manufacturing of metallic components: materials, processes and mechanisms". In: *International materials reviews* 57.3 (2012), pp. 133–164. DOI: https://doi.org/10.1179/1743280411Y.0000000014.

[129] B. Song, S. Dong, H. Liao, et al. "Morphology evolution mechanism of single tracks of FeAl intermetallics in selective laser melting". In: *Materials Research Innovations* 16.5 (2012), pp. 321–325. DOI: https://doi.org/10.1179/1433075X11Y.0000000045.

[130] C. Behrens, M. Siewert, A. Lüke, et al. "Simulation of Porosity Regrowth during Heat Treatment after Hot Isostatic Pressing in Titanium Components". In: *HTM Journal of Heat Treatment and Materials* 78.5 (2023), pp. 288–299. DOI: https://doi.org/10.1515/htm-2023-0018.

[131] J. Kunz, S. Herzog, A. Kaletsch, et al. "Influence of initial defect density on mechanical properties of AISI H13 hot-work tool steel produced by laser powder bed fusion and hot isostatic pressing". In: *Powder Metallurgy* 65.1 (2022), pp. 1–12. DOI: https://doi.org/10.1080/00325899.2021.1934634.

[132] C. Shi, N. Nouri, V. Schulze, et al. "High cycle fatigue behaviour of AISI 4140 steel manufactured by laser-powder bed fusion". In: *International Journal of Fatigue* 168 (2023), p. 107469. DOI: https://doi.org/10.1016/j.ijfatigue.2022.107469.

[133] V. Alfieri, V. Giannella, F. Caiazzo, et al. "Influence of position and building orientation on the static properties of LPBF specimens in 17-4 PH stainless steel". In: *Forces in Mechanics* 8 (2022), p. 100108. DOI: https://doi.org/10.1016/j.finmec.2022.100108.

[134] Q. Liu, J. Elambasseril, S. Sun, et al. "The Effect of Manufacturing Defects on the Fatigue Behaviour of Ti-6Al-4V Specimens Fabricated Using Selective Laser Melting". In: *Advanced Materials Research* 891 (2014), pp. 1519–1524. DOI: 10.4028/www.scientific.net/AMR.891-892.1519.

[135] G. Chi, D. Yi, B. Jiang, et al. "Crack propagation during Charpy impact toughness testing of TiAlVMoZr alloy tubes containing equiaxed and lamellar microstructures". In: *Journal of Alloys and Compounds* 852 (2021), p. 156581. DOI: https://doi.org/10.1016/j.jallcom.2020.156581.

[136] U. Zerbst, G. Bruno, J.Y. Buffière, et al. "Damage tolerant design of additively manufactured metallic components subjected to cyclic loading: State of the art and challenges". In: *Progress in Materials Science* 121 (2021), p. 100786. DOI: https://doi.org/10.1016/j.pmatsci.2021.100786.

[137] Z. Liao, A. la Monaca, J. Murray, et al. "Surface integrity in metal machining - Part I: Fundamentals of surface characteristics and formation mechanisms". In: *International Journal of Machine Tools and Manufacture* 162 (2021), p. 103687. DOI: https://doi.org/10.1016/j.ijmachtools.2020.103687.

[138] J. Liang, Z. Zhao, B. Guo, et al. "Enhancing plasticity by increasing tempered martensite in ultra-strong ferrite-martensite dual-phase steel". In: *Materials Research Express* 6 (2018), p. 026502. DOI: https://doi.org/10.1088/2053-1591/aaea34.

[139] V. Schulze, J. Hoffmeister, and M. Klemenz. "Correlation of Mechanical Surface Treatments, induced Surface States and Fatigue Performance of Steel Components". In: *Procedia Engineering* 19 (2011), pp. 324–330. DOI: https://doi.org/10.1016/j.proeng.2011.11.120.

[140] M. Klemenz and V. Schulze. "Application of the Concept of Local Fatigue Strength after Shot Peening of Notched Components Based on Numerical Simulations". In: *Materials Science Forum* 638 (2010), pp. 912–917. DOI: https://doi.org/10.4028/www.scientific.net/MSF.638-642.912.

[141] M. Benedetti, V. Fontanari, M. Bandini, et al. "High- and very high-cycle plain fatigue resistance of shot peened high-strength aluminum alloys: The role of surface morphology". In: *International Journal of Fatigue* 70 (2015), pp. 451–462. DOI: https://doi.org/10.1016/j.ijfatigue.2014.07.002.

[142] A.H. Noroozi, G. Glinka, and S. Lambert. "A two parameter driving force for fatigue crack growth analysis". In: *International Journal of Fatigue* 27.10 (2005), pp. 1277–1296. DOI: https://doi.org/10.1016/j.ijfatigue.2005.07.002.

[143] G. Glinka and G. Shen. "Universal features of weight functions for cracks in mode I". In: *Engineering Fracture Mechanics* 40.6 (1991), pp. 1135–1146. DOI: https://doi.org/10.1016/0013-7944(91)90177-3.

[144] B. Atzori, G. Meneghetti, and L. Susmel. "Material fatigue properties for assessing mechanical components weakened by notches and defects". In: *Fatigue & Fracture of Engineering Materials & Structures* 28.1-2 (2005), pp. 83–97. DOI: https://doi.org/10.1111/j.1460-2695.2004.00862.x.

Appendix

Table A1: Relative density of specimens manufactured with different laser power and scanning velocity, h=40 µm.

Number	Power (W)	Velocity (mm/s)	Hatching (µm)	RD (%)	Error
1	175	300	40	97.92	0.16
2	175	500	40	98.26	0.26
3	175	700	40	98.09	0.20
4	175	900	40	97.43	0.07
5	175	1100	40	97.03	0.23
6	175	1300	40	95.58	0.31
7	175	1500	40	92.61	0.24
8	200	300	40	98.19	0.09
9	200	500	40	98.51	0.17
10	200	700	40	98.41	0.34
11	200	900	40	98.42	0.21
12	200	1100	40	98.12	0.07
13	200	1300	40	98.31	0.10
14	200	1500	40	94.70	0.44
15	225	300	40	98.03	0.20
16	225	500	40	98.48	0.30
17	225	700	40	98.42	0.11
18	225	900	40	98.30	0.43
19	225	1100	40	98.14	0.31
20	225	1300	40	98.38	0.11
21	225	1500	40	96.42	0.28
22	250	300	40	98.27	0.35
23	250	500	40	98.76	0.26
24	250	700	40	98.76	0.19
25	250	900	40	98.76	0.16
26	250	1100	40	98.61	0.11
27	250	1300	40	98.45	0.32
28	250	1500	40	98.11	0.10

Table A2: Relative density of specimens manufactured with different laser power and scanning velocity, h=60 µm.

Number	Power (W)	Velocity (mm/s)	Hatching (µm)	RD (%)	Error
29	175	300	60	97.30	0.13
30	175	500	60	98.01	0.53
31	175	700	60	97.53	0.22
32	175	900	60	97.37	0.30
33	175	1100	60	96.87	0.27
34	175	1300	60	95.80	0.58
35	175	1500	60	92.93	0.30
36	200	300	60	97.55	0.22
37	200	500	60	98.57	0.47
38	200	700	60	97.86	0.35
39	200	900	60	97.67	0.19
40	200	1100	60	97.12	0.28
41	200	1300	60	96.75	0.39
42	200	1500	60	95.46	0.57
43	225	300	60	97.48	0.48
44	225	500	60	98.17	0.33
45	225	700	60	97.97	0.17
46	225	900	60	97.88	0.13
47	225	1100	60	98.59	0.14
48	225	1300	60	98.63	0.08
49	225	1500	60	98.14	0.30
50	250	300	60	98.05	0.34
51	250	500	60	98.38	0.17
52	250	700	60	98.29	0.37
53	250	900	60	98.37	0.52
54	250	1100	60	98.73	0.34
55	250	1300	60	99.10	0.30
56	250	1500	60	98.30	0.80

Table A3: Relative density of specimens manufactured with different laser power and scanning velocity, h=80 µm.

Number	Power (W)	Velocity (mm/s)	Hatching (µm)	RD (%)	Error
57	175	300	80	97.31	0.25
58	175	500	80	97.34	0.10
59	175	700	80	96.93	0.37
60	175	900	80	96.89	0.25
61	175	1100	80	96.64	0.16
62	175	1300	80	95.37	0.04
63	175	1500	80	92.38	0.33
64	200	300	80	98.09	0.18
65	200	500	80	97.78	0.26
66	200	700	80	97.98	0.39
67	200	900	80	97.65	0.36
68	200	1100	80	98.27	0.12
69	200	1300	80	98.14	0.13
70	200	1500	80	94.30	0.43
71	225	300	80	97.96	0.20
72	225	500	80	98.05	0.06
73	225	700	80	98.04	0.48
74	225	900	80	97.84	0.12
75	225	1100	80	98.22	0.34
76	225	1300	80	98.31	0.09
77	225	1500	80	95.59	0.29
78	250	300	80	98.16	0.19
79	250	500	80	98.26	0.23
80	250	700	80	98.29	0.21
81	250	900	80	98.44	0.17
82	250	1100	80	98.56	0.27
83	250	1300	80	98.64	0.12
84	250	1500	80	97.59	0.33

Table A4: The crack density of specimens manufactured with different laser power and scanning velocity, h=60 µm.

Number	Power (W)	Velocity (mm/s)	Crack density (mm/mm^2)	Error
1	175	300	0.63	0.04
2	175	500	0.59	0.11
3	175	700	0.51	0.05
4	175	900	0.52	0.05
5	175	1100	0.36	0.14
6	175	1300	0.12	0.02
7	175	1500	0.11	0.04
8	200	300	0.84	0.13
9	200	500	0.56	0.10
10	200	700	0.41	0.04
11	200	900	0.46	0.06
12	200	1100	0.25	0.04
13	200	1300	0.20	0.06
14	200	1500	0.02	0.01
15	225	300	2.99	0.12
16	225	500	1.68	0.07
17	225	700	1.32	0.11
18	225	900	0.66	0.04
19	225	1100	0.52	0.06
20	225	1300	0.25	0.04
21	225	1500	0.04	0.04
22	250	300	3.01	0.20
23	250	500	2.14	0.18
24	250	700	1.42	0.07
25	250	900	0.62	0.11
26	250	1100	0.40	0.04
27	250	1300	0.28	0.03
28	250	1500	0.23	0.03

Table A5: The density of samples manufactured with one remelting step (R1), and the reference density is 7.83 g/cm^3.

Number	Power (W)	Velocity (mm/s)	Density (g/cm^3)	Error
1	125	650	7.772	0.02
2	125	780	7.771	0.012
3	125	910	7.777	0.016
4	125	1040	7.755	0.017
5	125	1170	7.781	0.016
6	125	1300	7.766	0.001
7	150	650	7.757	0.02
8	150	780	7.774	0.007
9	150	910	7.771	0.02
10	150	1040	7.795	0.009
11	150	1170	7.777	0.01
12	150	1300	7.756	0.011
13	175	650	7.790	0.02
14	175	780	7.779	0.021
15	175	910	7.784	0.037
16	175	1040	7.759	0.02
17	175	1170	7.756	0.012
18	175	1300	7.754	0.018
19	200	650	7.755	0.022
20	200	780	7.801	0.028
21	200	910	7.776	0.021
22	200	1040	7.759	0.023
23	200	1170	7.783	0.011
24	200	1300	7.791	0.036
25	225	650	7.732	0.021
26	225	780	7.728	0.019
27	225	910	7.725	0.017
28	225	1040	7.720	0.033
29	225	1170	7.696	0.016
30	225	1300	7.770	0.047
31	250	650	7.705	0.016
32	250	780	7.710	0.02
33	250	910	7.715	0.009
34	250	1040	7.732	0.01
35	250	1170	7.718	0.023
36	250	1300	7.764	0.021

Table A6: The fatigue testing results for AB.

No.	Cycles	Stress amplitude (MPa)
1	230100	150
2	157100	150
3	359000	125
4	269300	125
5	776400	100
6	286500	100
7	648500	100
8	1053200	75
9	764700	75
10	1292000	60
11	1380000	60
12	1.00E+07	60
13	1.00E+07	50
14	1.00E+07	50
15	1.00E+07	50
16	1.00E+07	30

Table A7: The fatigue testing results for P+AB.

No.	Cycles	Stress amplitude (MPa)
1	275100	450
2	165800	450
3	312300	425
4	282300	425
5	483700	400
6	312700	400
7	647200	375
8	816900	375
9	470000	375
10	1.00E+07	350
11	1.00E+07	350
12	1.00E+07	350
13	686300	362
14	906600	362
15	1.00E+07	325
16	1.00E+07	325

Table A8: The fatigue testing results for AB after the HIP+QT heat treatment.

No.	Cycles	Stress amplitude (MPa)
1	45900	500
2	95600	500
3	227000	475
4	132600	475
5	125200	475
6	182300	450
7	193500	450
8	1.00E+07	450
9	1.00E+07	425
10	1674200	425
11	1.00E+07	400
12	1.00E+07	400
13	1.00E+07	400
14	1.00E+07	375
15	1.00E+07	375

Table A9: The fatigue testing results for P+AB after the HIP+QT heat treatment.

No.	Cycles	Stress amplitude (MPa)
1	74100	650
2	35600	650
3	125300	625
4	155600	625
5	226700	600
6	204000	600
7	904000	575
8	1228000	575
9	1.00E+07	550
10	1.00E+07	550
11	1.00E+07	550
12	1.00E+07	525
13	1.00E+07	525
14	1.00E+07	500
15	1.00E+07	500

Table A10: The fatigue testing results for AB specimens produced with one remelting step (R1).

No.	Cycles	Stress amplitude (MPa)
1	447400	150
2	430100	150
3	785700	125
4	737900	125
5	1751200	100
6	1376400	100
7	1.00E+07	75
8	1789100	75
9	2711600	75
10	3047800	75
11	1.00E+07	72.5
12	1.00E+07	72.5
13	1.00E+07	50
14	1.00E+07	50
15	1.00E+07	50

Publications

1. C. Shi, S. Dietrich, V. Schulze, Parameter optimization and mechanical properties of 42CrMo4 manufactured by laser powder bed fusion, International Journal of Advanced Manufacturing Technology. 121 (2022) 1899–1913.

2. C. Shi, N. Nouri, V. Schulze, S. Dietrich, High cycle fatigue behaviour of AISI 4140 steel manufactured by laser-powder bed fusion, International Journal of Fatigue. 168 (2023) 107469.

3. C. Shi, V. Schulze, S. Dietrich, Influences of laser remelting on mechanical performances of AISI4140 steel, Materials Science and Technology. 40 (2024) 107-119.